Innovations in Electrophoretic Deposition of Nanotitania-based Photoanodes for Use in Dye-sensitized Solar Cells

Nima Parsi Benehkohal

Department of Mining and Materials Engineering

McGill University

Montreal, QC, Canada

August 2013

A thesis submitted to McGill University in partial fulfillment of the requirements of the degree of Doctor of Philosophy

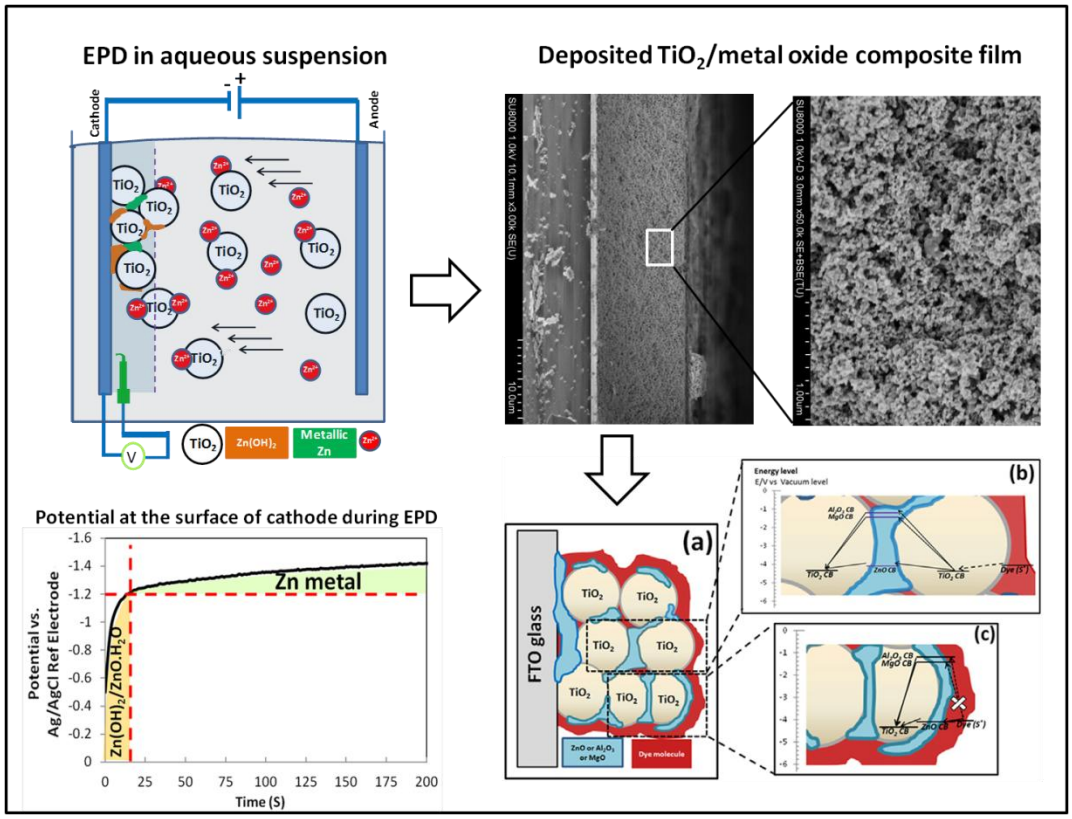
EPD in aqueous suspension
Deposited TiO_2/metal oxide composite film
Cathode
Anode
TiO_2
$Zn(OH)_2$
Metallic Zn
V
Potential at the surface of cathode during EPD
Potential vs. Ag/AgCl Ref Electrode
Time (S)
Zn metal
$Zn(OH)_2$/ZnO.H_2O
FTO glass
(a)
(b)
(c)
Energy level
E/V vs Vacuum level
ZnO or Al_2O_3 or MgO
Dye molecule

Abstract

The scope of this thesis is the investigation and elaboration of novel cost-effective and environmentally friendly electrophoretic deposition (EPD) techniques for the fabrication of robust and adhesive nanotitania film electrodes for high performance dye sensitized solar cells (DSSC). In the first part of this work, EPD in water is investigated, where electrolysis of water is suppressed by adoption of a low DC voltage approach. Growth of adherent and robust films is enabled via the use of isopropanol as co-solvent and $Zn(NO_3)_2$ as additive, the latter leading to co-deposition of hydrous zinc oxide that acts as nanoglue. The optimization of the suspension composition, mechanism of zinc co-deposition with TiO_2 nanoparticles (P25, Evonic), and the structural and electronic properties of the resultant TiO_2-ZnO semiconductor films are described. Subsequent to EPD nanocomposite TiO_2–ZnO film growth, the photoanodes after annealing at 450 ºC are assembled into DSSC devices and shown to have better photovoltaic performance compared to that of bare TiO_2 film photoanodes. Various photoelectrochemical characterizations indicated that in-situ formation of ZnO causes suppression of charge recombination at the electrode/electrolyte interface thus prolonging photoelectron lifetime.

In the next phase, the electrophoretic deposition of mixed nano scale P25 TiO_2-metal oxide composite films, namely TiO_2-ZnO, TiO_2-Al_2O_3 and TiO_2-MgO is investigated in order to probe charge recombination and electron transport properties. The secondary oxides were found to co-deposit uniformly within the TiO_2 film (forming island-like nanodeposits) at approximately 1-3 wt% content. Various photoelectrochemical characterization techniques revealed that among the three composite films, the TiO_2-Al_2O_3 electrode exhibits the highest charge recombination resistance at the TiO_2/electrolyte interface but its conversion efficiency is the lowest because it suffers from very high electron transport resistance. By comparison, the TiO_2-MgO and TiO_2-ZnO films exhibit

significantly lower electron transport resistance and relatively higher conversion efficiency.

In the last part of this thesis, EPD is employed successfully in a suspension of multi-component and different size and morphology (anatase + rutile) TiO_2 nanoparticulates to engineer a very robust bi-functional electrode structure. Aqueous-synthesized anatase (5–10 nm) nanocrystallites, sub-micrometer-sized "sea urchin"-like rutile (200–500 nm) aggregates and P25 nanoparticles (30 nm) are formulated in a stable binder-free isopropanol suspension and deposited into adhesive films not only on glass but also metal and plastic substrates without resorting to mechanical compression. As result of the scattering functionality and the excellent film adhesion rendered by rutile, contact resistance between the TiO_2 film and the substrate is minimized resulting in higher V_{OC}, fill factor and record-breaking efficiency: 8.59% vs. 8.32% for double-layer benchmark photoanode.

Résumé

Cette thèse porte sur l'étude et l'élaboration d'une nouvelle technique d'électrodéposition cationique (EPD) plus rentable et respectueuse de l'environnement. Cette technique est étudiée à des fins de fabrication d'électrodes robustes et adhésives de nano-dioxyde de titane pour des cellules photovoltaïques à pigments colorés (DSSCs) à haute performance. Dans un premier temps, l'EPD a été étudié dans un milieu aqueux. Une basse tension continue a été adoptée pour empêcher l'électrolyse de l'eau. Le dépôt de films solides et adhérents a été rendue possible par l'intermédiaire de l'utilisation d'isopropanol en tant que co-solvant et du $Zn(NO_3)_2$ en tant qu'additif. L'emploie du $Zn(NO_3)_2$ a également entrainé une déposition d'oxyde de zinc hydraté qui agit comme une nanocolle. L'optimisation de la composition de la suspension, du mécanisme de co-déposition de zinc avec des nanoparticules de TiO_2 (P25, Evonic), et les propriétés structurales et électroniques des films semi-conducteurs de TiO_2–ZnO obtenus sont décrites. Suite à la fabrication des films enTiO_2–ZnO via l'EPD, et après avoir été recuites à 450 °C, les photoanodes sont utilisées pour l'assemblage des DSSCs. Il a été démontré que ces photoanodes ont une meilleure performance photovoltaïque que celles contenant uniquement du TiO_2. Diverses caractérisations photoélectrochimiques ont indiqué une élimination de la recombinaison de charges à l'interface électrode/électrolyte lors de la formation in situ du ZnO, prolongeant ainsi la durée de vie des photoélectrons.

Dans un deuxième temps, la déposition par électrophorèse de trois films composites P25 TiO_2/oxyde de métal est étudiée, à savoir : TiO_2-ZnO, TiO_2-Al_2O_3, et TiO_2-MgO mélangés à l'échelle nano. Les propriétés de recombinaison des charges et de transport des électrons des films fabriqués ont été examinées. Il a été montré que les oxydes secondaires se co-déposent uniformément dans le film de TiO_2 (formant des nanodépôts en forme d'île) à une teneur d'environ 1-3% en poids. Diverses techniques de caractérisation photoélectrochimiques ont révélé que parmi les trois films composites, l'électrode à base deTiO_2-Al_2O_3 présente la

plus grande résistance associée à la recombinaison de charges à l'interface TiO_2/électrolyte, mais son efficacité de conversion est la plus faible, car elle éprouve d'une très forte résistance au transport des électrons. Au contraire, les films à base de TiO_2-MgO etTiO_2-ZnO présentent une résistance au transport d'électrons considérablement plus faible et une efficacité de conversion relativement élevée.

Dans la dernière partie de cette thèse, l'EPD est utilisé avec succès pour fabriquer une électrode bifonctionnelle très robuste. Une suspension à plusieurs composantes avec des nanoparticules de TiO_2 (anatase + rutile) de différentes tailles et morphologies a été utilisée. Des nanocristallites d'anatase synthétisés en milieu aqueux (5-10 nm), des agrégats de rutile de sous-taille micrométrique et en forme « d'oursin » (200-500 nm), et des nanoparticules de P25 (30 nm) sont formulés dans une suspension stable d'isopropanol sans liant, et sont déposés non seulement sur des substrats en verre, mais également sur des substrats métalliques et en plastique, et ce, sans recourir à une compression mécanique. Avec la fonctionnalité de diffusion de la lumière et l'excellente adhérence du film, grâce au rutile, la résistance de contact entre le film de TiO_2 et le substrat est réduite entrainant ainsi une augmentation de la tension V_{OC}, et du facteur de remplissage. Une efficacité de conversion record a été mesurée : 8,59 % contre 8,32 % pour la photoanode de référence à double couche.

Acknowledgements

I would like to gratefully and sincerely thank all those who provided me the possibility to complete this work. A special gratitude I give to professor Demopoulos for trusting me and giving me the opportunity to do this PhD in Materials Engineering, for scientific support and always taking time to discuss results. I also thank him for giving me the opportunity to learn by supporting me for attending many international conferences as well as Prof. Bisquert's lab in Spain. Not only be there as a supervisor, but also he has been such a supportive and understanding person, who cares, consults and helps me a lot in my personal life.

Furthermore, Professors R. Gauvin and N. Tufenkji are thanked for permission to use all required equipment in their laboratory. I would also like to acknowledge Mr. Ranjan Roy and Ms. Monique Riendeau, who gave me trainings and helped me for conducting different experiments. A special thanks goes to my current and previous members of our "Solar group" (Guobin, Hassane, Cecile, Renaud, and Nathan) for their help, guidance and support.

I would also like to express my deepest appreciation to my loving wife, Shiva Bahaei Moghadam, for her constant support, encouragement, quiet patience and unwavering love that were undeniably the bedrock upon which the past 4 years of my life have been built. She was always there cheering me up and stood by me through the good times and bad.

The last but not least, I owe my deepest gratitude to my parents for bringing me up, giving me all of their love, support and their faith in me and allowing me to be as ambitious as I wanted. I'm grateful to them to encourage and support me to continue my PhD study abroad. Without the pray from my mother, father and wife, I could not overcome hardship nor accomplish this PhD study.

To my parents and my loving wife, I dedicate this work.

Contributions of Author and Co-Authors of Published Works Presented in This Thesis

1. Nima Parsi Benehkohal, Mario A. Gomez, Raynald Gauvin, and George P. Demopoulos, *Enabling aqueous electrophoretic growth of adherent nanotitania mesoporous films via intrafilm cathodic deposition of hydrous zinc oxide*, **Electrochimica Acta**, 2013. 87(0): p. 169-179.

2. Nima Parsi Benehkohal and George P. Demopoulos, *Green Preparation of TiO_2-ZnO Nanocomposite Photoanodes by Aqueous Electrophoretic Deposition.* **Journal of The Electrochemical Society**, 2012. 159(5): p. B602-B610.

3. Nima Parsi Benehkohal and George P. Demopoulos, *Electrophoretically self-assembled mixed metal oxide-TiO_2 nano-composite film structures for photoelectrochemical energy conversion: Probing of charge recombination and electron transport resistances.* **Journal of Power Sources**, 2013. 240(0): p. 667-675.

4. Nima Parsi Benehkohal and George P. Demopoulos, *Green-engineered all-substrate mesoporous TiO_2 thin film photoanodes with superior light harvesting structure and performance*, Accepted in **ChemSusChem** in November 2013.

In all these works, the author has conducted all the experiments and materials production, performed analysis and characterization as well as prepared the manuscript drafts. In article one he was assisted with the XPS analysis of the TiO_2 and TiO_2-ZnO films by Mario Gomez (former fellow PhD student in our group) and co-author. In addition, for film characterization in the first paper Prof. Gauvin's field emission scanning electron microscope (FE-SEM) was used.

Finally, comprehensive supervision in conducting and writing up all these publications was offered by the supervisor (Prof. Demopoulos).

The accuracy of the above statements is attested by the student's supervisor.
George P. Demopoulos _____

Table of Contents

List of Figures

List of Tables

Chapter 1. Introduction

1.1. Motivation

The depletion of fossil fuel resources and raising awareness of environmental and climate change issues have highlighted the importance of exploring renewable energy sources, such as solar energy. Despite a lot of progress and development made on silicon-based photovoltaic technologies to harness solar energy efficiently, they still cannot compete with fossil fuels mainly due to their high production costs. Therefore, it is an imperative task to develop fossil fuel-competitive photovoltaic devices with reasonable efficiency for widespread use of solar energy. Thus, dye-sensitized solar cells (DSSCs) invented by O'Regan and Gratzel in 1991[1], have emerged as a promising alternative to conventional silicon solar cells owing to their great potential for low fabrication cost, use of an abundant material, TiO_2 and relatively high efficiency. Furthermore, some other advantages such as, potential for fabricating flexible solar products on metal or plastic substrates and functioning under all lighting conditions, attract a lot of attention toward this type of device.

Despite, however the great promise for "low cost" DSSCs no commercialization breakthrough has yet emerged. Hence it is imperative that its manufacturing cost is lowered. The mesoporous nanocrystaline titania thin film electrode is in the heart of the DSSC. Its fabrication and properties greatly influence the performance of the solar cell in terms of photocurrent generation and conversion efficiency. Various R&D efforts have been directed towards nano-titania film deposition methods on the conductive substrate with the aim of improving and optimizing its morphology, thickness, porosity, adhesion to the substrate and interparticle connectivity. There are various ways in preparing TiO_2 electrodes but the most common one involves screen printing of a paste (consisting of a nanoparticle dispersion in a viscous medium) followed by annealing-sintering at elevated temperature (~500°C) [2-4]. This method is time

consuming, energy consuming due to solvent evaporation and heavy user of chemicals like organic binders that demand relatively high temperature during annealing for their decomposition [5]. An alternative method that can be employed is electrophoretic deposition (EPD) that has a great potential from the commercialization prospective since it can provide process simplification, cost reduction and high throughput manufacturing capability including the advantage of low temperature fabrication [6, 7]. EPD involves deposition of charged particles suspended in a solution on an electrified substrate under the influence of an applied electric field [8, 9]. The deposited particle film is subsequently treated by low or high temperature methods depending on the substrate to improve its physical properties [10]. Previous efforts in applying EPD to fabrication of DSSC photoanodes have featured however the use of organic solvents as suspension medium along toxic in many instances charging or binding agents that have hindered further development as a large scale fabrication technology.

1.2. Objectives

Despite the previous work on EPD preparation of mesoporous photoanode electrodes for DSSCs, in addition to the problem of dealing with the toxic waste organics generated that hinder large scale development and implementation, still there is lack of understanding of several mechanistic process and photoanode performance aspects. In this work EPD is studied as method of fabrication of nanocrystalline titania thin film electrodes for DSSCs by focusing (1) on the elaboration of an aqueous (green) EPD system and how to enable aqueous electrophoretic growth of adherent nanotitania mesoporous films; (2) on determining the relationship between the aqueous-EPD process parameters and mesoporous film properties; (3) on fabrication of different mixed metal oxide-TiO_2 nano-composite films and probing their charge recombination and electron transport properties; and (4) engineering very robust and adhesive bi-functional anatase-rutile films and their application to fabrication of flexible photoanodes. In

this regard, parameters and properties related to the suspension formulation (zeta potential, surface tension, charging agent and particle concentration) have been systematically studied; the morphology, chemical composition and optical properties of the films characterized with various techniques, including, Field Emission Gun - Scanning Electron Microscope (FEG-SEM), High Resolution - Transmission electron microscopy (HR-TEM), X-ray Diffraction (XRD), X-ray Photoelectron Spectroscopy (XPS), and Ultraviolet–visible spectroscopy (UV-Vis); and the kinetics and mechanism of TiO_2-ZnO film deposition determined. Furthermore, the photoelectrochemical properties of the EPD-built DSSCs were characterized by Current-Voltage (*J-V)* curves, EIS (electrochemical impedance spectroscopy), incident photon current conversion efficiency (IPCE) and OCVD (open circuit voltage decay) methods, and correlated to film structure properties.

The thesis is divided into seven chapters: Following this introduction chapter, the literature review on DSSC and EPD is described in Chapter 2. Chapter 3 focuses on enabling aqueous deposition of adherent nanotitania mesoporous films via intrafilm cathodic deposition of hydrous zinc oxide. Optimization of suspension and EPD process along with mechanism of deposition have been studied as well. In Chapter 4, photovoltaic properties of TiO_2-ZnO nanocomposite film employed as a photoanode in the fabrication of dye-sensitized solar cell have been studied and compared to the cell based on the bare TiO_2 film. Chapter 5 describes the expansion of our study by considering $Mg(NO_3)_2$ and $AlCl_3$ in addition to $Zn(NO_3)_2$ as charging agents, prepare three mixed (TiO_2-MO_x) composite films, probe their charge recombination and electron transport properties and relate ultimately film structure to device performance. Chapter 6 focuses on binder-free EPD of aqueous-synthesized multi sized and dual phase (anatase + rutile) TiO_2 particles in order to fabricate robust electrodes on various substrates with improved light harvesting performance. Finally, Chapter 7 summarizes the global conclusions drawn from this work and states the original contributions to knowledge.

Chapter 2. Literature Survey

2.1. Solar energy photovoltaics

Among the different power sources, solar energy has the most potential. The sun provides the earth with approximately 100,000 terawatts/year, which is about 10,000 times more than the current world's annual energy consumption. It is interesting to note that the current world's energy needs could be met by covering 0.1% of the Earth's surface with PV installations that achieve a conversion efficiency of 10% [11]. Solar energy-derived electricity remains however too expensive to be able to compete with the conventional energy sources. This has led to a great research interest in developing new photovoltaic technologies based on advanced nanomaterials and processes with potential for low production cost and large-scale implementation.

2.1.1. Different types of solar cells

A road-map for best research-cell efficiencies of different photovoltaic types is presented in Figure 0-1. Silicon-based solar cells such as single crystal and polycrystalline types are known as first generation photovoltaics that currently dominate the solar cell market. The record efficiency for monocrystalline silicon cells is 25 %. Polycrystalline silicon cells are less expensive to produce than single crystal silicon cells, but are less efficient (20.4 %) because of increased charge recombination at various structural defects (e.g. grain boundaries and dislocations). It is worth noting that the cost of these cells can be prohibitive because of the long payback time (c.a. 10 to 20 years) mainly due to the complex, costly and high-energy consuming process involved in purifying silicon and substantial loss of material during their manufacture [12, 13].

The second generation photovoltaics are the thin film solar cells, which are mainly copper (indium, gallium) diselenide ($Cu(In,Ga)Se_2$) and cadmium telluride (CdTe), both coupled with n-type cadmium selenide (CdS) to create *pn*-heterojunction. Unlike to first generation silicon cells, which are ca.100 μm thick,

the thin film cells because they feature direct bandgap semiconductors require only 1 μm deposits for complete light absorption. Amorphous silicon (A-Si) is also part of this group. CIGS has the highest efficiency (20.4 %) among thin film materials [12, 14]. CdTe with record efficiency at 18.7% constitutes presently the lowest cost PV option gaining a lot of market share the last few years. However, the use of rare elements such as indium (CIGS) as well as environmental concerns about the toxicity of the materials (e.g. Cd for CdTe) are among the issues that impede the long-term prospects of these type of devices in the market

The efficiency can be extended beyond the single-junction limit by attaching different solar cells with increasing band gap on top of each other. These devices are known as multi-junction or tandem solar cells. Here, high energy photons are absorbed by the top cell and lower energy photons are successively absorbed by the bottom cells. The maximum efficiency increases to about 37.5 % for a triple junction [12].

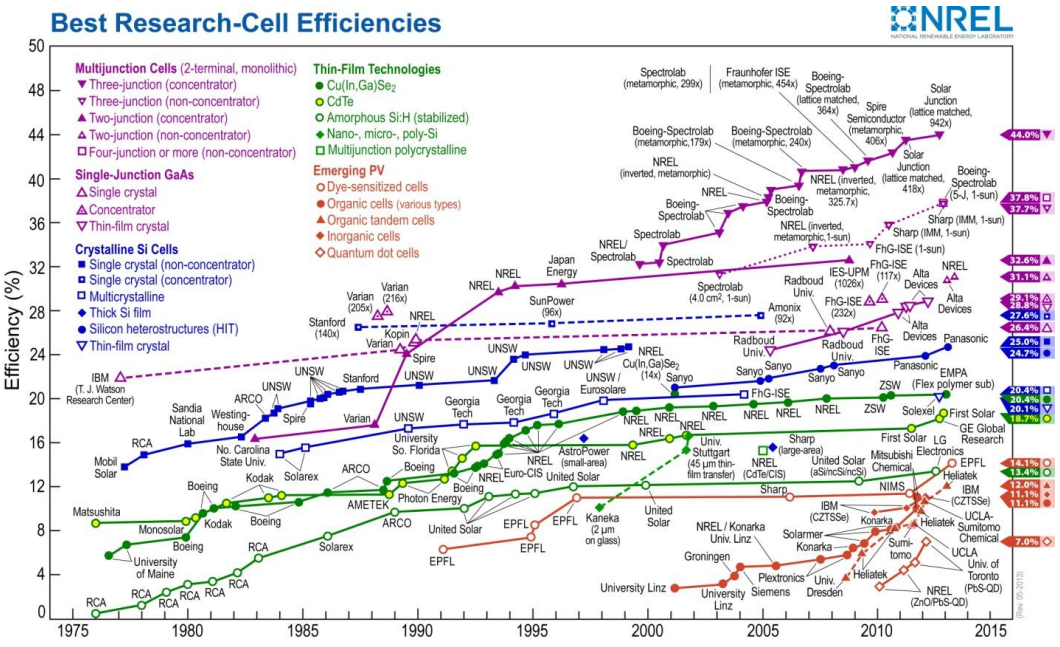

Figure 0-1. Road-map for best Research-Cell Efficiencies [15]

However, there is also a third generation of *PV* devices that unlike the previous ones that they are built via high temperature and vacuum fabrication processes, they rely on potentially cheaper roll-to-roll solution processing for their fabrication. These are usually categorized into: (1) organic heterojunction solar cells and (2) dye-sensitized solar cells. The organic heterojunction type includes two different structures, the bilayer heterojunction and the bulk heterojunction. The bilayer is similar to the *pn*-heterojunction, however the bulk heterojunction is a structure within which the *p*-*n* interface is maximized by intertwining the *n*-type and *p*-type polymers. Dye-sensitized solar cells, which constitute the research topic of this thesis, are based on mesoporous structure semiconductor (e.g. TiO_2) film coated with an organic dye, which absorbs the light. A certified record efficiency for this device of 14.1% was achieved very recently by Dr. Grätzel's group-the father of DSSCs [16].

2.1.2. Dye-sensitized solar cells (DSSCs)

The dye-sensitized solar cell (DSSC) is a nanostructured photoelectrochemical device. Unlike silicon solar cells, electrons and holes in a DSSC are separated and transported in two different phases, TiO_2 and electrolyte respectively. Hence, the possibility of recombination is decreased and as such there is no need for ultra high pure materials unlike traditional semiconductor-based solar cells. It is notable that DSSCs with moderate power conversion (~10%) efficiencies can be manufactured under lab conditions without the need of clean rooms or very specialized facilities. Furthermore, DSSCs have been shown to perform without significant change in the power conversion efficiency at higher temperatures (up to 50˚C) than conventional solar cells and more importantly under all type of lighting conditions including indoors [17]. Finally, DSSCs can be printed on flexible substrates, such as plastic [18, 19] or thin metallic substrate [20], which can broaden their applications significantly.

Due to their unique features, DSSCs may find a wide range of applications from portable battery charging items (bag packs, blankets), electronic devices and

embedded applications (computer, cell phones and TV screens) to fully building-integrated PV installations (roofs, blinds, stained windows) as illustrated in Figure 0-2.

Figure 0-2. Various applications of DSSC

On the commercial side, a number of start-up companies such as, Dyesol (Australia), Solaronix (Switzerland), G24i (Wales, UK), and SolarPrint (Ireland) have emerged with the main focus on the DSSC technology. In addition, some large companies such as Sharp, Sony, Samsung and BASF have also engaged in their own DSSC R&D activities. Sharp had till recently the official confirmed record for DSSC efficiencies, 11.2% for a 0.2 cm^2 cell [21]. Sony also has announced the record sub-module, 9.9% for 17 cm^2. In 2009, G24 Innovations (G24i) released the first commercial DSSC product, which is a flexible Ti-based module integrated into items like bags, backpacks, and wireless keyboards for portable recharging of consumer electronics. Furthermore, Dyesol, the leading distributor of DSSC materials and equipment, is also partnering with Tata Steel in

order to fabricate DSSCs on steel substrate for building-integrated photovoltaic applications [22].

2.1.3. Description of Dye-sensitized Solar Cells

2.1.3.1. DSSC structure and functional components

A DSSC is made of a photoanode placed in contact with a redox electrolyte, and a counter electrode. A schematic of the DSSC is shown in Figure 0-3 [1, 23]. The photoanode is usually composed of nanocrystalline titanium oxide semiconductor film deposited on a conductive substrate (typically FTO (fluorine doped tin oxide)-coated glass). The photoanode-the focus of this thesis- is further described in detail in section 2.1.6. A monolayer of the dye (otherwise called sensitizer) is adsorbed onto the surface of the semiconductor by chemical bonding. The function of the sensitizer is to absorb the incident light, inject the excited electrons into the semiconductor, and become regenerated by the redox couple in the electrolyte. The most common sensitizer is the N719 - an organometallic (Ru) dye, developed by Gratzel's group [24], whose molecular structure is shown in Figure 0-4. The counter electrode is usually an FTO glass coated with a layer of platinum-the latter acting as catalyst for the redox couple. Other counter electrodes such as CoS [25], carbon nanotubes [26] and conductive polymers have also been proposed [27].

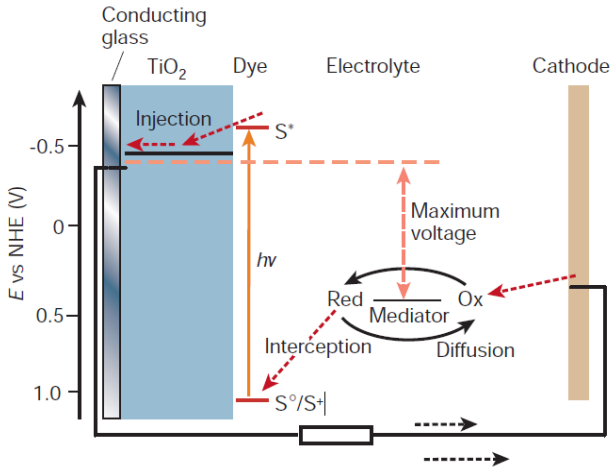

Figure 0-3. Basic operational schematic of a DSSC [28]

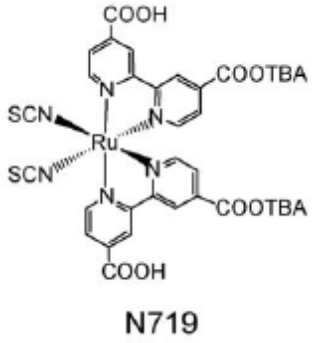

Figure 0-4. The molecular structures of Dye N719: (bis(tetrabutylammonium)[cis-di(thiocyanato)-bis(2,2'- bipyridyl-4-carboxylate-4'-carboxylic acid)-ruthenium(II)] [72]

The most commonly used redox couple is the I^-/I_3^- system in a liquid electrolyte such as acetonitrile (CH_3CN). However, limitations such as the volatility of the electrolyte can lead to long term stability issues due to difficulties in sealing the device. The change of the volatile electrolyte to a nonvolatile ionic liquid has proven to be successful both in terms of high efficiencies and good stabilities, however high viscosity and ion mobility remains a challenge [29, 30]. Ionic liquids, when used in DSSCs, can serve as both iodide source and solvent. In addition, some other redox couples such as disulfide/thiolate [31], or complexes of cobalt (II/III) redox couple [32] have been developed that can rival the performance of the I^-/I_3^- couple. Recently, new cobalt (II/III) based redox couple along with porphyrin-based dye led to high open circuit voltage and record power-conversion efficiency of 12.3% [33]. Solid-state hole conductor materials (HTM), which eliminate the problem of volatilization, also have the potential to increase the open circuit voltage and make DSSCs more manufacturable. HTMs are inorganic solids, organic polymers or p-conducting molecules. Past efforts have focused on using HTMs, but their conversion efficiency had remained modest till recently mainly due to the poor filling of the nanoporous TiO_2 layer. Recently, Chung et al. [34] replaced the entire liquid electrolyte with a p-type direct bandgap semiconductor $CsSnI_3$, which is soluble in polar organic solvents and

therefore can be transferred into TiO_2 pores at a molecular level to make intimate contact with dye molecules and TiO_2. They reported excellent conversion efficiencies up to 10.2 % for their all-solid state DSSC.

Very recently solid-state electrolytes like spiro-OMeTAD in combination with a new family of light absorbers, organic perovskites ($CH_3NH_3PbX_3$, where X a halide) have reached record efficiencies initially at the ~10+% range that now has led to 15% (14.1% as certified by NREL) world record efficiency [35, 36]. Along the same line Noh et al. [37] using again the perovskite light absorber but a different hole-transporting material, polytriarylamine (PTAA), they built a DSSC with an outstanding power conversion efficiency of 12.3%. In all these new DSSCs a mesoporous film of nanostructured TiO_2 (the subject of this work) is used as the scaffold of the photoanode

2.1.3.2. Photoelectrochemical operation

When the cell is illuminated, photo-excitation of the dye (S^*) (refer to Figure 0-5) results in the injection of electrons into the conduction band of the semiconductor (TiO_2). Injected electrons are transported by diffusion through the TiO_2 nanoparticle network towards the external conductive substrate. The circuit is been completed via electron migration through the external load. The original state of the dye is subsequently regenerated by the redox mediator (I^-) and I^- is oxidized to I_3^- state. The oxidized redox mediator, I_3^-, diffuses toward the counter electrode where is re-reduced to I^- ions.

The kinetics of different processes occurring during the operation of a DSSC is described in the energy diagram of Figure 0-5. In the dark, the Fermi level of electrons in the TiO_2 is equilibrated with the redox energy level of the electrolyte ($E_{F0} = E_{redox}$). The dye is sensitized by photon absorption and injection of its electron into the conduction band (E_C) of the semiconductor on a femto- to picosecond timescale (10^{-15}-10^{-12} s). Therefore, a quasi-Fermi level, E_F, is defined because of the additional charge in the TiO_2 under illumination. Iodide in the electrolyte regenerates the oxidized dye (S^+) within a few microseconds,

which generally occurs more rapidly than reduction of S^+ by photo-injected electrons in the TiO_2. It is worth noting that there are two competing processes namely, recombination with tri-iodide in the electrolyte and diffusion through the TiO_2 film that can influence the photo injected electron in the TiO_2. Recombination occurs in the millisecond to second range, and diffusion ideally occurs on timescale one to two orders of magnitude smaller [38].

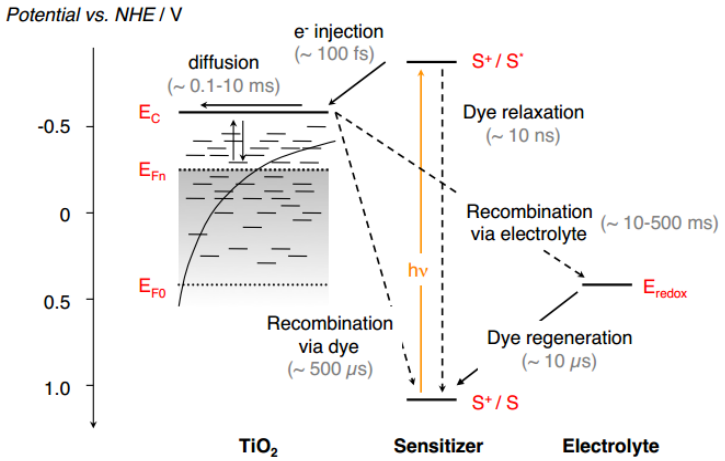

Figure 0-5. Energy diagram of the DSSC showing different kinetic processes occurring in the cell and their timescales [39].

The difference between the quasi-Fermi level (E_{Fn}) of the photoelectrode semiconductor and the redox potential of the electrolyte is defined as open circuit voltage (V_{OC}) [40]. The quasi-Fermi level (E_{Fn}) of electrons in the TiO_2 depends on the charge generation rate in the TiO_2, the transport rate, and the recombination rate. One of the features of electron transport in the mesoporous TiO_2 is multiple trapping and de-trapping events, which has been verified with several time-dependent techniques. This event seems to occur at time scales much faster than transport and recombination. The response of the cell voltage and current to change in the charge density inside the film (controlled by the incident irradiation or an applied electrical bias) suggests there is a high density of exponentially distributed trap states in the band gap within which the electron is trapped. In

general, the density of electrons in the conduction band is many orders of magnitude lower than the density of trapped electrons, however the transport and charge recombination occurs predominantly via the conduction band [41].

2.1.4. DSSC performance parameters

The performance of DSSCs is usually evaluated by the following four parameters:

- **Open-circuit voltage** (V_{OC}), the maximum potential difference that can be provided by the cell (at J_{SC} = 0). The theoretical maximum V_{OC} of the cell is determined by the difference between the Fermi level of the semiconductor and the redox potential of the electrolyte.
- **Short-circuit current density** (J_{SC}), the maximum current density that can flow between the two electrodes.
- The voltage and current density yielding **maximum power**, respectively V_{max} and J_{max}, as shown in Figure 0-6.
- **Fill factor** (*FF*), is defined as the ratio of the maximum achievable power to the product of short circuit current and open circuit voltage, as expressed in such equation (0-1):

$$FF = \frac{V_{\max} * J_{\max}}{V_{OC} * J_{SC}} \qquad (0\text{-}1)$$

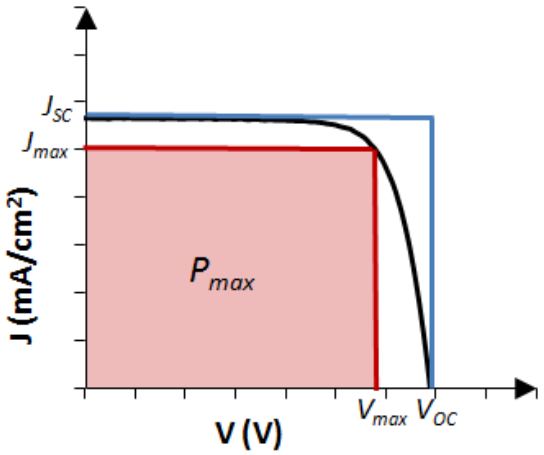

Figure 0-6. Diagram of current-voltage (*J-V*) response of a solar cell

The overall solar energy to electricity conversion efficiency of a solar cell is defined as the ratio of its electric power output to the incoming light intensity that strikes the cell. This performance is usually tested by determining the *J* vs. *V* curve (Figure 0-6) while the cell is irradiated by a calibrated light source simulating the sun light, which provides the light with a power of 1000 $W.m^{-2}$ and AM 1.5 (Air Mass 1.5). Outside of atmosphere the power of the sun light reaches 1360 $W.m^{-2}$ but at the sea level it is approximately 1000 $W.m^{-2}$ due to light absorption by the atmosphere. The air mass index relates to the spectral energy distribution of the light (Figure 0-7). Air Mass 1 is associated to the light with the sun directly overhead whereas Air Mass 1.5 is associated to the light received by locations at latitudes between 30° and 60°.

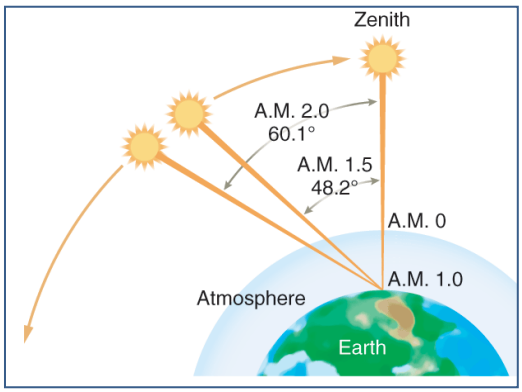

Figure 0-7. Schematic of the atmospheric sun light absorption related to various air mass indices [42]

A maximum efficiency of 20.25% with an optical bandgap of 1.31 *eV* (940 nm) was estimated for DSSCs. This estimation is based on a number of assumptions that remain to be verified/confirmed including the realization of a "dye" or light absorber with 1.31 bandgap. To achieve this efficiency various factors need to be optimized such as:1) an optimized energy alignment between dye, electrolyte and TiO_2; 2) optimizing the optical band gap of dye molecules to absorb over wider wavelength of light spectrum; 3) reduction of reflection losses from the optical transparency of the conducting glass; 4) more efficient

photoinduced electron transfer; 5) and more importantly minimizing the loss-in-potential due to the overpotential required to oxidize the electrolyte and also voltage drop for charge transport through the solar cell [43, 44].

2.1.5. Photoelectrochemical characterization techniques

2.1.5.1. Open circuit voltage decay (OCVD)

The OCVD (Open Circuit Voltage Decay) technique is a powerful tool to probe the kinetics of recombination. In this method, steady-state illumination at open circuit is switched off by a shutter and the V_{OC} recorded as a function of time. It monitors the transient of V_{OC} during relaxation from the illuminated steady-state to the dark equilibrium. Unlike frequency or steady-state-based methods, it provides a continuous reading of electron lifetime as a function of V_{OC} at high-voltage resolution [45]. The V_{OC} decay reflects the decrease of electron concentration in TiO_2, which is mainly caused by charge recombination [46]. As reported before [45], the electron lifetime (τ) can be derived from the rate of V_{OC} decay according to equation (0-2):

$$\tau = -\frac{k_B T}{e}\left(\frac{dV_{OC}}{dt}\right)^{-1} \qquad (0\text{-}2)$$

where k_B is the Boltzmann constant ($m^2\ kg\ s^{-2}\ K^{-1}$), T is the temperature (K), and e is the electron charge (C).

2.1.5.2. Electrochemical impedance spectroscopic (EIS) analysis

Electrochemical impedance spectroscopy (EIS) has been widely used over the past several years to study the kinetics of electrochemical and photoelectrochemical processes including the explanation of charge transfer (both electronic and ionic) processes occurring in the DSSC [47]. Impedance analysis for the components of the DSSC, such as mesoporous TiO_2 electrode, counter electrode, and role of electrolyte, has been done in order to clarify the behavior of charge transfer at each electrode and interface [48-50]. A typical EIS spectrum for a

DSSC exhibits three semicircles in the Nyquist plot (Figure 0-8). The left (high frequency) arc (R_{CE}) corresponds to the combination of charge transfer process at the Pt counter electrode (R_{Pt}) and FTO/TiO_2 interfaces (R_{CO}); the central arc is related to charge transport resistance in TiO_2 film (R_t), recombination at the TiO_2/dye/electrolyte interfaces (R_{rec}) and the chemical capacitance (C_μ); and the right (low frequency) arc is attributed to ion diffusion in the I^-/I_3^- electrolyte. Chemical capacitance indicates the chemical potential of electrons. As a result the chemical capacitance, due to increasing chemical potential (concentration) of electrons in the TiO_2 phase, is obtained when the electrode potential (V) displaces the electron Fermi level (E_{Fn}) of the semiconductor with respect to the lower edge of the conduction band (E_c) [51, 52]. Finally, the right (low frequency) arc is attributed to ion diffusion in the I^-/I_3^- electrolyte (Z_W).

By performing EIS analysis at variable applied voltage the shift in conduction band could be determined by the displacement observed in C_μ (chemical capacitance), this allowing for equivalent interpretation of observed differences in $R_{rec.}$ In fact, in order to evaluate properly the R_{rec}, we have to plot the R_{rec} of different cells at the same equivalent value of the position of the conduction band (i.e., the same distance between the electron Fermi level, E_{Fn}, and the CB of TiO_2 (E_{CB})), or in other words same electron density in TiO_2, since the recombination rate is proportional to electron density. This can be done by removing the displacement of CB. Therefore, despite majority of studies that perform EIS at just the V_{OC}, it is important to perform EIS at variable applied voltage [53].

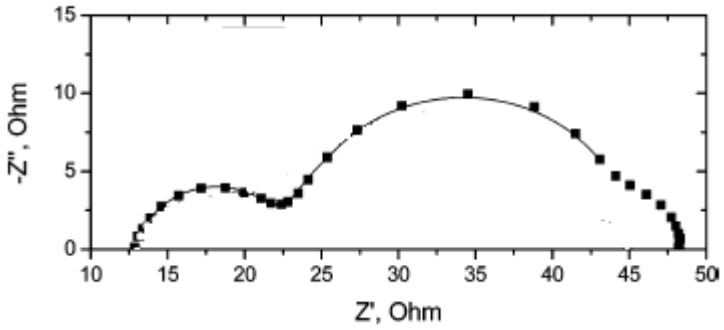

Figure 0-8. Typical Nyquist plots of a N719 sensitized DSSC [47]

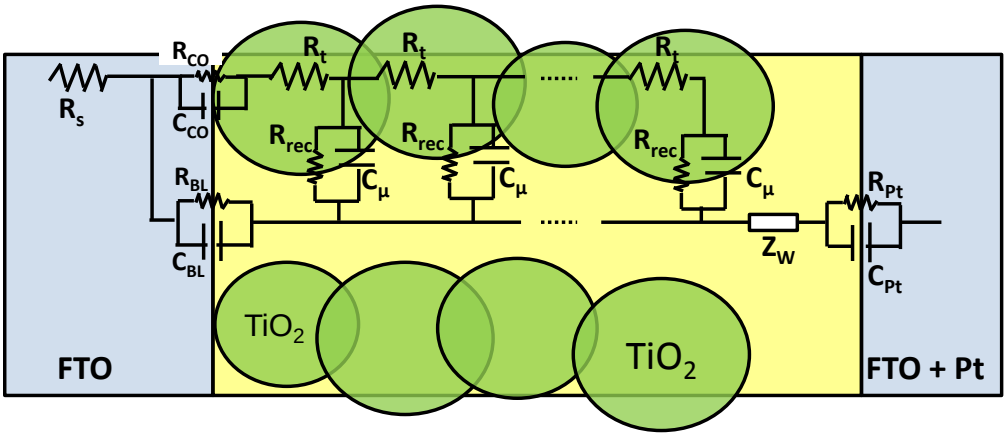

Figure 0-9. General transmission line model of DSSC. R_{Pt} and C_{Pt} are the charge-transfer resistance and double-layer capacitance at the *Pt* counter electrode, R_{CO} and C_{CO} are the resistance and the capacitance at FTO/TiO_2 interfaces, R_t is charge transport resistance in TiO_2 film, R_{rec} is recombination at the TiO_2/dye/electrolyte interfaces and C_μ the chemical capacitance, and the Z_W is attributed to ion diffusion in the I^-/I_3^- electrolyte. R_{BL} and C_{BL} are the charge-transfer resistance and the corresponding double-layer capacitance at the exposed FTO/electrolyte interface, respectively, R_s is the series resistance, including the sheet resistance of the FTO glass and the contact resistance of the cell [47, 54].

The equivalent circuit of the complete cell is represented by a transmission line model [48, 54-56], which is employed in order to simulate the experimental data and extract the EIS parameters by using for example the Z-view software (Figure 0-9). Such EIS study can lead to comprehension of the various charge transfer steps hence making possible to improve the cell's conversion efficiency.

2.1.6. DSSC Photoanodes

2.1.6.1. Materials used for fabrication of photoanodes

The working electrode (photoanode) used in DSSCs consists of a mesoporous wide band gap semiconductor like TiO_2, ZnO, SnO_2, Nb_2O_5, etc. However, among all these metal oxides, TiO_2 is the material of choice due to its stability, low cost, natural abundance, nontoxicity, and better power conversion efficiency. It is worth noting that there are several requirements to be met by the photoelectrode material: (1) it must be transparent and have high surface area for dye loading hence maximizing light harvesting; (2) it should have high charge carrier mobility and charge recombination resistance for more efficient photoelectron collection; (3) its energy level should match with that of the excited dye molecules in order to facilitate electron injection; (4) it should be easy to synthesize, stable, cheap and environmentally friendly [57, 58]. Additionally, the performance of photoanodes depends on the TiO_2 nanostructures including nanopowder [59, 60], nanowires [61], nanorods [62], and nanotubes [63-66] as well as properties of the TiO_2 nanopowder such as particle size and morphology [60, 67, 68], crystallinity, phase content [69], chemical composition (doping) [70, 71], and surface groups [72, 73], which have been extensively studied and shown to have a significant effect on the overall DSSC efficiency.

Optimized photoelectrode films usually consist of two layers: the bottom layer is a 10-12 μm thick transparent layer made of 20–30 nm anatase-TiO_2 nanoparticles, which provide high surface area for dye adsorption; the top layer which is a 4 μm thick film made of much larger TiO_2 (anatase or rutile) particles (~400 nm in diameter) to scatter light back into the bottom layer and enhance light harvesting [74]. The scattering effect may also be achieved by other approaches such as adding an over layer containing nanotubes [75-77], specially designed beads [78], hollow TiO_2 spheres[79], or TiO_2 composite materials (TiO_2-Al_2O_3, TiO_2-Nb_2O_5, and TiO_2-ZrO_2) [80]. Alternatively, a hybrid composite photoelectorde fabricated by incorporating large (sub-micron) TiO_2 particles or voids into the nano-sized

anatase particles [81], or a blend of TiO_2 nanotubes and nanoparticles [82-85], nanoparticles/nanorods [86], and nanotube/nanocube arrays [87] were also reported to provide promising photovoltaic properties.

2.1.6.2. Fabrication methods

There are various methods in preparing TiO_2 electrodes but the most common one involves screen printing of a paste (consisting of a nanoparticle dispersion in a viscous medium) followed by annealing-sintering at elevated temperature (~450°C) [2-4]. This process however is time consuming and makes use of organic binders [88] on one hand and on the other imposes challenges with its application to flexible electrode fabrication (such as conductive plastic substrates). The challenge with such substrates is that the higher temperature that can be used for annealing is limited to 150°C. As a result of that weak interconnection between the TiO_2 particles and poor substrate adhesion characterize the nanocrystalline films leading to increased resistance to electron transport and increased electrical resistance at substrate/thin film interface, negatively affecting the overall cell performance.

Therefore, many efforts have been made to develop some low-temperature preparation methods for nanocrystalline TiO_2 films. These methods include screen-printing followed by physical or chemical treatments such as compression [89, 90], UV irradiation [91], hydrothermal crystallization [92] or lift-off/transfer [93]. Another method that has been proposed for low-temperature fabrication of flexible photoanodes is electrophoretic deposition (EPD) [7]. EPD has several advantages such as fast deposition rate, simple equipment, adaptability to mass production processing and low temperature fabrication capability. EPD involves deposition of charged particles suspended in a solution on a substrate under the influence of an applied electric field [8, 9]. The deposited film is subsequently treated by low or high temperature methods depending on the substrate to

improve its physical properties [10]. The EPD method and its application to DSSC fabrication is discussed further in section 2.2.

2.1.6.3. Composite photoanodes

As mentioned previously typically photoanodes are made of two layers (transparent and scattering layers) or hybrid single layer configurations. With reference to the latter in some studies the composite photoanode was constructed using a mixture of nanoparticles with different size, shape such as, nanotube and nanowire, which resulted in enhanced conversion efficiency due to the facile electron transport as well as light scattering [94-96]. Moreover, different metal oxides have been investigated as scattering layer on top of the transparent TiO_2 film such as ZrO_2 [97] and Al_2O_3 [98]. Another approach in fabrication of composite photoanodes is the coating of the transparent TiO_2 film with a thin layer of another metal oxide (a type of core-shell configuration applied to the whole film as opposed the individual particles). This approach has been reported to enhance the cell performance of DSSCs by retarding interfacial recombination. As overcoat materials, different metal oxides with higher conduction band (CB) edges, e.g., MgO, ZnO, Nb_2O_5, Al_2O_3, SiO_2, and ZrO_2, are selected in order to minimize the back transfer of photo injected electrons through the TiO_2/dye/electrolyte interface and, hence, improve the V_{OC} and subsequently cell efficiency [99-109]. Furthermore, overcoating with different metal hydroxides such as $Mg(OH)_2$, $Zn(OH)_2$, $Al(OH)_3$, and $La(OH)_3$ prepared by electrodeposition has also been reported [110, 111]. It is worth noting that different metal hydroxides with more negative CB compared to that of TiO_2 were also applied as a blocking TiO_2 layer at the FTO/ TiO_2 interface in order to decrease electron leakage from the substrate to electrolyte [46, 112, 113].

In contrast to the core-shell (overcoat) composite structure, there are few studies on the so-called mixed composite structure. For instance, Chou et al. [114] reported the fabrication of a TiO_2/NiO mixed composite film by mixing the NiO powder with TiO_2 particles, and depositing it on FTO-glass substrate via the spin

coating process; the cell employing the composite structure yielded a better conversion efficiency(η;3.80%) than that of the conventional TiO_2 film-based DSSC (3.27%). This improvement was attributed to the blocking effect of the NiO particles. Moreover, Niu et al.[115] demonstrated that mixed TiO_2-SiO_2 composite electrodes led to pronounced increase in η from ~5.8% (bare TiO_2) to ~8.4%. This increase was explained in terms of the favorable effect SiO_2 particles had on the dispersion of TiO_2, as well as on its role as blocking layer against charge recombination. However, Chappel et al. [116] claimed that the core-shell film structure is preferable as they argued the metal oxide (usually with more negative CB compared to TiO_2; distributed in the entire film of the mixed structure) will act as energy barrier to photo injected electrons diffusing toward the current collector. However, this loss in charge transport depends on how far the CB position of the second metal oxide is located compared to TiO_2.

2.1.6.4. Substrates used for photoanodes

FTO (fluorine doped tin oxide)-coated glass is the most common substrate used for DSSC application. Replacing this substrate with flexible transparent conductive substrates, such as polyethylene terephthalate coated with indium-doped tin oxide (ITO/PET) and polyethylene naphthalate (ITO/PEN) has recently gained a lot of interest [7, 117]. Flexible DSSCs using, thin and lightweight conducting substrates as electrodes are of particular interest due to their potentials for manufacture simplification as well as wider application such as flexible electronics [91, 118]. As mentioned before, plastic substrate-based photoanodes cannot in general undergo the standard high temperature (450 ˚C) sintering/annealing treatment, which is required for necking individual TiO_2 nanoparticles [119]. Therefore, various low-temperature fabrication and post treatment techniques have been employed, which usually resulted in lower conversion efficiency compared to the standard high temperature sintering method [120, 121]. However, Vomiero et al. [19] recently fabricated a DSSC by deposition of TiO_2 nanotubes (5-6 μm thickness) on a non transparent and high-temperature

resistant plastic substrate (Kapton HN (DuPont)), which showed 3.5% conversion efficiency. Furthermore, to the best of our knowledge Yamaguchi et al [121] has reported 8% conversion efficiency, the highest value obtained so far for plastic based DSSC for 0.25 cm^2 cell area under 1 sun illumination. They prepared a thin film of TiO_2 by doctor blading followed by a subsequent low temperature compression post treatment.

Alternatively, flexible metallic substrates, such as titanium foil, thin steel or aluminum sheet can offer superior performance compared to the plastic substrate, e.g. 8.6 % efficiency using SiOx and ITO-coated stainless steel [122-126], since metallic substrates can be annealed at high temperature [127]. However, the corrosion vulnerability of metals against the iodine-containing electrolyte imposes various challenges [128]. In addition, as the metallic substrates are not transparent, the efficiency in these cells is limited, since the cell needs to be back-illuminated from the Pt counter electrode side where a part of light is absorbed by the electrolyte and the Pt layer.

2.2. Electrophoretic deposition (EPD)

The phenomenon of electrophoresis was discovered in 1807 by the Russian physicist F.F. Reuss, who observed that when a direct electric current was passed through a suspension of clay in water, the clay particles migrated towards the anode [129]. Electrophoretic deposition (EPD) is a two-step process. In the first step, charged particles suspended in a liquid migrate towards an electrode under the effect of an electric field (electrophoresis). In the second step, the particles deposit on the electrode forming a relatively dense and homogeneous compact film (Figure 0-10) [8, 9]. The movement and deposition of the particles is influenced by the charge on the particles, the electrophoretic mobility of the particles in the solvent, and the applied electric field [130].

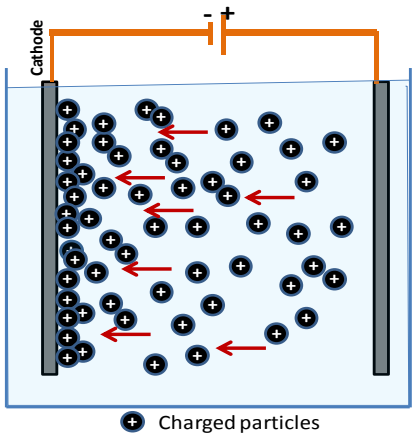

Figure 0-10. Schematic of cathodic EPD

2.2.1. EPD principles

2.2.1.1. Electrical double layer and Zeta potential

Charged particles in a fluid are surrounded by a cloud of opposite ions (counterions). This gives rise to what is called the electrical double layer on the surface of the particle. There are several theoretical treatments of the solid-liquid interface. The Stern model is the most widely accepted model for the particle double layer [131, 132]. A schematic of the double layer in accordance with the Stern model accompanied with potential distribution across the double layer is shown in

Figure 0-11. If we assume a negatively charged particle, the ions of opposite charge closest to surface of the particle form the Stern layer and the region extending outwards from the Stern layer is termed the diffuse region (Figure 0-11). The zeta potential that corresponds to the shear plane between the stern layer and the diffuse region is a key property that governs electrophoresis [63, 129, 133, 134].

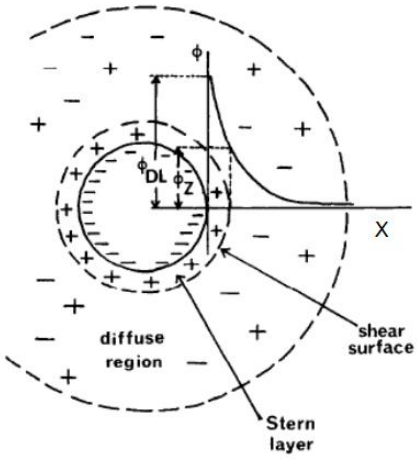

Figure 0-11. Schematic of the electric double layer of the charged particle and potential distribution φ(x) across the double layer [129]

2.2.1.2. Electrophoretic mobility (μ)

Electrophoretic mobility, μ, ($m^2\ V^{-1}\ s^{-1}$) is a property defined as the motion of the particle under the effect of electric field forces toward the electrodes [135-137]. The electrophoretic mobility of small particles defined as having a radius r much smaller than the Debye length of the counterionic atmosphere ($r << 1/\kappa$) is described by the Huckel equation 0-3[135]:

$$\mu = \frac{2\varepsilon\varepsilon_0\zeta}{3\eta} \qquad (0\text{-}3)$$

Where ζ represents the zeta potential (V), η the viscosity of the liquid ($Pa.s$), ε the dielectric constant of the solvent and ε_0 the vacuum dielectric permittivity ($F.m^{-1}$),

respectively. For particles that are large compared with $1/\kappa$ the electrophoretic mobility is given by the Smoluchowski equation (0-4):

$$\mu = \frac{\varepsilon\varepsilon_0\xi}{\eta} \quad (0\text{-}4)$$

Equally important for best results is the avoidance of particle aggregation. The interaction of colloid particles in a suspension is described by the classical DLVO theory [138, 139] in terms of two forces, electrostatic repulsion due to the double layer and van der Waals attraction between two particles. According to this theory, in order to prevent particle aggregation, high particle charge is required to create high electrostatic repulsion. By contrast, when attraction overcomes repulsion, coagulation or particle aggregation is favored.

2.2.2. Factors influencing EPD

2.2.2.1. Particle size

Electrophoretic deposition can be applied to any particulate material (<30 μm) that is in the form of a colloidal suspension. For larger particles, a very strong surface charge must be obtained, because the main problem is that they tend to settle due to gravity [129, 130]. On the other hand, very small particles tend to aggregate and therefore result in inhomogeneous deposits [140]. As such co-deposition of variable size particles may prove challenging.

2.2.2.2. Dielectric constant of solvent

The lack of reasonable surface charge due to very low dielectric constant can lead to no deposition because of insufficient ionization. On the other hand, deposits from solvents with high dielectric constants are known to be more fluid and slide easily off the electrode surface, i.e. exhibit weak adhesion. Therefore, Powers proposed that solvents with a dielectric constant in the range of 12–25 are needed to yield good deposits via EPD. It is worth noting that the low ionic concentration in the suspension, which is desirable for EPD, can be obtained in solvents of low dielectric constant [141].

2.2.2.3. Conductivity and viscosity of the suspension

The current (applied electric field) between the anode and cathode is not only carried by the charged particles but by the free coexisting ions (electrolyte) as well. Higher conductivities imply a higher fraction of ions in suspension. Therefore, at constant current a decreased fraction of charged particles contributes to the total current, which leads to a lower deposition rate [142, 143]. For solvents such as water with high dissociation power (dielectric constant ~80.1), the amount of ions in the suspension must be kept very low in order to yield stable suspension as well as high deposition rate. In contrast, if the conductivity is too low, the suspension will be resistive, leading to loss in stability [144]. Viscosity is also another important parameter in EPD process, desired to be kept low in order to have high electrophoretic mobility and finally high deposition rate [145]. It is very important to have careful control about the above described inter-related parameters. In short, low viscosity, high dielectric constant and low conductivity are desired suspension properties [130].

2.2.2.4. Stability of suspension

The suspension stability is defined in terms of settling resistance and avoidance of flocculation. Colloidal particles with an average size (1 μm or less in diameter) tend to remain in suspension for long periods due to Brownian motion. Bigger sized particles require continuous hydrodynamic agitation to remain in suspension since they usually tend to sediment due to the strong gravitational forces. The suspension stability depends on various factors such as size of the particles, their zeta potential, as well as the presence of adsorbed species [146].

The particle charge or the zeta potential is a key parameter in suspension stability and also EPD process, which can be controlled by a variety of charging agents such as acids, bases and specifically adsorbed ions or polyelectrolytes. The zeta potential plays a role in stabilization of the suspension by determining the

intensity of repulsive interaction between particles as well as determining the direction and migration velocity of a particle during EPD [129, 147].

2.2.2.5. Applied voltage

Deposition rate and thickness of deposit increase with increasing applied potential and deposition time. It has been found that at moderate applied fields (25–100 $V.cm^{-1}$) the highest uniformity of deposited films is obtained in an organic suspension, while higher applied fields (>100 $V.cm^{-1}$) cause film deterioration due to induced turbulence in the suspension [148]. By contrast, applying high voltage in an aqueous-based suspension leads to gas evolution from the electrolysis of water, preventing the deposition of a uniform adherent layer [149, 150].

2.2.2.6. Concentration of particles in suspension

The concentration of particles, which affects the green density of the deposit, in general is kept relatively low to favor good dispersed particle suspension [117, 151]. The latter is controlled by the operating zeta potential [147].

2.2.3. Solvents

Both organic and aqueous solutions have been used in EPD. Organic solvents are more popular to water as a suspension medium for EPD. Water-based suspensions result in gas evolution from the decomposition of water, which prevents the deposition of a uniform adherent layer. However, aqueous media have some advantages such as lower voltage, plus environmental and cost benefits. Different approaches have been reported to make aqueous EPD feasible such as addition of a co-solvent to suppress the water electrolysis reaction [152], working with a voltage below the threshold for water electrolysis [153], or by applying pulse potential [9, 149] or AC-electric field [154]. On the other hand, the lower dielectric constant of the organic solvents coupled with the low particle charge

demand higher field strengths, i.e. higher applied voltage. Cost, toxicity and flammability by far are the main disadvantages of organic solvents[129].

2.2.4. Particle charging

Regarding the origin of charging on particles this depends on the type of medium (organic vs. water) and the presence of ions or decomposing additives. For most oxide particles in aqueous media, adsorption or desorption of protons will determine their charge. Water or organic acids could be used as proton donors. As such pH controls the charge of particles. On the other hand, some salts such as $Mg(NO_3)_2$, $MgCl_2$, or $AlCl_3$ can be added as charging agents and binders as well. Particles are charged positively by adsorption of metal ions on the surface. On the other hand reactions at the electrode may convert these adsorbed ions into uncharged metal hydroxides that help to bind the particles on the substrate during deposition [151]. Polyelectrolytes such as PEI (polyethylenimine) can be used as additives as well to develop charging on ceramic particles [78, 135, 155].

Alcohols behave as proton donors as well. A pure alcohol can ionize in the following way:

$$RCH_2OH + RCH_2O\text{-}H \rightarrow RCH_2O^- + RCH_2OH_2^+ \qquad (0\text{-}5)$$

and an aqueous alcohol ionizes as follows:

$$RCH_2O\text{-}H + H_2O \rightarrow RCH_2O^- + H_3O^+ \qquad (0\text{-}6)$$

Then adsorbed alcohol ionizes into a protonated alcohol and an alkoxide ion, followed by the dissociation of the protonated alcohol. The dissociated alcohol and the alkoxide ion then desorb into the solution, leaving the proton on the particle surface [135].

2.2.5. Kinetics of EPD

The kinetics of EPD may be described by the Hamaker equation (0-7) [143, 156]:

$$\frac{dY}{dt} = f\mu cES \qquad (0\text{-}7)$$

in which the yield is Y (g), the time t (s), the electrophoretic mobility μ ($m^2.V^{-1}.s^{-1}$), the electric field E ($V.m^{-1}$), the concentration of powder in suspension c ($g.l^{-1}$), the electrode surface area S (m^2) and a dimensionless factor f, which takes into account that not every particle that moves toward the electrode will be eventually deposited ($f \leq 1$).

The suspension conductivity Λ (Sm^{-1}) can be calculated from the current flowing through the cell, I (A), the electric field E (Vm^{-1}) and the electrode surface area S (m^2):

$$\Lambda = \frac{I}{ES} \qquad (0\text{-}8)$$

2.2.6. Mechanism of EPD

The accurate mechanism for EPD is still not clear and under debate. Hamaker & Verwey proposed that in the EPD process, applied electric field exerts sufficient force to overcome interparticle repulsion and leads to the formation of deposit [151]. Another hypothesis is that charged particles upon contact with the opposite charge of the electrode would neutralize facilitating deposition. This mechanism is invalid when electrophoretic deposition occurs away from the electrode or when EPD is done for longer times (thick deposits).

In addition, it was suggested that electrochemical reactions at the deposition electrode cause an increase in ionic strength and decrease in zeta potential. This reduces the repulsive forces between particles near the electrode, which in turn induces coagulation of particles which collapse into deposit. Furthermore, various chemical reactions, such as reaction (2-9) and (0-10), could result in a local pH increase at the surface of cathode during the EPD [157, 158].

$$2H_2O + 2e^- \rightarrow H_2 + 2OH^- \qquad (0\text{-}9)$$

$$NO_3^- + H_2O + 2e^- \rightarrow NO_2^- + 2OH^- \qquad (0\text{-}10)$$

This local pH increase can facilitate deposition on the electrode, since pH increase towards the isoelectric point promotes particle coagulation. However, if the powder is charged positively by adsorption of metal ions on the powder via addition of salts such as $Mg(NO_3)_2$, $La(NO_3)_3$, $Y(NO_3)_3$, $MgCl_2$, or $AlCl_3$, an electrode reaction would convert these adsorbed ions into uncharged metal hydroxides, which act as binders for the deposit. This theory is acceptable to explain deposition of particles from aqueous-based suspensions but not from organic suspensions since no electrochemical reactions occur [135, 140, 151]

To overcome the problem with explaining the EPD mechanism in the absence of the electrochemical reactions, Sarkar & Nicholson [131] pointed out that the double layer of a particle in motion is distorted and becomes thinner ahead of the particle. Therefore, the next incoming particle, which has a thin leading double layer, can approach close enough for London Van der Waals (LVDW) attractive forces to overcome the repulsion barrier and finally induce coagulation/deposition.

It is worth noting that some experimental data obtained by imagery techniques are now available on how the particles aggregate on the electrode, which is modeled by various mechanisms such as electrohydrodynamics and electroosmosis. Electroosmotic flow is the result of electric field action on the diffuse layer charge of the particle, while electrohydrodynamic flow is due to the action of an electric field on charge induced by the electric field on the electrode [141, 144, 159].

2.3. Electrophoretically deposited TiO_2 films and their application in DSSCs

Several previous EPD studies involving TiO_2 deposition are summarized in Table 0-1. Different commercial types of TiO_2 particles have been used. P25 is the most common one. This consists of predominantly anatase (with 20% rutile content) nanoparticles of ~ 30nm size [3]. In general a low concentration of particles in suspension is used (only a few $g.L^{-1}$) in order to prevent particle aggregation, which leads to poor packing density of the deposited film [117, 160].

In accordance to what was discussed before, by far organic solvents are the most common suspension media. In particular, as it is evident from Table 0-1, methanol, ethanol and isopropanol have been widely used in most of previous work. The best results were obtained with ethanolic suspensions: uniform, adherent, homogeneous films with controllable thickness [161]. Various studies demonstrated that titania dense layers can be obtained also by EPD in aqueous suspensions [78, 152, 155, 162-164]. As mentioned before, some ways have been used to overcome the problems due to water electrolysis such as controlling the intensity of the applied current but this implies a long deposition time. Another way is to modify the suspension formulation. For instance, ethanol was added to water as a co-solvent in one study to prevent oxygen evolution at the anode. Their experiments revealed that the oxidation of ethanol occurs at a potential lower than that of water [152, 165]. Thus, Zhao et al. [162] fabricated 2 μm thick films made by EPD (in 30% *v/v* ethanol/water mixture) of ordered titanate nanotubes or commercial P25 TiO_2 powder, and obtained respectively 3.79 and 2.89% efficiencies after annealing at 600 $^{\circ}$C. Kim et al. [163], on the other hand, prepared 10 μm thick films by EPD (in 30% *v/v* methanol/water mixture) of titanate nanotubes on FTO, which upon annealing at 450 and 500 $^{\circ}$C showed efficiency of 4.25 and 6.71% respectively. To our knowledge, this is one of the highest conversion efficiencies reported so far for photoanodes fabricated by aqueous EPD. However, it is worthy to note that the use of titanate nanotubes greatly increases the complexity and cost

of the process making it less attractive from a commercialization perspective. Using cathode materials that can store hydrogen within their structure, like palladium, is another option that enables EPD from aqueous suspensions at the cathode [155]. A much more promising way is the membrane method. Here, a porous, ion-permeable membrane is employed as a substrate. Deposition occurs at the membrane while the ions can pass the pores of the membrane, therefore water electrolysis and generation of gas bubbles occurs at the electrodes [166].

Table 0-1: Summary of major EPD studies involving deposition of nanotitania films

NO	Particle	Substrate	Solvent	Additive	Description	Post treatment	Ref
1	P25	FTO (Cathode)	Acetylacetone	Iodine (I_2)	d= 1cm, Voltage = 5 - 20 V	Sintered at 450 °C	[148]
2	P25	ITO-PET (Cathode)	isopropanol and (0.3%) distilled water	$Mg(NO_3)_2 \cdot 6H_2O$	d= 2cm, Voltage =20-160 V pH=4.7	Compression	[7]
3	P25	FTO or Ti sheet (Cathode)	Butanol+isopropanol + ethanol	-	Electric field= 48 $V.cm^{-1}$, T=30 s	TBT treatment +water-cooked or sintered at 400 °C	[10, 167]
4	Commercial TiO_2 powder (Millenium)	Ti foils (Cathode)	Acetylacetone	Iodine	Voltage =5-30 V, t =5-120 s	Sintered at 800°C in flowing argon	[168]
5	(Nanotek TiO_2)	ITO glass (Cathode)	2-propanol with 2,4-pentanedione	-	d = 2cm, Voltage=40 V, t=30–35 s	Sintered at 400 °C	[160]
6	Commercially TiO_2 powder (ST-01, Japan)	Stainless steel (Cathode)	Acetone	-	Voltage=10-240 V , t =up to 10 min	Sintered at 600 or 800 °C	[169]
7	F-5 and G-2	ITO-PET (Cathode)	*t*-butyl alcohol + acetonitrile	-	d =0.3 mm, Voltage= 35-36 V, t= 30 s	Chemical treatment	[117]
8	P25 or P90	FTO glass and ITO-PET (Cathode)	Alcohol (methanol, ethanol, or isopropanol)+ acetylacetone	Iodine + acetone + water	d= 18 or 54mm, t=120s, Constant current= 0.4, 0.65 $mA.cm^{-2}$	Modified compression	[143, 161, 170]
9	F-5	ITO–PET (Cathode)	*t*-butyl alcohol + acetonitrile	-	Electric field=200 $V.cm^{-1}$, t =30s	CVD with UV light irradiation	[171]
10	P25 and P90	Titanium foil (Cathode)	isopropanol	-	electric fields of 200-300 $V.cm^{-1}$	Compression+ sintering at 350 °C for 1 h	[124]
11	P-90	ITO/PEN	isopropanol	-	Constant current = 20 $\mu A\ cm^{-2}$	Compression	[172]
12	Commercially TiO_2 powder (NanoTek .Japan)	Palladium sheet (Cathode)	Water	Polyethylenimine (PEI)	d= 1cm, Constant crurent = 0.375 $mA.cm^{-2}$	-	[78]
13	Spherical anatase particles (Nanotek TiO_2)	Palladium sheet (Cathode)	Water	Polyethylenimine (PEI)	Constant current=2.7 $mA.cm^{-2}$	Sintered at 650°C	[155]
14	Nanotube powder	FTO glass (anode)	Ethanol + water	Tetramethyl-ammonium hydroxide	d= 4 cm , Voltage =15 V	Sintered at 300-600°C and $TiCl_4$ treatment	[162]
15	Synthesized Titanate nanotubes	FTO glass (anode)	Methanol + water	-	Voltage=40 V , t=30 min	Sintered at 400 or 600°C	[163]
16	P25	Sb doped SnO_2 film deposited on glass plates (Cathode)	Propanol + water	-	d=2 cm , Voltage =4 V , t=40-120 s	Sintered at 450°C	[164]
17	Anatase powder (Merck Chemicals)	graphite substrate (Anode)	Water	Carboxylic acids and NaOH	d=2 cm , Voltage =10 V	-	[173]

d: distance between electrodes

In case of organic suspensions, some of the additives exploited for EPD of TiO_2 are listed in Table 0-1. Yum et al. [7] used $Mg(NO_3)_2$ salt as an additive and indicated that the zeta potential of the TiO_2 in the isopropanol changed from a negative to a positive value due to the adsorption of $MgNO_3^+$ to the particle surface. The use of iodine (I_2) alone [78, 148] or iodine, acetone, and water together [143, 161, 170] as additives was reported in several studies. It was proposed that the particle charging in this system is achieved via adsorption of protons, which are formed by the keto-enol reaction:

$$CH_3COCH_3 \leftrightarrow CH_3C(OH)CH_2 \qquad (0\text{-}11)$$

$$CH_3C(OH)CH_2 + I_2 \rightarrow CH_3COCH_2I + H^+ + I^- \qquad (0\text{-}12)$$

As only a fraction of the ions is adsorbed on the particle surface the amount of additives is minimized. Ions that do not adsorb on particle surfaces increase the ionic strength of a suspension, which causes reduced thickness of the electrical double layer on the particle surface, which in turn leads to particle aggregation and deterioration of the quality of deposited films [161].

Among various studies within which the photoanodes are fabricated by EPD in organic media the best efficiencies were: 8.5 % for TiO_2 film deposited on the FTO glass followed by compression and sintering at higher temperature [161]; 6.33% for film deposited on Ti substrate followed by chemical treatment and high temperature annealing [167]; and 6.63% for film deposited on ITO/PEN substrates by using compression post treatment [172].

The film thickness increases with deposition time. The latter is rather short in case of organic suspension, usually less than 2 min. Jarernboon et al. [148] found that the optimum TiO_2 film thickness to obtain the highest DSSC efficiency was ~14 μm. Such thickness leads to highly porous films, which can be very favorable for application in DSSCs, where electrolyte filling of the porous space and enhanced dye loading are critical [143]. On the other hand, more than optimum thickness deteriorates adhesion of the film to the substrate. It also increases the amount and size of microcracks and defects, which cause carrier recombination

and a serious loss in electron diffusion within the layer leading to lower current density and conversion efficiency [117, 148]. Preparing a multi-layer film via repeated cycles of EPD and post treatments has been proposed as a solution [117, 161].

As shown in Table 0-1, the majority of researchers have used an electric field less than 100 $V.cm^{-1}$ for organic suspension. Increasing the applied field (higher voltage or lower distance) leads to higher force and finally a thicker and denser film [169]. Constant voltage and constant current modes can be used for EPD. It has been also demonstrated that the distance between the electrodes hardly affects the deposited film quality under optimal conditions, although smaller distance between electrodes increases the deposition rate [161].

As mentioned before, in order to strengthen the interconnection between TiO_2 particles and their adhesion to the substrate, a low or high temperature treatment depending on the substrate is required [10]. High temperature post-treatment involving heating at ~450°C is applied to films deposited on glass or metal substrates [3, 160, 162, 168, 169, 174]. This is followed by immersion of the sintered films into aqueous $TiCl_4$ solution at 70°C for 30 min in a closed vessel [3]. After that, the electrodes are sintered again at 450°C for 30 min. This treatment forms a pure TiO_2 layer which increases the interconnection between the particles and also improves the electron injection efficiency [175]. For films deposited by EPD on plastic (ITO/PET or ITO/PEN) substrates, different low temperature treatments have been proposed al already mentioned earlier. For example, Miyasaka and Kijitori [117, 176] obtained 4.1% conversion efficiency at 1 sun illumination following chemical treatment with a TiO_2-containing aqueous sol, which contained brookite in a mixture of aqueous hydrochloric acid and ethanol. Tan et al. [10] rinsed as-deposited thin film with TBT (tetra-n-butyl titanate)-butanol solution and dried in an oven. Then, the TiO_2 thin film was heat-treated in a non-sealed container full of water (called “water cooked”). The TBT was hydrolyzed and crystallized into anatase to link nanocrystalline TiO_2 particles and also to increase the adhesion to the substrate by common pressure hydrothermal treatment thus improving the electron transport properties of the deposited thin

film. After this treatment a conversion efficiency of 6.12% under illumination of 1 sun was obtained that was comparable to that obtained following sintering at 450°C (6.20%).

2.4. References

1. O'Regan B, Gratzel M. A low-cost, high-efficiency solar cell based on dye-sensitized colloidal TiO_2 films. Nature 1991;353(6346):737-40.

2. Ito S, Miura H, Uchida S, Takata M, Sumioka K, Liska P, et al. High-conversion-efficiency organic dye-sensitized solar cells with a novel indoline dye. Chemical Communications 2008(41):5194-96.

3. Demopoulos GP, Charbonneau C, Lee K, Shan G, Gomez MA, Gauvin R. Synthesis of Hydroxyl-Rich Anatase Nanocrystallites, Their Characterization and Performance as Photoanode in Dye-Sensitized Solar Cells. ECS Transactions 2009;21(1):23-34.

4. Lee K, Charbonneau C, Shan G, Demopoulos G, Gauvin R. Nanocrystalline TiO_2 thin film electrodes for dye-sensitized solar cell applications. JOM Journal of the Minerals, Metals and Materials Society 2009;61(4):52-57.

5. Ito S, Chen P, Comte P, Nazeeruddin MK, Liska P, Péchy P, et al. Fabrication of screen-printing pastes from TiO_2 powders for dye-sensitised solar cells. Progress in Photovoltaics: Research and Applications 2007;15(7):603-12.

6. Meyer GJ. The 2010 Millennium Technology Grand Prize: Dye-Sensitized Solar Cells. ACS Nano 2010;4(8):4337-43.

7. Yum J-H, Kim S-S, Kim D-Y, Sung Y-E. Electrophoretically deposited TiO_2 photo-electrodes for use in flexible dye-sensitized solar cells. Journal of Photochemistry and Photobiology A: Chemistry 2005;173(1):1-6.

8. Kaya C, Kaya F, Su B, Thomas B, Boccaccini AR. Structural and functional thick ceramic coatings by electrophoretic deposition. Surface and Coatings Technology 2005;191(2-3):303-10.

9. Besra L, Uchikoshi T, Suzuki TS, Sakka Y. Application of constant current pulse to suppress bubble incorporation and control deposit morphology during aqueous electrophoretic deposition (EPD). Journal of the European Ceramic Society 2009;29(10):1837-45.

10. Tan W, Chen J, Zhou X, Zhang J, Lin Y, Li X, et al. Preparation of nanocrystalline TiO_2 thin film at low temperature and its application in dye-sensitized solar cell. Journal of Solid State Electrochemistry 2009;13(5):651-56.

11. Grätzel M. Photovoltaic and photoelectrochemical conversion of solar energy. Philosophical Transactions of the Royal Society A: Mathematical, Physical and Engineering Sciences 2007;365(1853):993-1005.

12. Green MA, Emery K, Hishikawa Y, Warta W, Dunlop ED. Solar cell efficiency tables (version 40). Progress in Photovoltaics: Research and Applications 2012;20(5):606-14.

13. Goetzberger A, Hebling C, Schock HW. Photovoltaic materials, history, status and outlook. Materials Science and Engineering R: Reports 2003;40(1).

14. Repins I, Contreras MA, Egaas B, DeHart C, Scharf J, Perkins CL, et al. 19·9%-efficient ZnO/CdS/CuInGaSe2 solar cell with 81·2% fill factor. Progress in Photovoltaics: Research and Applications 2008;16(3):235-39.

15. *NREL*. Available from: http://www.nrel.gov/.

16. Grätzel M. Perovskite nano-pigments and new molecularly engineered porphyrin light harvesters for mesoscopic solar cells. Hybrid and Organics Photovoltaics Conference (HOPV) 2013. Seville, Spain; 2013.

17. Berginc M, Opara Krašovec U, Jankovec M, Topič M. The effect of temperature on the performance of dye-sensitized solar cells based on a propyl-methyl-imidazolium iodide electrolyte. Solar Energy Materials and Solar Cells 2007;91(9):821-28.

18. Liu X, Wang L, Xue Z, Liu B. Efficient flexible dye-sensitized solar cells fabricated by transferring photoanode with a buffer layer. RSC Advances 2012;2(16):6393-96.

19. Vomiero A, Galstyan V, Braga A, Concina I, Brisotto M, Bontempi E, et al. Flexible dye sensitized solar cells using TiO_2 nanotubes. Energy & Environmental Science 2011;4(9):3408-13.

20. Ito S, Ha N-LC, Rothenberger G, Liska P, Comte P, Zakeeruddin SM, et al. High-efficiency (7.2%) flexible dye-sensitized solar cells with Ti-metal substrate for nanocrystalline- TiO_2 photoanode. Chemical Communications 2006(38):4004-06.

21. Green MA, Emery K, Hishikawa Y, Warta W. Solar cell efficiency tables (version 37). Progress in Photovoltaics: Research and Applications 2011;19(1):84-92.

22. Baxter JB. Commercialization of dye sensitized solar cells: Present status and future research needs to improve efficiency, stability, and manufacturing. Journal of Vacuum Science and Technology A: Vacuum, Surfaces and Films 2012;30(2).

23. Grätzel M. Conversion of sunlight to electric power by nanocrystalline dye-sensitized solar cells. Journal of Photochemistry and Photobiology A: Chemistry 2004;164(1-3):3-14.

24. Nazeeruddin MK, Kay A, Rodicio I, Humphry-Baker R, Mueller E, Liska P, et al. Conversion of light to electricity by cis-X2bis(2,2'-bipyridyl-4,4'-dicarboxylate)ruthenium(II) charge-transfer sensitizers (X = Cl^-, Br^-, I^-, CN^-, and SCN^-) on nanocrystalline titanium dioxide electrodes. Journal of the American Chemical Society 1993;115(14):6382-90.

25. Wang M, Anghel AM, Marsan Bt, Cevey Ha N-L, Pootrakulchote N, Zakeeruddin SM, et al. CoS Supersedes Pt as Efficient Electrocatalyst for Triiodide Reduction in Dye-Sensitized Solar Cells. Journal of the American Chemical Society 2009;131(44):15976-77.

26. Anwar H, George AE, Hill IG. Vertically-aligned carbon nanotube counter electrodes for dye-sensitized solar cells. Solar Energy 2013;88(0):129-36.

27. Bay L, West K, Winther-Jensen B, Jacobsen T. Electrochemical reaction rates in a dye-sensitised solar cell—the iodide/tri-iodide redox system. Solar Energy Materials and Solar Cells 2006;90(3):341-51.

28. Gratzel M. Photoelectrochemical cells. Nature 2001;414(6861):338-44.

29. Zeng W, Cao Y, Bai Y, Wang Y, Shi Y, Zhang M, et al. Efficient Dye-Sensitized Solar Cells with an Organic Photosensitizer Featuring Orderly

Conjugated Ethylenedioxythiophene and Dithienosilole Blocks. Chemistry of Materials 2010;22(5):1915-25.

30. Choi H, Kang SO, Ko J, Gao G, Kang HS, Kang M-S, et al. An Efficient Dye-Sensitized Solar Cell with an Organic Sensitizer Encapsulated in a Cyclodextrin Cavity. Angewandte Chemie International Edition 2009;48(32):5938-41.

31. Wang M, Chamberland N, Breau L, Moser JE, Humphry-Baker R, Marsan B, et al. An organic redox electrolyte to rival triiodide/iodide in dye-sensitized solar cells. Nature Chemistry 2010;2(5):385-89.

32. Sapp SA, Elliott CM, Contado C, Caramori S, Bignozzi CA. Substituted Polypyridine Complexes of Cobalt(II/III) as Efficient Electron-Transfer Mediators in Dye-Sensitized Solar Cells. Journal of the American Chemical Society 2002;124(37):11215-22.

33. Yella A, Lee H-W, Tsao HN, Yi C, Chandiran AK, Nazeeruddin MK, et al. Porphyrin-Sensitized Solar Cells with Cobalt (II/III)–Based Redox Electrolyte Exceed 12 Percent Efficiency. Science 2011;334(6056):629-34.

34. Chung I, Lee B, He J, Chang RPH, Kanatzidis MG. All-solid-state dye-sensitized solar cells with high efficiency. Nature 2012;485(7399):486-89.

35. Lee MM, Teuscher J, Miyasaka T, Murakami TN, Snaith HJ. Efficient Hybrid Solar Cells Based on Meso-Superstructured Organometal Halide Perovskites. Science 2012;338(6107):643-47.

36. Burschka J, Pellet N, Moon SJ, Humphry-Baker R, Gao P, Nazeeruddin MK, et al. Sequential deposition as a route to high-performance perovskite-sensitized solar cells. Nature 2013;499(7458):316-19.

37. Noh JH, Im SH, Heo JH, Mandal TN, Seok SI. Chemical Management for Colorful, Efficient, and Stable Inorganic–Organic Hybrid Nanostructured Solar Cells. Nano Letters 2013;13(4):1764-69.

38. J. Frank A, Kopidakis N, Lagemaat Jvd. Electrons in nanostructured TiO_2 solar cells: transport, recombination and photovoltaic properties. Coordination Chemistry Reviews 2004;248(13-14):1165-79.

39. Wenger S. Strategies to Optimizing Dye-Sensitized Solar Cells: Organic Sensitizers, Tandem Device Structures, and Numerical Device Modeling, PhD dissertation, hèse École polytechnique fédérale de Lausanne EPFL, Swiss; 2010.

40. Burnside S, Moser J-E, Brooks K, Grätzel M, Cahen D. Nanocrystalline Mesoporous Strontium Titanate as Photoelectrode Material for Photosensitized Solar Devices: Increasing Photovoltage through Flatband Potential Engineering. The Journal of Physical Chemistry B 1999;103(43):9328-32.

41. Peter LM. Dye-sensitized nanocrystalline solar cells. Physical Chemistry Chemical Physics 2007;9(21):2630-42.

42. Availavle at : http://www.renewableenergyworld.com/rea/news/article/2009/01/photovoltaics_-enhancements

43. Snaith HJ. Estimating the Maximum Attainable Efficiency in Dye-Sensitized Solar Cells. Advanced Functional Materials 2010;20(1):13-19.

44. Bisquert J. Dilemmas of Dye-Sensitized Solar Cells. ChemPhysChem 2011;12(9):1633-36.

45. Zaban A, Greenshtein M, Bisquert J. Determination of the Electron Lifetime in Nanocrystalline Dye Solar Cells by Open-Circuit Voltage Decay Measurements. ChemPhysChem 2003;4(8):859-64.

46. Liu Y, Sun X, Tai Q, et al. Efficiency enhancement in dye-sensitized solar cells by interfacial modification of conducting glass/mesoporous TiO_2 using a novel ZnO compact blocking film. Journal of Power Sources 2011;196(1):475-81.

47. Wang Q, Moser J-E, Gratzel M. Electrochemical Impedance Spectroscopic Analysis of Dye-Sensitized Solar Cells. The Journal of Physical Chemistry B 2005;109(31):14945-53.

48. Hoshikawa T, Kikuchi R, Eguchi K. Impedance analysis for dye-sensitized solar cells with a reference electrode. Journal of Electroanalytical Chemistry 2006;588(1):59-67.

49. He C, Zhao L, Zheng Z, Lu F. Determination of Electron Diffusion Coefficient and Lifetime in Dye-Sensitized Solar Cells by Electrochemical Impedance Spectroscopy at High Fermi Level Conditions. The Journal of Physical Chemistry C 2008;112(48):18730-33.

50. Hauch A, Georg A. Diffusion in the electrolyte and charge-transfer reaction at the platinum electrode in dye-sensitized solar cells. Electrochimica Acta 2001;46(22):3457-66.

51. Bisquert J, Vikhrenko VS. Interpretation of the Time Constants Measured by Kinetic Techniques in Nanostructured Semiconductor Electrodes and Dye-Sensitized Solar Cells. The Journal of Physical Chemistry B 2004;108(7):2313-22.

52. Bisquert J. Chemical Diffusion Coefficient of Electrons in Nanostructured Semiconductor Electrodes and Dye-Sensitized Solar Cells. The Journal of Physical Chemistry B 2004;108(7):2323-32.

53. Fabregat-Santiago F, Garcia-Belmonte G, Mora-Sero I, Bisquert J. Characterization of nanostructured hybrid and organic solar cells by impedance spectroscopy. Physical Chemistry Chemical Physics 2011;13(20):9083-118.

54. Wang Q, Ito S, Gratzel M, et al. Characteristics of High Efficiency Dye-Sensitized Solar Cells. The Journal of Physical Chemistry B 2006;110(50):25210-21.

55. Bisquert J. Theory of the Impedance of Electron Diffusion and Recombination in a Thin Layer. The Journal of Physical Chemistry B 2001;106(2):325-33.

56. Fabregat-Santiago F, Bisquert J, Garcia-Belmonte G, Boschloo G, Hagfeldt A. Influence of electrolyte in transport and recombination in dye-sensitized solar cells studied by impedance spectroscopy. Solar Energy Materials and Solar Cells 2005;87(1-4):117-31.

57. Jena A, Mohanty SP, Kumar P, et al. Dye Sensitized Solar Cells: A Review. Transactions of the Indian Ceramic Society 2012;71(1):1-16.

58. Grätzel M. Mesoporous oxide junctions and nanostructured solar cells. Current Opinion in Colloid & Interface Science 1999;4(4):314-21.

59. Lee KE, Charbonneau C, Demopoulos GP. Thin single screen-printed bifunctional titania layer photoanodes for high performing DSSCs via a novel hybrid paste formulation and process. Journal of Materials Research 2013;28(03):480-87.

60. Chou TP, Zhang Q, Russo B, Fryxell GE, Cao G. Titania Particle Size Effect on the Overall Performance of Dye-Sensitized Solar Cells. The Journal of Physical Chemistry C 2007;111(17):6296-302.

61. Zhao R, Zhu L, Cai F, et al. ZnO/TiO_2 core–shell nanowire arrays for enhanced dye-sensitized solar cell efficiency. Applied Physics A 2013:1-7.

62. Park Y, Anabuki K, Kim S, et al. Fabrication of stable electrospun TiO_2 nanorods for high-performance dye-sensitized solar cells. Macromolecular Research 2013;21(6):636-40.

63. Ghicov A, Albu SP, Hahn R, et al. TiO_2 Nanotubes in Dye-Sensitized Solar Cells: Critical Factors for the Conversion Efficiency. Chemistry – An Asian Journal 2009;4(4):520-25.

64. Stergiopoulos T, Ghicov A, Likodimos V, et al. Dye-sensitized solar cells based on thick highly ordered TiO_2 nanotubes produced by controlled anodic oxidation in non-aqueous electrolytic media. Nanotechnology 2008;19(23).

65. Stergiopoulos T, Valota A, Likodimos V, et al. Dye-sensitization of self-assembled titania nanotubes prepared by galvanostatic anodization of Ti sputtered on conductive glass. Nanotechnology 2009;20(36).

66. Vaenas N, Stergiopoulos T, Kontos AG, et al. Sensitizer activated solar cells based on self-organized TiO_2 nanotubes. Microelectronic Engineering 2012;90:62-65.

67. Huang C-Y, Hsu Y-C, Chen J-G, et al. The effects of hydrothermal temperature and thickness of TiO_2 film on the performance of a dye-sensitized solar cell. Solar Energy Materials and Solar Cells 2006;90(15):2391-97.

68. Baek IC, Vithal M, Chang JA, et al. Facile preparation of large aspect ratio ellipsoidal anatase TiO_2 nanoparticles and their application to dye-sensitized solar cell. Electrochemistry Communications 2009;11(4):909-12.

69. Park NG, van de Lagemaat J, Frank AJ. Comparison of Dye-Sensitized Rutile- and Anatase-Based TiO_2 Solar Cells. The Journal of Physical Chemistry B 2000;104(38):8989-94.

70. Fabregat-Santiago F, Barea EM, Bisquert J, et al. High Carrier Density and Capacitance in TiO_2 Nanotube Arrays Induced by Electrochemical Doping. Journal of the American Chemical Society 2008;130(34):11312-16.

71. Lee S, Noh JH, Han HS, et al. Nb-Doped TiO_2: A New Compact Layer Material for TiO_2 Dye-Sensitized Solar Cells. The Journal of Physical Chemistry C 2009;113(16):6878-82.

72. Lee KE, Gomez MA, Elouatik S, Demopoulos GP. Further Understanding of the Adsorption Mechanism of N719 Sensitizer on Anatase TiO_2 Films for DSSC Applications Using Vibrational Spectroscopy and Confocal Raman Imaging. Langmuir 2010;26(12):9575-83.

73. Hirose F, Kuribayashi K, Suzuki T, et al. UV Treatment Effect on TiO_2 Electrodes in Dye-Sensitized Solar Cells with N719 Sensitizer Investigated by Infrared Absorption Spectroscopy. Electrochemical and Solid-State Letters 2008;11(7):A109-A11.

74. Lee J-K, Jeong B-H, Jang S-i, et al. Preparations of TiO_2 pastes and its application to light-scattering layer for dye-sensitized solar cells. Journal of Industrial and Engineering Chemistry 2009;15(5):724-29.

75. Xu C, Shin PH, Cao L, Wu J, Gao D. Ordered TiO_2 Nanotube Arrays on Transparent Conductive Oxide for Dye-Sensitized Solar Cells. Chemistry of Materials 2009;22(1):143-48.

76. Qiu J, Zhuge F, Li X, et al. Coaxial multi-shelled TiO_2 nanotube arrays for dye sensitized solar cells. Journal of Materials Chemistry 2012;22(8):3549-54.

77. Luo J, Gao L, Sun J, Liu Y. A bilayer structure of a titania nanoparticle/highly-ordered nanotube array for low-temperature dye-sensitized solar cells. RSC Advances 2012;2(5):1884-89.

78. Tang F, Uchikoshi T, Ozawa K, Sakka Y. Effect of polyethylenimine on the dispersion and electrophoretic deposition of nano-sized titania aqueous suspensions. Journal of the European Ceramic Society 2006;26(9):1555-60.

79. Wu X, Lu GQ, Wang L. Shell-in-shell TiO_2 hollow spheres synthesized by one-pot hydrothermal method for dye-sensitized solar cell application. Energy & Environmental Science 2011;4(9):3565-72.

80. Kim D-W, Kim J-H, Kim K-H, et al. Preparations of Titanium Composite Electrodes from Commercial Inorganic Pigment and Its Application to Light Scattering Layers on Dye-Sensitized Solar Cells. Molecular Crystals and Liquid Crystals 2011;539(1):156/[496]-165/[505].

81. Zhang Y, Song Z, Hao J, Qiu S, Xu Z. Two new prenylated xanthones and a new prenylated tetrahydroxanthone from the pericarp of Garcinia mangostana. Fitoterapia 2010;81(6):595-99.

82. Zheng D, Lv M, Wang S, et al. A combined TiO_2 structure with nanotubes and nanoparticles for improving photoconversion efficiency in dye-sensitized solar cells. Electrochimica Acta 2012;83(0):155-59.

83. Kim AY, Kang M. High efficiency dye-sensitized solar cells based on multilayer stacked TiO_2 nanoparticle/nanotube photoelectrodes. Journal of Photochemistry and Photobiology A: Chemistry 2012;233(0):20-23.

84. Zhong P, Que W, Zhang J, et al. Charge transport and recombination in dye-sensitized solar cells based on hybrid films of TiO_2 particles/TiO_2 nanotubes. Journal of Alloys and Compounds 2011;509(29):7808-13.

85. Khamwannah J, Zhang Y, Young Noh S, et al. Enhancement of dye sensitized solar cell efficiency by composite TiO_2 nanoparticle/8nm TiO_2 nanotube paper-like photoelectrode. Nano Energy 2012;1(3):411-17.

86. Saji VS, Pyo M. Dye sensitized solar cell of TiO_2 nanoparticle/nanorod composites prepared via low-temperature synthesis in oleic acid. Thin Solid Films 2010;518(22):6542-46.

87. Ho S-Y, Su C, Kathirvel S, Li C-Y, Li W-R. Fabrication of TiO_2 nanotube–nanocube array composite electrode for dye-sensitized solar cells. Thin Solid Films 2013;529(0):123-27.

88. Demopoulos G, Charbonneau C, Lee C-H, et al. New Cost-effective Manufacture of DSSC TiO_2 Paste with Enhanced Sensitizer Anchoring Properties. 1st International Conference on Materials for Energy. Karlsruhe, Germany; July 2010

89. Yamaguchi T, Tobe N, Matsumoto D, Arakawa H. Highly efficient plastic substrate dye-sensitized solar cells using a compression method for preparation of TiO_2 photoelectrodes. Chem Commun 2007;45:4767–9.

90. Lindstrom H, Holmberg A, Magnusson E, et al. A New Method for Manufacturing Nanostructured Electrodes on Plastic Substrates. Nano Letters 2001;1(2):97-100.

91. Zhang D, Yoshida T, Oekermann T, Furuta K, Minoura H. Room-Temperature Synthesis of Porous Nanoparticulate TiO_2 Films for Flexible Dye-Sensitized Solar Cells. Advanced Functional Materials 2006;16(9):1228-34.

92. Zhang D, Yoshida T, Furuta K, Minoura H. Hydrothermal preparation of porous nano-crystalline TiO_2 electrodes for flexible solar cells. Journal of Photochemistry and Photobiology A: Chemistry 2004;164(1-3):159-66.

93. Durr M, Schmid A, Obermaier M, et al. Low-temperature fabrication of dye-sensitized solar cells by transfer of composite porous layers. Nat Mater 2005;4(8):607-11.

94. Yu J, Li Q, Shu Z. Dye-sensitized solar cells based on double-layered TiO_2 composite films and enhanced photovoltaic performance. Electrochimica Acta 2011;56(18):6293-98.

95. Kim YJ, Lee YH, Lee MH, et al. Formation of Efficient Dye-Sensitized Solar Cells by Introducing an Interfacial Layer of Long-Range Ordered Mesoporous TiO_2 Thin Film. Langmuir 2008;24(22):13225-30.

96. Chan Y-F, Wang C-C, Chen B-H, Chen C-Y. Dye-sensitized TiO_2 solar cells based on nanocomposite photoanode containing plasma-modified multi-walled carbon nanotubes. Progress in Photovoltaics: Research and Applications 2013;21(1):47-57.

97. Hore S, Vetter C, Kern R, Smit H, Hinsch A. Influence of scattering layers on efficiency of dye-sensitized solar cells. Solar Energy Materials and Solar Cells 2006;90(9):1176-88.

98. Shin K, Jun Y, Moon JH, Park JH. Observation of Positive Effects of Freestanding Scattering Film in Dye-Sensitized Solar Cells. ACS Applied Materials & Interfaces 2009;2(1):288-91.

99. Tennakone K, Bandara J, Bandaranayake PKM, Kumara GRA, Konno A. Enhanced efficiency of a dye-sensitized solar cell made from MgO-coated nanocrystalline SnO_2. Japanese Journal of Applied Physics, Part 2: Letters 2001;40(7 B):L732-L34.

100. Palomares E, Clifford JN, Haque SA, Lutz T, Durrant JR. Slow charge recombination in dye-sensitised solar cells (DSSC) using Al_2O_3 coated nanoporous TiO_2 films. Chemical Communications 2002(14):1464-65.

101. Palomares E, Clifford JN, Haque SA, Lutz T, Durrant JR. Control of Charge Recombination Dynamics in Dye Sensitized Solar Cells by the Use of Conformally Deposited Metal Oxide Blocking Layers. Journal of the American Chemical Society 2002;125(2):475-82.

102. Kay A, Grätzel M. Dye-Sensitized Core−Shell Nanocrystals: Improved Efficiency of Mesoporous Tin Oxide Electrodes Coated with a Thin Layer of an Insulating Oxide. Chemistry of Materials 2002;14(7):2930-35.

103. Kim S-S, Yum J-H, Sung Y-E. Improved performance of a dye-sensitized solar cell using a TiO_2/ZnO/Eosin Y electrode. Solar Energy Materials and Solar Cells 2003;79(4):495-505.

104. Taguchi T, Zhang X-t, Sutanto I, et al. Improving the performance of solid-state dye-sensitized solar cell using MgO-coated TiO_2 nanoporous film. Chemical Communications 2003(19):2480-81.

105. Kumara GRA, Okuya M, Murakami K, et al. Dye-sensitized solid-state solar cells made from magnesiumoxide-coated nanocrystalline titanium

dioxide films: enhancement of the efficiency. Journal of Photochemistry and Photobiology A: Chemistry 2004;164(1–3):183-85.

106. Jung HS, Lee J-K, Nastasi M, et al. Preparation of Nanoporous MgO-Coated TiO_2 Nanoparticles and Their Application to the Electrode of Dye-Sensitized Solar Cells. Langmuir 2005;21(23):10332-35.

107. Kim J, Lee S, Noh J, Jung H, Hong K. Enhanced photovoltaic properties of overlayer-coated nanocrystalline TiO_2 dye-sensitized solar cells (DSSCs). Journal of Electroceramics 2009;23(2):422-25.

108. Chou C-S, Chou F-C, Kang J-Y. Preparation of ZnO-coated TiO_2 electrodes using dip coating and their applications in dye-sensitized solar cells. Powder Technology 2012;215-216(0):38-45.

109. Chen SG, Chappel S, Diamant Y, Zaban A. Preparation of Nb_2O_5 Coated TiO_2 Nanoporous Electrodes and Their Application in Dye-Sensitized Solar Cells. Chemistry of Materials 2001;13(12):4629-34.

110. Yum J-H, Nakade S, Kim D-Y, Yanagida S. Improved Performance in Dye-Sensitized Solar Cells Employing TiO_2 Photoelectrodes Coated with Metal Hydroxides. The Journal of Physical Chemistry B 2006;110(7):3215-19.

111. Peiris TAN, Senthilarasu S, Wijayantha KGU. Enhanced Performance of Flexible Dye-Sensitized Solar Cells: Electrodeposition of $Mg(OH)_2$ on a Nanocrystalline TiO_2 Electrode. The Journal of Physical Chemistry C 2011;116(1):1211-18.

112. Xia J, Masaki N, Jiang K, Yanagida S. Sputtered Nb_2O_5 as a Novel Blocking Layer at Conducting Glass/TiO_2 Interfaces in Dye-Sensitized Ionic Liquid Solar Cells. The Journal of Physical Chemistry C 2007;111(22):8092-97.

113. Noh JH, Lee S, Kim JY, et al. Functional Multilayered Transparent Conducting Oxide Thin Films for Photovoltaic Devices. The Journal of Physical Chemistry C 2008;113(3):1083-87.

114. Chou C-S, Lin Y-J, Yang R-Y, Liu K-H. Preparation of TiO_2/NiO composite particles and their applications in dye-sensitized solar cells. Advanced Powder Technology 2011;22(1):31-42.

115. Niu H, Liu L, Wang H, et al. Significant Influence of Nano-SiO_2 on the Performance of Dye-sensitized Solar Cells Based on P25. Electrochimica Acta 2012;81(0):246-53.

116. Chappel S, Chen S-G, Zaban A. TiO_2-Coated Nanoporous SnO_2 Electrodes for Dye-Sensitized Solar Cells. Langmuir 2002;18(8):3336-42.

117. Miyasaka T, Kijitori Y. Low-Temperature Fabrication of Dye-Sensitized Plastic Electrodes by Electrophoretic Preparation of Mesoporous TiO_2 Layers. Journal of The Electrochemical Society 2004;151(11):A1767-A73.

118. Pagliaro M, Ciriminna R, Palmisano G. Flexible Solar Cells. ChemSusChem 2008;1(11):880-91.

119. Nemoto J, Sakata M, Hoshi T, Ueno H, Kaneko M. All-plastic dye-sensitized solar cell using a polysaccharide film containing excess redox electrolyte solution. Journal of Electroanalytical Chemistry 2007;599(1):23-30.

120. Pichot F, Pitts JR, Gregg BA. Low-Temperature Sintering of TiO_2 Colloids: Application to Flexible Dye-Sensitized Solar Cells. Langmuir 2000;16(13):5626-30.

121. Yamaguchi T, Tobe N, Matsumoto D, Nagai T, Arakawa H. Highly efficient plastic-substrate dye-sensitized solar cells with validated conversion efficiency of 7.6%. Solar Energy Materials and Solar Cells 2010;94(5):812-16.

122. Chang H, Chen TL, Huang KD, Chien SH, Hung KC. Fabrication of highly efficient flexible dye-sensitized solar cells. Journal of Alloys and Compounds 2010;504(Supplement 1):S435-S38.

123. Park JH, Jun Y, Yun H-G, Lee S-Y, Kang MG. Fabrication of an Efficient Dye-Sensitized Solar Cell with Stainless Steel Substrate. Journal of The Electrochemical Society 2008;155(7):F145-F49.

124. Chen H-W, Huang K-C, Hsu C-Y, et al. Electrophoretic deposition of TiO_2 film on titanium foil for a flexible dye-sensitized solar cell. Electrochimica Acta 2011;56(23):7991-98.

125. Jun Y, Kim J, Kang MG. A study of stainless steel-based dye-sensitized solar cells and modules. Solar Energy Materials and Solar Cells 2007;91(9):779-84.

126. Miettunen K, Halme J, Toivola M, Lund P. Initial Performance of Dye Solar Cells on Stainless Steel Substrates. The Journal of Physical Chemistry C 2008;112(10):4011-17.

127. Kuang D, Brillet Jrm, Chen P, et al. Application of Highly Ordered TiO_2 Nanotube Arrays in Flexible Dye-Sensitized Solar Cells. ACS Nano 2008;2(6):1113-16.

128. Toivola M, Halme J, Miettunen K, Aitola K, Lund PD. Nanostructured dye solar cells on flexible substrates—Review. International Journal of Energy Research 2009;33(13):1145-60.

129. Binner JGP. Advanced Ceramic Processing and Technology: William Andrew Publishing/Noyes; 1990.

130. Besra L, Liu M. A review on fundamentals and applications of electrophoretic deposition (EPD). Progress in Materials Science 2007;52(1):1-61.

131. Sarkar P, Nicholson PS. Electrophoretic Deposition (EPD): Mechanisms, Kinetics, and Application to Ceramics. Journal of the American Ceramic Society 1996;79(8):1987-2002.

132. Lyklema J, Overbeek JTG. On the interpretation of electrokinetic potentials. Journal of Colloid Science 1961;16(5):501-12.

133. Lyklema J. Water at interfaces: A colloid-chemical approach. Journal of Colloid and Interface Science 1977;58(2):242-50.

134. Velev OD, Bhatt KH. On-chip micromanipulation and assembly of colloidal particles by electric fields. Soft Matter 2006;2(9):738-50.

135. Zhitomirsky I. Cathodic electrodeposition of ceramic and organoceramic materials. Fundamental aspects. Advances in Colloid and Interface Science 2002;97(1-3):277-315.

136. Ohshima H. On the General Expression for the Electrophoretic Mobility of a Soft Particle. Journal of Colloid and Interface Science 2000;228(1):190-93.

137. Ohshima H. Electrophoretic mobility of soft particles. Colloids and Surfaces A: Physicochemical and Engineering Aspects 1995;103(3):249-55.

138. Derjaguin BV, Landau L. Theory of the Stability of Strongly Charged Lyophobic Sols and of the Adhesion of Strongly Charged Particles in Solutions of Electrolytes. Acta Phys. Chim. URSS 1941;14:633-62.

139. Casimir HBG, Polder D. The Influence of Retardation on the London-van der Waals Forces. Physical Review 1948;73(Copyright (C) 2010 The American Physical Society):360.

140. Ammam M. Electrophoretic deposition under modulated electric fields: a review. RSC Advances 2012;2(20):7633-46.

141. Song M-G, Bishop KJM, Pinchuk AO, Kowalczyk B, Grzybowski BA. Formation of Dense Nanoparticle Monolayers Mediated by Alternating Current Electric Fields and Electrohydrodynamic Flows. The Journal of Physical Chemistry C 2010;114(19):8800-05.

142. Ferrari B, Moreno R. The conductivity of aqueous Al_2O_3 slips for electrophoretic deposition. Materials Letters 1996;28(4-6):353-55.

143. Dor S, Rühle S, Ofir A, et al. The influence of suspension composition and deposition mode on the electrophoretic deposition of TiO_2 nanoparticle agglomerates. Colloids and Surfaces A: Physicochemical and Engineering Aspects 2009;342(1-3):70-75.

144. Ghosal S. Fluid mechanics of electroosmotic flow and its effect on band broadening in capillary electrophoresis. ELECTROPHORESIS 2004;25(2):214-28.

145. Prieve DC, Sides PJ, Wirth CL. 2-D assembly of colloidal particles on a planar electrode. Current Opinion in Colloid & Interface Science 2010;15(3):160-74.

146. Lyklema J, van Leeuwen HP, Minor M. DLVO-theory, a dynamic re-interpretation. Advances in Colloid and Interface Science 1999;83(1–3):33-69.

147. Zarbov M, Schuster I, Gal-Or L. Methodology for selection of charging agents for electrophoretic deposition of ceramic particles. Journal of Materials Science 2004;39(3):813-17.

148. Jarernboon W, Pimanpang S, Maensiri S, Swatsitang E, Amornkitbamrung V. Optimization of titanium dioxide film prepared by electrophoretic deposition for dye-sensitized solar cell application. Thin Solid Films 2009;517(16):4663-67.

149. Besra L, Uchikoshi T, Suzuki TS, Sakka Y. Bubble-Free Aqueous Electrophoretic Deposition (EPD) by Pulse-Potential Application. Journal of the American Ceramic Society 2008;91(10):3154-59.

150. Ferrari B, Moreno R. Zirconia Thick Films Deposited on Nickel by Aqueous Electrophoretic Deposition. Journal of The Electrochemical Society 2000;147(8):2987-92.

151. Van der Biest OO, Vandeperre LJ. Electrophoretic deposition of materials. Annual Review of Materials Science 1999;29(1):327-52.

152. Lebrette S, Pagnoux C, Abélard P. Fabrication of titania dense layers by electrophoretic deposition in aqueous media. Journal of the European Ceramic Society 2006;26(13):2727-34.

153. Hayward RC, Saville DA, Aksay IA. Electrophoretic assembly of colloidal crystals with optically tunable micropatterns. Nature 2000;404(6773):56-59.

154. Neirinck B, Fransaer J, Biest OVd, Vleugels J. Aqueous electrophoretic deposition in asymmetric AC electric fields (AC–EPD). Electrochemistry Communications 2009;11(1):57-60.

155. Uchikoshi T, Suzuki TS, Iimura S, Tang F, Sakka Y. Control of crystalline texture in polycrystalline TiO_2 (Anatase) by electrophoretic deposition in a strong magnetic field. Journal of the European Ceramic Society 2006;26(4-5):559-63.

156. Ma J, Cheng W. Deposition and packing study of sub-micron PZT ceramics using electrophoretic deposition. Materials Letters 2002;56(5):721-27.

157. Yoshida T, Komatsu D, Shimokawa N, Minoura H. Mechanism of cathodic electrodeposition of zinc oxide thin films from aqueous zinc nitrate baths. Thin Solid Films 2004;451-452:166-69.

158. Zhang L, Chen Z, Tang Y, Jia Z. Low temperature cathodic electrodeposition of nanocrystalline zinc oxide thin films. Thin Solid Films 2005;492(1–2):24-29.

159. Solomentsev Y, Böhmer M, Anderson JL. Particle Clustering and Pattern Formation during Electrophoretic Deposition: A Hydrodynamic Model. Langmuir 1997;13(23):6058-68.

160. Kawakita M, Uchikoshi T, Kawakita J, Sakka Y. Preparation of Crystalline-Oriented Titania Photoelectrodes on ITO Glasses from a 2-Propanol-2,4-Pentanedione Solvent by Electrophoretic Deposition in a Strong Magnetic Field. Journal of the American Ceramic Society 2009;92(5):984-89.

161. Grinis L, Dor S, Ofir A, Zaban A. Electrophoretic deposition and compression of titania nanoparticle films for dye-sensitized solar cells.

Journal of Photochemistry and Photobiology A: Chemistry 2008;198(1):52-59.

162. Zhao L, Yu J, Fan J, Zhai P, Wang S. Dye-sensitized solar cells based on ordered titanate nanotube films fabricated by electrophoretic deposition method. Electrochemistry Communications 2009;11(10):2052-55.

163. Kim G-S, Seo H-K, Godble VP, et al. Electrophoretic deposition of titanate nanotubes from commercial titania nanoparticles: Application to dye-sensitized solar cells. Electrochemistry Communications 2006;8(6):961-66.

164. Manríquez J, Godínez LA. Tuning the structural, electrical and optical properties of Ti(III)-doped nanocrystalline TiO_2 films by electrophoretic deposition time. Thin Solid Films 2007;515(7-8):3402-13.

165. Lebrette S, Pagnoux C, Abélard P. Stability of aqueous TiO_2 suspensions: influence of ethanol. Journal of Colloid and Interface Science 2004;280(2):400-08.

166. Tabellion J, Clasen R. Electrophoretic deposition from aqueous suspensions for near-shape manufacturing of advanced ceramics and glasses—applications. Journal of Materials Science 2004;39(3):803-11.

167. Tan W, Yin X, Zhou X, et al. Electrophoretic deposition of nanocrystalline TiO_2 films on Ti substrates for use in flexible dye-sensitized solar cells. Electrochimica Acta 2009;54(19):4467-72.

168. Abdullah HZ, Sorrell CC. TiO_2 Thick Films by ElectrophoreticDeposition. Journal of the Australian Ceramic Society 2008;44(2):12-16.

169. Lin CK, Yang TJ, Feng YC, Tsung TT, Su CY. Characterization of elecrophoretically deposited nanocrystalline titanium dioxide films. Surface and Coatings Technology 2006;200(10):3184-89.

170. Zaban A, Grinis L, Ofir A, inventors; Barilan University assignee. Method for production of nanoporous electrods for photoelectrochemical applications. H01L31/042; C09D5/44 ed: Barilan University 2009.

171. Murakami TN, Kijitori Y, Kawashima N, Miyasaka T. Low temperature preparation of mesoporous TiO_2 films for efficient dye-sensitized photoelectrode by chemical vapor deposition combined with UV light irradiation. Journal of Photochemistry and Photobiology A: Chemistry 2004;164(1-3):187-91.

172. Chiu W-H, Lee K-M, Hsieh W-F. High efficiency flexible dye-sensitized solar cells by multiple electrophoretic depositions. Journal of Power Sources 2011;196(7):3683-87.

173. Hanaor D, Michelazzi M, Veronesi P, et al. Anodic aqueous electrophoretic deposition of titanium dioxide using carboxylic acids as dispersing agents. Journal of the European Ceramic Society 2011;31(6):1041-47.

174. Ofir A, Dittrich T, Tirosh S, Grinis L, Zaban A. Influence of sintering temperature, pressing, and conformal coatings on electron diffusion in electrophoretically deposited porous TiO_2. Journal of applied physics 2006;100:074317.1-17.6.

175. Sommeling PM, O'Regan BC, Haswell RR, et al. Influence of a $TiCl_4$ Post-Treatment on Nanocrystalline TiO_2 Films in Dye-Sensitized Solar Cells. The Journal of Physical Chemistry B 2006;110(39):19191-97.

176. Miyasaka T, Kijitori Y, Murakami TN, Kawashima N. Fabrication of dye-sensitized plastic film electrodes for flexible solar cells based on electrophoretic deposition techniques. Paper presented at, 2004; San Diego, CA, USA: SPIE.

Chapter 3. Enabling aqueous electrophoretic growth of adherent nanotitania mesoporous films via intrafilm cathodic deposition of hydrous zinc oxide

In this first of 4 papers-chapters series, detailed studies are described with reference to the development of a water-based (aqueous) electrophoretic deposition system for the growth of adherent nanotitania mesoporous films on conductive (FTO) glass substrate. In this regard: 1) parameters and properties related to the suspension formulation (zeta potential, surface tension, charging agent and particle concentration) have been systematically studied and optimized; 2) the influence of EPD related parameters to successfully deposit a robust and adherent film from aqueous suspension have also been investigated; 3) the kinetics and mechanism of TiO_2-ZnO film deposition determined; and 4) the morphology, chemical composition and optical properties of the deposited films were characterized. This chapter –with the same title- and co-authored by Nima Parsi Benehkohal, Mario A. Gomez, Raynald Gauvin, and George P. Demopoulos has been published in *Electrochimica Acta 87 (2013) 169– 179.*

3.1. Abstract

By far the majority of previous electrophoretic deposition (EPD) works employ organic solvent media and additives that impose environmental challenges to large-scale implementation. Here EPD in water is investigated instead. In particular via the adoption of a low DC voltage approach mesoporous films of nanotitania are successfully grown by aqueous EPD of the commercial P25 mixed phase TiO_2 product on FTO-glass as substrate. Growth of adherent and robust films is enabled via the use of isopropanol as co-solvent and $Zn(NO_3)_2$ as additive, the latter leading to co-deposition of hydrous zinc oxide that acts as nanoglue. The optimization of the suspension composition, mechanism of zinc co-deposition with TiO_2, and the structural and electronic properties of the resultant TiO_2-ZnO semiconductor films are described. Under galvanostatic EPD regime, zinc co-deposition occurs initially (first 15 s) as $Zn(OH)_2$ via the cathodic (NO_3^- *to* NO_2^- reduction) interfacial generation of OH^-. Upon rise of the cathodic potential with increasing film thickness, nanosized metallic zinc co-deposits uniformly throughout the film profile (~2% Zn content). As such $Zn(OH)_2$ and metallic nanozinc that partially oxidizes *in situ* act as intrafilm nanoglue. After annealing at 450 ºC the nanocomposite TiO_2–ZnO film exhibits blue-shifting and abundant hydroxyl surface coverage that are desirable in photocatalytic applications.

3.2. Introduction

Titanium dioxide nanomaterials are currently investigated and applied in various advanced fields, including environmental photocatalysis [1], self-cleaning surfaces [2], energy storage [3], solar fuels [4], and photovoltaics [5]. In many of these applications the nanotitania material is deposited on substrates to form mesoporous films, as is the case of dye-sensitized solar cells[6]. The deposition of the titania nanocrystallites to form mesoporous films (~10-15 microns thick) typically is accomplished by screen-printing [7]. Alternatively as means of

simplifying and hence lowering the cost of the mesoporous film fabrication operation the application of EPD can be considered [8].This is so because EPD is a high throughput technique that allows fast deposition rates, good film growth control and adaptability to various substrates including conductive plastic materials [9-10]. However in most of these EPD methods, organic solvents and toxic additives are used [8, 11], which complicate their large scale application. Use of water as solvent is preferred but this has been hampered by the use of high DC voltages that cause its decomposition and gas evolution preventing the growth of good quality mesoporous films. Different approaches have been reported to make aqueous EPD feasible such as addition of a co-solvent to suppress the water electrolysis reaction [12], working with a voltage below the threshold for water electrolysis [13], or by applying pulse potential [14-15] or AC-electric field [16].

In this study, the low DC voltage approach is adopted in building mesoporous films of nanotitania by aqueous EPD of the commercial P25 TiO_2 product on FTO-glass as substrate. In order to overcome the problems of film adhesion and quality arising from water electrolysis several measures were taken, namely judicious selection of EPD parameters (particularly applied voltage), use of isopropanol as co-solvent and more importantly the use of $Zn(NO_3)_2$ as additive. The latter measure was the most critical to overcome the poor adhesion of the film to the substrate. Under low electric field (due to low voltage), EPD does not lead to good physical attachment of particles to the substrate, hence the need for a chemical-assisted mode of attachment. The use of $Zn(NO_3)_2$ as additive serves three purposes, first in charging the TiO_2 particles, second in depositing $Zn(OH)_2$ [17-19] that acts as nanoglue, and third in producing TiO_2-ZnO composite semiconductor films upon annealing. Recently we reported the fabrication of mesoporous TiO_2-ZnO electrodes for dye-sensitized solar cell (DSSC) application by employing our aqueous EPD system [20]. We reported that in-situ formation of ZnO causes suppression of charge recombination at the substrate/electrolyte and TiO_2/electrolyte interfaces thus leading to enhanced photovoltaic performance. Other researchers have reported on the enhanced photocatalytic activity of the

TiO_2-ZnO couple owing to inhibition of the recombination of electron–hole pairs [21-23]. It is the scope of the present study to investigate, optimize, and elucidate the mechanism of the cathodic deposition of hydrous zinc oxide in building robust TiO_2-ZnO mesoporous films by aqueous EPD hence enabling development of green semiconductor film fabrication processes. In this regard, parameters and properties related to the suspension formulation (zeta potential, surface tension, charging agent and particle concentration) have been systematically studied; the morphology, chemical composition and optical properties of the film characterized with various techniques, including, FEG-SEM, XRD, XPS, and UV-Vis; and the kinetics and mechanism of TiO_2-ZnO film deposition determined.

3.3. Experimental

3.3.1. Suspension preparation and EPD parameters

The suspension (200 *mL*) consisted of de-ionized water containing different amounts of isopropanol (0-40% *v/v*) in which variable quantities (2-20 $g.L^{-1}$) of TiO_2 powder (AEROXIDE® TiO_2 P25, Evonic) were added. In addition various amounts (10^{-4} – 10^{-2} M) of $Zn(NO_3)_2.6H_2O$ were tested. It is worthy to note that we tested different zinc salts such as zinc sulfate and zinc acetate and chose zinc nitrate among them since the others did not provide enough suspension stability apparently due to complex formation and incomplete dissociation. The suspension was first mixed for 75 minutes with a magnetic stirrer and after for 15 minutes with an ultrasonic stirrer prior to EPD. Constant current density (0.05-0.2 $mA.cm^{-2}$) was applied between a stainless steel sheet (anode) and a fluorine-doped tin-oxide conducting glass substrate (FTO-Glass, 7 $\Omega.cm^{-2}$, Nippon Sheet Glass, Japan). This current density range was tested with the purpose of selecting the low cell voltage (2.5-3.2 *V*) that minimizes water decomposition. The distance between the two electrodes was 2 *cm*. The deposition area of the photoelectrode was 5 cm^2. A Keithley 2400 Source Meter was used as a power supply. Ambient

temperature deposition was performed for different times over the range of 2-30 min. After each deposition test the TiO_2 coated FTO-glass electrode was taken out of the electrophoretic cell and let dry at room temperature, before subjected to characterization and annealing. The nanotitania films were annealed at 450°C in air for 30 min [24]. To investigate the mechanism of zinc co-deposition the potential of the cathode was monitored with a Ag/AgCl reference electrode. In addition zinc was electrodeposited on the FTO glass with a 3-electrode system employing a Ag/AgCl reference electrode and platinum wire as counter electrode at different constant cathodic potential applied via a VSP-potentiostat system (BioLogic).

3.3.2. Suspension characterization

The surface tension of the suspension was measured with a Krauss K-12 Tensiometer using the Wilhelmy Plate method. The zeta potential and suspension conductivity were measured with a Malvern Zetasizer Nano ZS (Malvern Instruments) and an Oakton conductivity meter, respectively. Sedimentation tests were also carried out by measuring absorbance at λ = 420 nm vs. time for different particle concentrations (corrected for the blank solution of 5% v/v isopropanol - deionized water mixture) using an Evolution 300 UV-Visible spectrometer.

3.3.3. Mesoporous film characterization

The thickness of TiO_2 film was measured using a Dektak 3030 surface profiler system (Veeco Instruments). The morphology of the TiO_2 films was investigated using a field emission scanning electron microscope FE-SEM (S-4700 Hitachi) and also the cold-FEG-SEM Hitachi SU-8000. X-ray diffraction (XRD) was carried out using a Bruker D8 diffractometer equipped with a GADDS 2D detector and Cu Kα radiation (λ = 0.15406 nm) at a scan rate of 5°/min. The optical properties of the films were investigated by measuring the diffusive reflectance at room temperature with a PV Measurements Inc Quantum Efficiency

system, model QEX10. X-ray photoelectron spectroscopy (XPS) and the $L_3M_{45}M_{45}$ Auger electron spectra (AES) measurements were performed and collected with a Thermo Scientific K-Alpha instrument, using an Al Kα X-ray source at 1486.6 *eV*. Spectra were generated at a perpendicular takeoff angle, using a pass energy of 20 *eV* and steps of 0.1 *eV*. During analysis, the pressure was in the order of $\sim 10^{-10}$ Torr. Ar^+ ion bombardment with energy of 2 *keV* for 30 *s* was carried out prior to collecting the spectra in order to remove any charging effects from carbon-based contaminants. As an internal reference for the absolute binding energies, the Au ($4f_{7/2}$) peak was used. The experimental spectra were de-convoluted after subtraction of the Shirley background using the VG Avantage program. In order to determine the weight percentage zinc content of the TiO_2 deposited film, the film was immersed (24 h) in acidic (2M HCl) solution and the latter analysed by atomic absorption (AA) using a Varian Atomic Absorption spectrometer. Photocatalytic activities of both composite TiO_2-ZnO and TiO_2 nanoparticles were carried out by observing the degradation of (methyl orange) MO under UV light. In this regard, 50 *mg* powder, which was scratched off the deposited TiO_2-ZnO and TiO_2 films, was added to 50 *mL* of aqueous MO solution in a 100 *mL* beaker, with an initial MO concentration of 10 $mg.L^{-1}$. The solution was stirred in the dark for 60 min for adsorption–desorption equilibrium. The dye-loaded powder solution suspension was placed at 6 cm distance from UV light source inside a closed chamber, and irradiated for 60 min. 5 *mL* of irradiated solution was taken every 15 minute, centrifuged and subjected to absorption measurement. The MO solution, without powder present, gives an absorption peak (A_0) at 464 nm. The photocatalytic degradation efficiency was calculated via the following equation 0-1[25]:

$$\%D = \left(\frac{A_0 - A_t}{A_0} \right) * 100 \qquad (0\text{-}1)$$

where, A_t is the absorption peak of the MO solution after being irradiated for the aforementioned period.

3.4. Results and Discussion

3.4.1. Optimization of suspension and EPD parameters

3.4.1.1. Suspension formulation

Isopropanol content: Obtaining a uniform, adherent and robust deposit is dependent largely on the composition and properties of the suspension. Hence, characterization and optimization of suspension properties in terms of high colloid stability and low surface tension, conductivity and viscosity is of paramount importance [26]. Since our goal was to develop an aqueous suspension we opted to reduce surface tension and conductivity by using isopropanol (2-propanol). This is so because isopropanol is better suited for larger scale application rather than other lower molecular weight (MW) alcohols [8] due to its higher boiling point (better plant hygiene), its easier recovery-recycling via low cost azeotropic mixture distillation, and electrochemical stability [27]. In this regard, various isopropanol/water media (5-40% *v/v*) were prepared and characterized as shown in Table 0-1. As it can be seen the first effect of adding isopropanol to water was reduction of the surface tension, which is desirable in EPD as it avoids film cracking by minimizing capillary stresses [28]. In addition, the conductivity decreased progressively with increasing isopropanol content. A lower conductivity is preferable since it enables deposition at higher rate as well as working with a lower electric field, which is the case of the present system. On the other hand, increasing isopropanol content caused a reduction in zeta potential, which is undesirable as destabilizes the suspension hence adversely affecting particle deposition and adhesion as confirmed by EPD tests-described below. The reduction in zeta potential is significant, however only at higher than 5 vol.% isopropanol content. Along the line of thought of Lebrette et al. [29], it is postulated that the isopropanol molecules populate the particle/solvent interface (as indirectly evident by the surface tension results as well) disturbing the electrical double layer structure hence the lowering of zeta potential. Finally, it can be seen with the data of Table 0-1 that the electrophoretic mobility of TiO_2

particles decreases with increasing isopropanol content reflecting the decreasing dielectric constant, zeta potential, and increasing viscosity of the medium. A lower mobility can adversely affect the deposition rate and hence adhesion as discussed in the next paragraph.

Zn-free EPD: EPD tests were attempted with all above suspensions containing various amounts of isopropanol. The EPD conditions applied were: 5 $g.L^{-1}$ TiO_2, i=0.01-0.2 $mA.cm^{-2}$ and t=0.5-3 min. It was possible to obtain a deposit only with 0% and 5 %*v/v* isopropanol-water mixture, however the results were not reproducible. EPD failed to form any deposit from suspensions containing 10%*v/v* isopropanol or higher. It is noted that in the lower concentration range of isopropanol (5 *v*% isopropanol), the film sometimes fell off the substrate, when it was taken out of the suspension, but in higher (10 *v*% isopropanol and more) concentration range, the film fell off even during EPD. It is clear therefore, that adhesion was very poor becoming nil with increasing isopropanol content. It is postulated that the low particle mobility in combination with the low applied electric field failed to generate substantial particle-substrate collision, a condition favoring physical attachment. This led to the exploration of a chemical-induced adhesion process as described in the following section.

Table 0-1: The influence of isopropanol content on aqueous suspension properties (5 $g.L^{-1}$ TiO_2 and without any $Zn(NO_3)_2$)

Isopropanol (vol.%)	*Surface Tension ($10^{-3}N.m^{-1}$)*	*Zeta Potential (mV)*	*Mobility ($10^{-4}cm^2.V^{-1}s^{-1}$)*	*Suspension pH*	*Conductivity ($10^{-3}S.cm^{-1}$)*	*Viscosity (cP)*	*Dielectric Constant* [30]
0	72.6±0.8	29.0±0.5	2.24±0.03	4.1	0.042±0.004	0.89	78.5
5	49.7±0.7	28.3±0.9	1.71±0.07	4.0	0.031±0.002	1.09	74.9
10	40.0±1.4	22.0±2.1	1.01±0.06	4.0	0.027±0.003	1.37	71.4
20	31.3±0.9	23.8±1.0	0.65±0.02	4.0	0.024±0.002	2.06	64.1
30	27±1.2	22.9±1.1	0.42±0.02	4.1	0.016±0.002	2.77	56.9
40	25.2±1.1	19.1±0.8	0.25±0.03	4.1	0.012±0.001	3.29	49.7

Zinc Nitrate Additive: Considering all issues mentioned above, the 5%*v/v* isopropanol -water solvent system was chosen for investigating the role of zinc nitrate as additive. First its effect as charging agent in increasing the stability of the suspension (5 $g.L^{-1}$ P25 TiO_2) is considered. Plots of suspension zeta potential vs. pH for different concentrations of $Zn(NO_3)_2$ are shown in Figure 0-1. The best suspension stability was obtained with 10^{-3} M $Zn(NO_3)_2$ corresponding to a zeta potential of 36.5 mV at pH 4 (Table 0-1)-the natural pH of the suspension. The increased zeta potential (36.5 mV vs. 28.3 mV) as well as the shift of the isoelectric point (IEP) to higher pH with increasing concentration can be attributed to specific Zn^{2+} adsorption on the surface of particles, similar to observations made by Tang et al. [31]. The zeta potential however, decreased upon further concentration increase (19.3 mV at 10^{-2} M and 4.4 suspension pH [20]). High salt concentration tends to compress the double layer leading to zeta potential decrease and suspension instability. In short, 5 % *v/v* isopropanol-water mixture containing 10^{-3} M $Zn(NO_3)_2$ was retained for the rest of our experiments as an optimum suspension medium.

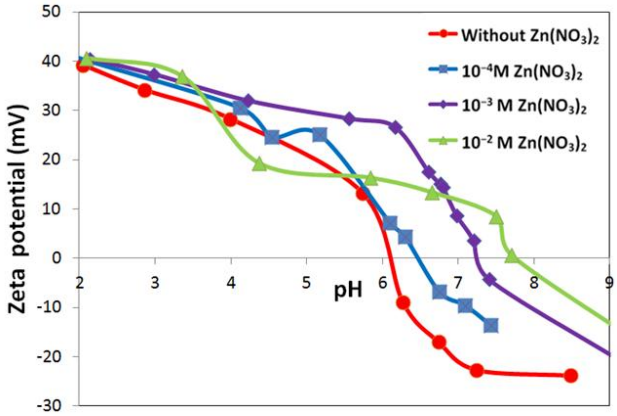

Figure 0-1. Zeta potential of TiO_2 nanoparticles (5 $g.L^{-1}$ P25) as a function of pH in the 5%*v/v* isopropanol-water suspension containing different amounts of $Zn(NO_3)_2$

3.4.1.2. Selection of current density

By performing a series of galvanostatic EPD tests with the optimized suspension formulation over a range of current densities (0.05-0.2 $mA.cm^{-2}$), it was determined that 0.1 $mA.cm^{-2}$ was the upper limit in terms of minimized water decomposition and obtainment of good quality, uniform and adhesive film (see Figure 0-2). Further increase in current density caused formation of bubbles and deterioration of film quality. Hence 0.1 $mA.cm^{-2}$ was selected, since it offered the best compromise between accelerated particle flux needed for good film adhesion and packing on one hand and avoidance/minimization of bubble formation due water electrolysis on the other.

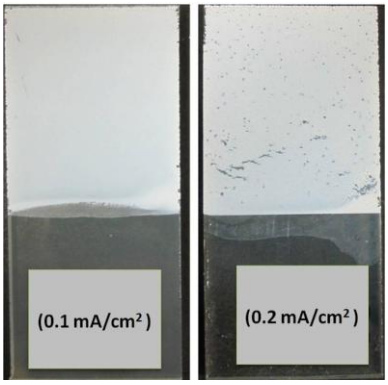

Figure 0-2. The effect of current density on TiO_2-ZnO composite film quality (~15 μm). The "footprints" (upper right) of bubbles formed at 0.2 $mA.cm^{-2}$ are clearly shown. The deposition area is about 2cm*2.5 cm.

3.4.1.3. Effect of particle concentration

A range of TiO_2 particle concentrations was investigated in 5 % *v/v* isopropanol-water mixture containing $Zn(NO_3)_2$. The measured pH of the suspension decreased from pH 4.2 with 2 $g.L^{-1}TiO_2$ to pH 3.6 with 20 $g.L^{-1}$ TiO_2, which is in agreement with others [32]. The pH decrease with increasing TiO_2 concentration is attributed to the well known phenomenon of metal oxide surface hydrolysis [33]. In terms of potential determining ions, Zn^{2+} ions supersede protons because of their higher charge and concentration, almost one order of magnitude

(10^{-3} M Zn^{2+} vs. $10^{-3.6 \text{ to } 4.2}$ M H^{+}). Attempts to electrophoretically grow films at particle concentrations higher than 5 $g.L^{-1}$, when the concentration of $Zn(NO_3)_2$ was constant at 10^{-3} M, however failed. Thus it was decided proportionally to increase the $Zn(NO_3)_2$ concentration as well in order to keep the same ratio of $[Zn(NO_3)_2]/ [TiO_2]$ (=10^{-3} M Zn^{2+}/5 $g.L^{-1}$ TiO_2). Under these conditions, formation of continuous films was feasible for all particle concentrations tried. This can be verified with the SEM images of film cross sections in Figure 0-3. However at high particle concentration (most evident at 20 $g.L^{-1}$-Figure 0-3 (d)) the uniformity of the film deteriorated significantly. This was traced to large aggregate formation as evident with the sedimentation measurements reported in Figure 0-4. As it can be seen the settling rate increased markedly above 5 $g.L^{-1}$ particle concentration, hence this concentration was selected. By comparison similar particle concentrations or even lower are reported for EPD systems involving organic media [8, 26, 34]. On the other hand, the aqueous EPD grown films were found to form cracks (evident in Figure 0-3) during the drying process as a result of the stresses induced from the evaporation of the intrafilm trapped water. As we showed in our previous study [20] the occurrence of cracking can be greatly minimized by adopting multilayer deposition involving repeated cycles of thin layer EPD and intermittent drying.

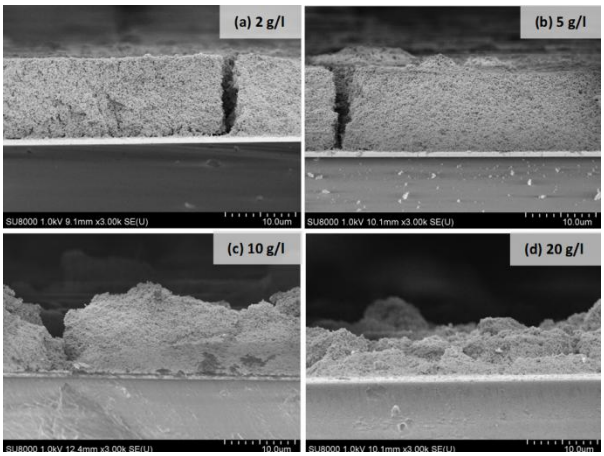

Figure 0-3. Cross sections of films deposited from suspensions with different TiO_2 particle concentrations and constant ratio of 10^{-3} M Zn/ 5 $g.L^{-1}$ TiO_2 (taken with the S-4700 Hitachi).

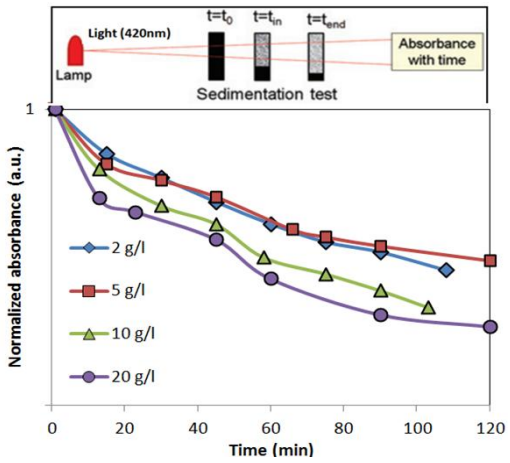

Figure 0-4. The influence of particle concentration on the sedimentation of TiO_2 nanoparticle suspensions, natural pH. The ratio of $Zn(NO_3)_2$/ particle concentration was constant for all suspensions equal to 10^{-3} M Zn/5 $g.L^{-1}$

3.4.2. EPD Kinetics

The use of $Zn(NO_3)_2$ as additive led to co-deposition of TiO_2 with zinc (the exact type of zinc compound and mechanism of deposition is discussed in the next section). Chemical analysis of the deposited films at different times yielded the results summarized in Table 0-2. Interestingly, the weight percentage of deposited zinc was found to be ~ 2 % and independent of the deposition time, which is in a good agreement with previous observations [35]. This represents only a minor fraction of the available in solution zinc, namely <1.3%. Therefore, it can be concluded that zinc deposited uniformly along the entire film as verified in our pervious study by EDS analysis of the cross section of the film [20].

Table 0-2: Deposited mass of TiO_2 and zinc at different deposition times; 5 % *v/v* isopropanol-water system, 5 $g.L^{-1}$ TiO_2 concentration, and 10^{-3} M $Zn(NO_3)_2$ under 0.1 $mA.cm^{-2}$ constant current density

Deposition time (s)	***Deposited TiO_2 ($mg.cm^{-2}$)***	***Deposited Zn ($mg.cm^{-2}$)***	***Deposited Zn % Wt.***
300	0.526±0.014	0.00957±0.0009	1.82±0.06
600	0.850±0.05	0.0163±0.0022	1.92±0.04
1050	1.450±0.07	0.0284±0.0019	1.96±0.02
1200	1.659±0.08	0.0331±0.0024	2.00±0.03

The TiO_2 deposition kinetics was determined in terms of yield vs. time and film thickness vs. time and presented in the plots of Figure 0-5. The yield was obtained by weighing the electrode before and after deposition at different EPD times, while film thickness was evaluated with a profiler system. As it can be seen deposition and film growth progressed linearly reflecting the fact that EPD was performed at constant current density [8]. The absence of deviation from linearity with increasing time further indicates that not significant depletion in particle concentration has taken place within the time of the test [26]. This is true as it was calculated that after 20 min deposition only ~0.8% of the particles had deposited.

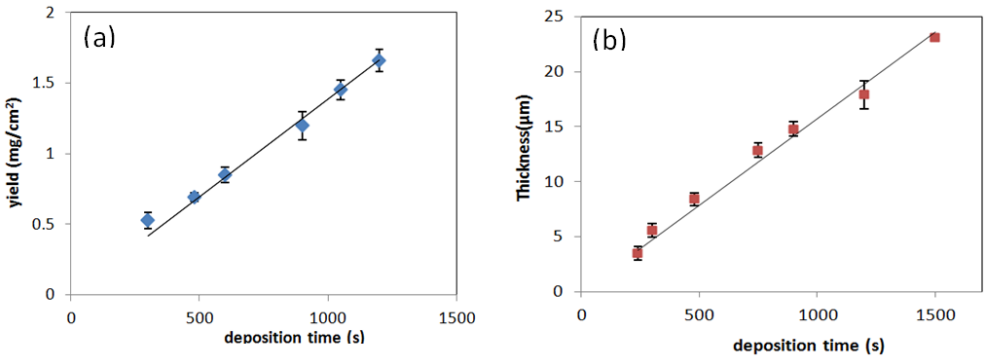

Figure 0-5. (a) Deposition yield, and (b) thickness of TiO_2 films as function of deposition time; 5 % *v/v* isopropanol-water mixture, 5 $g.L^{-1}$ TiO_2 and 10^{-3} M $Zn(NO_3)_2$ under 0.1 $mA.cm^{-2}$ constant current density

The theoretical deposition rate (assuming 100 % efficiency, or f=1) can be calculated with the aid of the Hamaker equation 0-2[8, 36]:

$$\frac{dY}{S.dt} = f\mu cE \qquad (0\text{-}2)$$

Here Y (mg) is yield, t (s) is time, S is the electrode surface area (5 cm^2), μ is electrophoretic mobility (=2.29 $\bullet 10^{-4}$ $cm^2.V^{-1}.s^{-1}$), c *is* particle concentration (5 $mg.cm^{-3}$), and E is electric field (average value = 1.347±0.35 $V.cm^{-1}$). Using these values the theoretical deposition rate of TiO_2 was calculated to be 0.0077 $mg.cm^{-2}.s^{-1}$. By comparison the actual deposition rate obtained from the plot in Figure 0-5 was 0.0014 $mg.cm^{-2}\ s^{-1}$ (or 14 $\bullet 10^{-7}$ $g.cm^{-2}.s^{-1}$), i.e. 18% (f=0.18) of the theoretical rate. Thus, it can be concluded that just 18% of the particles driven to the electrode actually deposited. The relatively low efficiency reflects (at least in part), as pointed out by Hamaker [37] the fact that at low voltage (below 20 V) particle deposition becomes less effective.

3.4.3. Mechanistic aspects

Electrode polarization: In order to elucidate what exactly is happening at the suspension/cathode interface especially in relation to the mechanism of zinc deposition we investigated the variation of potential and characterized the deposit by various techniques. According to Van der Biest et al. [34], the potential drop over an EPD cell with equal surface area electrodes generally consists of four components (Figure 0-6 (a)):

$$V_a = \Delta\emptyset_1 + \Delta\emptyset_{dep} + \Delta\emptyset_{susp} + \Delta\emptyset_2 \qquad (0\text{-}3)$$

$$\Delta\emptyset_1 = (e_{eq,\,cathode} + \eta_{cathode}) \qquad (0\text{-}4)$$

$$\Delta\emptyset_2 = (e_{eq,anode} + \eta_{anode}) \qquad (0\text{-}5)$$

Where V_a is the applied cell potential, $\Delta\emptyset_1$ and $\Delta\emptyset_2$ are the cathode and anode interfacial potentials, $\Delta\emptyset_{dep}$ is the potential drop across the deposited film and $\Delta\emptyset_{susp}$ is the potential drop in the suspension. $\Delta\emptyset_1$ is the algebraic sum of the

equilibrium potential of the cathodic reaction ($e_{eq,cathode}$) and the cathodic overpotential ($\eta_{cathode}$); the latter can be of the activation type, concentration type or a mixture of the two. The total cathodic potential ($\Delta\emptyset_{cath,total}$) is the sum of $\Delta\emptyset_1$ and $\Delta\emptyset_{dep}$. $\Delta\emptyset_{cath,total}$ and $\Delta\emptyset_2$ were measured by using the Ag/AgCl reference electrode at the surface of the cathode film and the anode, respectively and plotted (w.r.t. SHE) in Figure 0-6 (b). $\Delta\emptyset_{susp}$ was evaluated indirectly by monitoring the voltage difference between the anode electrode and the reference electrode placed near the cathode face, i.e. by measuring $\Delta\emptyset_{susp}+\Delta\emptyset_2$ and subtracting from it the independently measured anode potential $\Delta\emptyset_2$. From these measurements, $\Delta\emptyset_{susp}$ was determined to be essentially constant at about 0.2 V reflecting the essentially constant composition of the aqueous suspension.

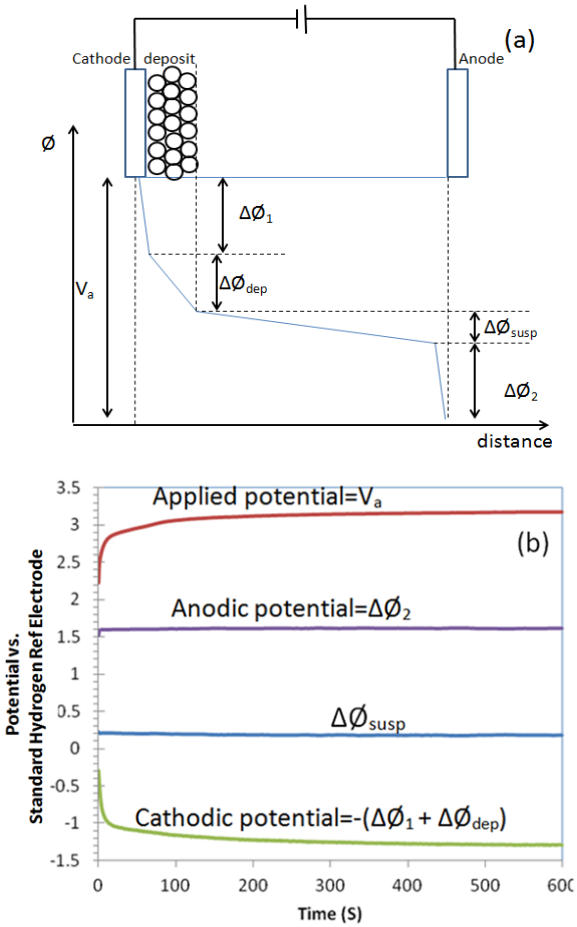

Figure 0-6. (a) Electrochemical potential profile in an EPD cell and (b) potential (vs. SHE) variation as a function of EPD time at a costant applied current density (0.1 $mA.cm^{-2}$)

As shown in Figure 0-6 (b), the anodic potential remained essentially constant at 1.6 *V* during the course of deposition. This potential corresponds to the oxygen evolution reaction. By taking into account the equilibrium potential of the O_2/H_2O couple (corresponding to pH 4, the pH of the suspension), then the anodic overpotential is estimated at ~0.6 *V*, which is typical for the oxygen reaction on the surface of stainless steel. However, the total cathodic potential ($\Delta\emptyset_1 + \Delta\emptyset_{dep}$) is seen to increase with the progress of deposition. Such increase may be due to different reasons such as the increasing resistance of the growing deposit, changes in cathodic polarization, and/or a progressive decrease in the suspension conductivity [34].

Of these possible reasons the first one at all likelihood applies here. First, in terms of the suspension conductivity, $\Delta\emptyset_{susp}$, this was relatively constant throughout the deposition cycle (as seen in Figure 0-6 (b)) reflecting the fact, as already noted earlier, that there was negligible zinc nitrate (major charging agent) consumption (~2%) during EPD. Second, in terms of cathodic polarization, we estimated the limiting current densities of Zn^{2+}, NO_3^-, and H^+($1.9 \bullet 10^{-4}$ $mA.cm^{-2}$ for the first two and $9.6 \bullet 10^{-3}$ $mA.cm^{-2}$ for H^+) to be cumulatively only a small fraction (~1/10) of the applied current density. In other words all important ions (see next section) were under concentration overpotential control throughout the EPD cycle hence could not have been the origin of the observed increase in cathodic potential. Therefore, it can be concluded that the cell voltage rise during EPD can be attributed to voltage drop ($\Delta\emptyset_{dep}$) across the growing EPD film.

Cathodic reactions: There are three possible primary cathodic reactions that may occur in the present system as described by equations 3-6, 3-7 and 0-8. Reaction 0-6 represents the evolution of hydrogen ($e_{eq,H^+/H_2} = -0.228V$) that also leads to local pH rise due to OH^- generation [17, 19, 38]. This reaction is considered to be, however significantly suppressed in the present system due to co-deposition of zinc on the surface of which hydrogen exhibits a very large activation

overpotential [39]. Reaction 0-7 represents the reduction of nitrate ions to nitrite ions ($e_{eq,NO_3/NO_2^-} = 0.5026V$) that also leads to localized OH^- generation [40-41]. It is interesting to note that Zn^{2+} ions were reported to play a catalytic role in reaction 0-7 [40]. Finally, another possible cathodic reaction that has not received the necessary attention previously is the formation of metallic zinc (equation 8; $e_{eq,Zn^{2+}/Zn} = -0.849V$). This is a distinct possibility given in particular the continuous decrease of cathodic potential with the progress of deposition (Figure 0-6 (b)) that was experimentally verified as described in the next section.

$$2H_2O + 2e^- \rightarrow H_2 + 2OH^- \qquad (0\text{-}6)$$

$$NO_3^- + H_2O + 2e^- \rightarrow NO_2^- + 2OH^- \qquad (0\text{-}7)$$

$$Zn^{2+} + 2e^- \rightarrow Zn \qquad (0\text{-}8)$$

Upon interfacial pH increase as result of the cathodic generation of OH^- (Equation 0-6 and 0-7), it is postulated that zinc hydroxide forms (Equation 0-9) acting as binder for the physically deposited TiO_2 particles hence promoting the building of an adherent film. Furthermore, $Zn(OH)_2$ (or hydrous zinc oxide: $ZnO \bullet H_2O$) is thought to transform into ZnO during annealing. The postulated formation of the different zinc species is confirmed in the characterization section that follows.

$$Zn^{2+} + 2\,OH^- \rightarrow Zn(OH)_2 \xrightarrow{Annealing} ZnO \qquad (0\text{-}9)$$

Zn^{2+} to Zn metal reduction: In order to verify whether the reduction of Zn^{2+} to Zn metal were feasible during EPD, it was decided to carry out electrodeposition tests with a 5 %*v/v* isopropanol/water solution containing 10^{-3} M $Zn(NO_3)_2$ but not TiO_2 particles. The pH was adjusted at 4 as well in order to have equivalent solution composition. The tests this time though were performed at constant voltage rather than current density in order to investigate different EPD deposition events (refer to variation of cathodic potential in Figure 0-6 (b)). To

ensure accurate control of the potential at the surface of the cathode, a 3-electrode system employing a Ag/AgCl reference electrode and platinum wire as counter electrode was used. The tests were carried out at the following constant cathodic potentials (vs. Ag/AgCl): -1.1, -1.2, and -1.3 *V* corresponding to EPD deposition times (refer to Figure 0-6 (b) and Figure 0-8) 7, 15, and 55 s respectively. XRD characterization of the different zinc deposits (see Figure 0-7 (a)) showed that reduction of zinc ions to zinc metal did occur starting at -1.2 *V* (vs. Ag/AgCl) cathodic potential. No zinc deposit was XRD observable at -1.1 *V* (vs. Ag/AgCl) either before or after annealing probably due to the deposition of amorphous $Zn(OH)_2$ (hydrous zinc oxide) although the latter was supposed to become observable upon conversion to crystalline ZnO after annealing.

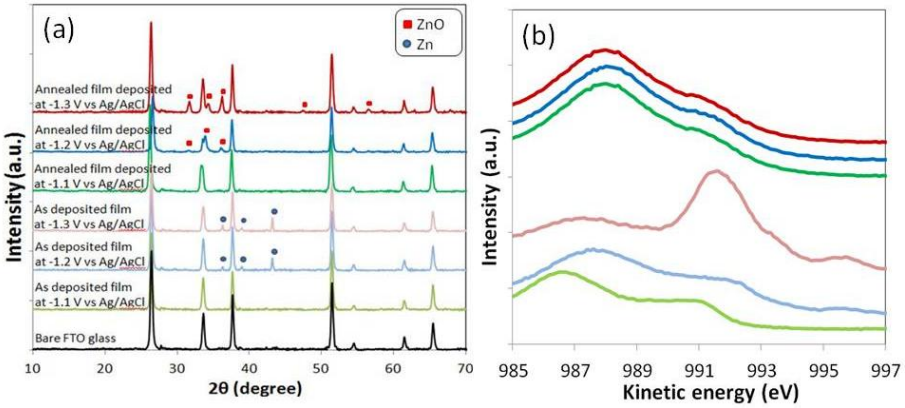

Figure 0-7. (a) XRD patterns and (b) Zn $L_3M_{45}M_{45}$ Auger electron spectra of TiO_2-free zinc films deposited at different constant voltage before and after annealing at 450 ˚C

In order to further elucidate the state of the zinc deposit films, high resolution Zn 2p XPS spectra were collected and compared to those of standards like Zn metal, ZnO and $Zn(OH)_2$ (Table 0-3). However, because of overlap of the Zn $2p_{3/2}$ spectrum of zinc oxide with that of the Zn metal peak BE [42-44], the $L_3M_{45}M_{45}$ Auger electron spectra (AES) were also collected since they are known to show characteristic peaks at 990.9 *eV* and 994.3 *eV* for the zinc metal [45] and at 988.2 *eV* and 991.4 *eV* for ZnO [43]. The relevant Auger spectra are shown in Figure 0-7 (b),

while in Table 0-3 both Zn $2p_{3/2}$ and O 1s, and the main Zn $L_3M_{45}M_{45}$ peak values are summarized and compared to reference data.

Table 0-3: Binding energy of Zn $2p_{3/2}$ and O ls levels and kinetic energy of Zn $L_3M_{45}M_{45}$ Auger peaks of various zinc deposit films compared to Zn, ZnO, and $Zn(OH)_2$ reported by other studies (in *eV*)

	Zn $L_3M_{45}M_{45}$	**Zn $2p_{3/2}$**	**O 1s**	**Ref**
Zn	992.2	1021.65	-	[46]
Zn	991.9	1021.6	-	[47]
ZnO	988.1	1022.1	Not reported	[46]
ZnO	988.2	1022.1	530.5	[48]
ZnO	988.0	1022.06	530.9	This work
$Zn(OH)_2$	987.2	1022.7	532	[48]
$Zn(OH)_2$	986.6	1022.6	Not reported	[46]
As-deposited film at -1.1 V Vs. Ag/ AgCl	986.6	1022.71	532.28	This work
As-deposited film at -1.2 V Vs. Ag/ AgCl	987.8 991.65	1021.67 1022.33	530.99 532.6	This work
As-deposited film at -1.3 V Vs. Ag/ AgCl	991.74	1021.56 1022.74	530.81 532.46	This work
Annealed film deposited at -1.1 V Vs. Ag/ AgCl	988.1	1022.18	530.89	This work
Annealed film deposited at -1.2 V Vs. Ag/ AgCl	988.13	1022.11	530.87	This work
Annealed film deposited at -1.3 V Vs. Ag/ AgCl	988.03	1022.19	530.95	This work

According to the collected data, Zn AES peak, Zn $2p_{3/2}$ and O 1s, the as-deposited film at -1.1 *V* (vs. Ag/AgCl) shows evidence of $Zn(OH)_2$ formation, while after annealing this becomes ZnO confirming the earlier postulation. However, the as-deposited film at -1.2 *V* (vs. Ag/AgCl), after de-convolution of its wide AES peak observed around 987.8 *eV* into two peaks, provides evidence of the presence of both $Zn(OH)_2$ as well as ZnO. Similar deductions are made from the O 1s spectra, where the peaks at 532.68 and 531.09 *eV* correspond to $Zn(OH)_2$ and ZnO, respectively. But in addition, the two small AES peaks that appear at 991.65 and 995.69 *eV* indicate the presence of zinc metal, in agreement with our XRD data. However, after annealing only evidence of ZnO is found suggesting

the air oxidation of zinc metal along the conversion of $Zn(OH)_2$ to ZnO. Finally, the as-deposited film at -1.3 *V* (vs. Ag/AgCl) depicted clear evidence of the presence of zinc metal (AES peaks at 991.74 and 995.7 *eV*); however a small broad AES peak around 987.6 *eV* (along a wide O 1s XPS peak de-convoluted to two peaks at 530.81 and 532.46 *eV*) indicates the presence of $Zn(OH)_2$, and ZnO as well apparently forming from in situ oxidation of the metal. Once more after annealing only the presence of ZnO is observed, resulting apparently by the full oxidation of the metal. These observations are in good agreement with the XRD data.

Thus, it can be concluded that regarding the cathodic potential-time profile during EPD (Figure 0-8), in the first 15 seconds of EPD (at $\Delta\emptyset_{cath,total}$ > -1.2 *V* vs. Ag/AgCl) zinc seems to deposit as hydrous zinc oxide ($Zn(OH)_2/ZnO{\bullet}H_2O$), while at longer times (i.e. at $\Delta\emptyset_{cath,total}$ <-1.2 *V* vs. Ag/AgCl) metallic zinc co-deposits as well. Both forms of zinc deposit, i.e. hydrous zinc oxide and metallic zinc, may be thought to be nanoscale size nuclei forming on the surface of the substrate and the co-deposited TiO_2 particles effectively acting as nanoglue that stabilizes and enforces the adhesion of the film. Especially the deposition of metallic zinc nanoclusters that was not considered before, it seems to have provided additional film strength. Both hydrous zinc oxide and metallic nanodeposits ultimately convert to ZnO upon annealing at 450 ºC. The structure of the TiO_2-ZnO film following annealing is studied next.

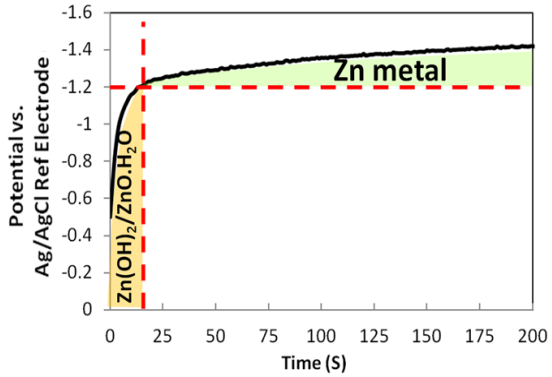

Figure 0-8. Potential at the surface of cathode vs. Ag/AgCl reference electrode during 200 s EPD in a 5 % *v/v* isopropanol-water mixture containing 10^{-3} M $Zn(NO_3)_2$

3.4.4. Probing the TiO_2-ZnO composite film

Film structure: In our pervious study [20], EDS analysis across the cross section of the electrophoretically deposited TiO_2-ZnO film showed relatively uniform deposition of ZnO in the entire film thickness. This was verified in the present study with the data of Table 0-2. High magnification images of the composite film before and after annealing (Figure 0-9) show a well-grown mesoporous structure, highly desirable for photovoltaic application [20]. It was not possible, however to locate any ZnO particles, even when STEM images taken (Figure 0-9 (c)) apparently reflecting their low percentage (~2% Zn) content in the film and/or their likely deposition as thin shell-type coating on the TiO_2 (P25) particles.

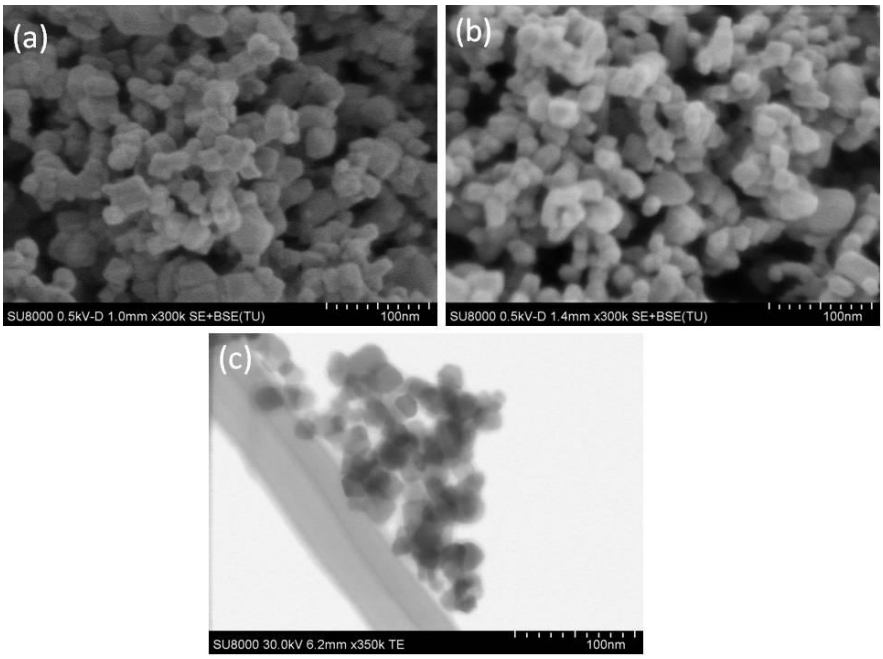

Figure 0-9. Top-view high magnification SEM images of (a) as-deposited and (b) annealed composite TiO_2-ZnO films. (c) STEM image of nanoparticles of annealed TiO_2-ZnO composite film(taken with the SU-8000 Hitachi)

Similarly, XRD patterns (taken at an angle of 2θ from 20 to 60° and shown in Figure 0-10) failed to detect any ZnO characteristic peaks because of the minor

(<3%) presence of the latter in the film as it also happened in other TiO_2-ZnO film investigations [21, 49]. It is noted that the TiO_2 film built here for comparison to composite TiO_2-ZnO film was deposited by EPD in the 5 % v/v isopropanol–water mixture without any $Zn(NO_3)_2$ being present. The XRD results showed only the presence of TiO_2 (anatase and rutile) and FTO glass. The mixed phase TiO_2 content is not surprising as P25 is known to consist of ~80% anatase and 20% rutile [50]. Furthermore, there were no signs of Zn^{2+} ion substitution into the TiO_2 lattice as otherwise the XRD peaks for TiO_2 would have shifted to some extent [51-52]. Finally, Raman spectra of both films with and without co-deposited zinc oxide did not detect ZnO but surface-sensitive XPS analysis, as described in the next section, did confirm its presence suggesting, ZnO crystallites to have deposited on the surface of TiO_2 nanoparticles [49].

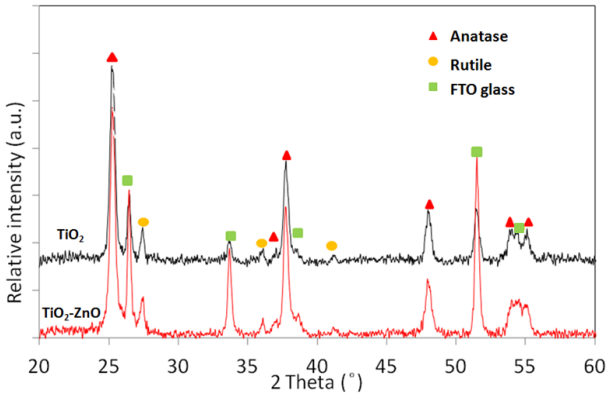

Figure 0-10. XRD patterns of TiO_2 and TiO_2-ZnO films after annealing

Electronic properties: In order to investigate the electronic effects from the co-deposition of ZnO in the TiO_2 film, XPS analysis was carried out for both TiO_2 and TiO_2-ZnO composite films. The Ti 2p XPS high-resolution spectra for both films (Figure 0-11 (a)) exhibited two peaks at 459.25 *eV* and 464.95 *eV* for the TiO_2 film (459.42 *eV* and 465.1 *eV* for TiO_2-ZnO film) attributed to Ti $2p_{3/2}$ and Ti $2p_{1/2}$ states, which are characteristic of titanium (IV) species such as anatase [53-54]. More importantly we can clearly observe that the Ti 2p bands of the TiO_2-ZnO

film are shifted by +0.17 *eV* for Ti $2p_{3/2}$ and +0.15 *eV* for Ti $2p_{1/2}$ compared to those in the TiO_2 film. These types of shifts are important, as they are the manifestation of a change in the Fermi level position of the band gap or a change of the surface dipole [53-56]. In our case the coupling of the ZnO with the TiO_2 likely caused a shift in the Fermi energy, which is expressed in the XPS spectra as a shift to higher energy for the core states ($2p_{1/2}$, $2p_{3/2}$) of TiO_2. Kang et al. [57] observed a similar shift to higher binding energy side (~0.3 *eV*) for the Ti 2p core level XPS data of their TiO_2 sample coated with ZnO, which was attributed to the different electron affinity that ZnO exhibits. In addition, Dobler et al. [56] mentioned that the shift of binding energy to the higher value is connected to the upward movement of Fermi level. It is interesting to note that, in our previous study [20] within which the TiO_2-ZnO thin film was employed as photoelectrode for dye-sensitized solar cell application, it was resulted in higher open circuit voltage (V_{OC}) compared to the TiO_2 photoelectrode. The higher V_{oc} relates to a higher Fermi level of TiO_2-ZnO film compared to TiO_2 film, which is in a good agreement with the present XPS data.

The Zn 2p spectrum (Figure 0-11 (b)) exhibited the spin-orbit splitting attributed to p states with the Zn $2p_{3/2}$ and Zn $2p_{1/2}$ occurring at 1021.93 *eV* and 1045 *eV* respectively in agreement with [46] and those of pure ZnO powder (collected for comparison) occurring at 1022.06 *eV* and 1045.14 *eV*. Therefore, it can be confirmed that the zinc present in our annealed film is in the form of ZnO. Furthermore, we did not observe any other Zn 2p peak other than those attributed to the Zn-O type of bonding.

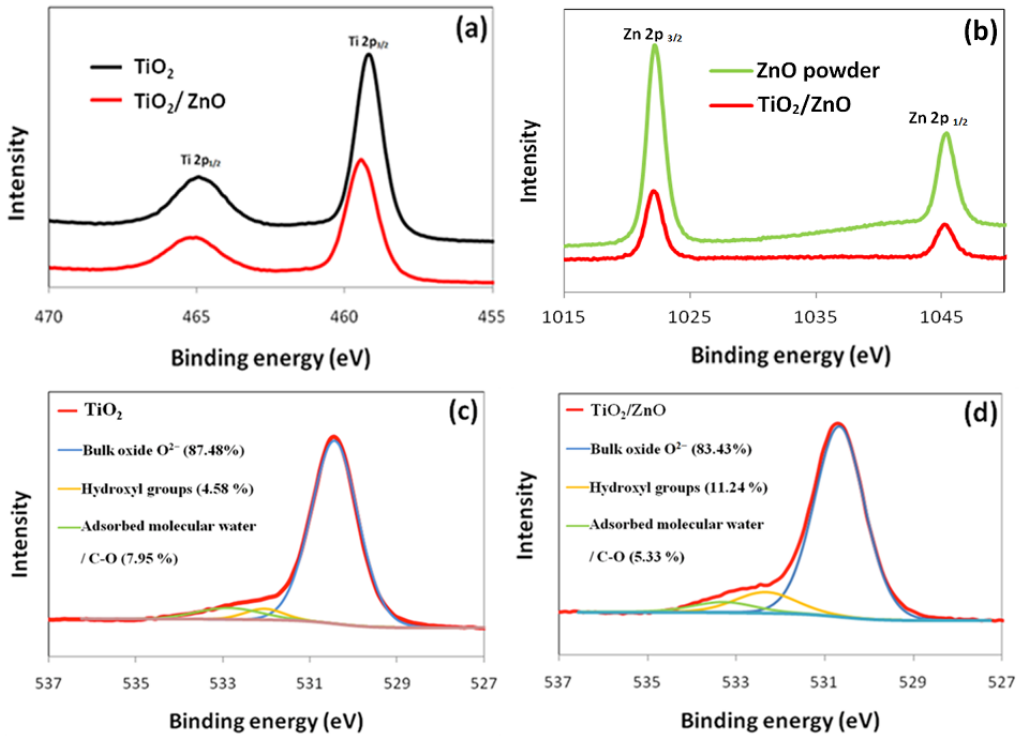

Figure 0-11. High resolution XPS spectra of (a) Ti 2p region, (b) Zn 2p region, and (c and d) O 1s region for TiO_2 and TiO_2-ZnO films after annealing

The O 1s XPS spectra for both films are shown in Figure 0-11(c) and (d). According to some reports the O 1s peak of TiO_2 may be separated in two peaks at 530.64 and 531.8 *eV* corresponding to bulk oxide (O^{2-}) and hydroxyl (OH^-) groups, respectively [50, 58]. On the other hand, some other studies on the pure TiO_2 system [54, 59] and also the combined TiO_2-ZnO system [21, 51] de-convoluted the O 1s XPS spectrum of TiO_2 to at least three resolved peaks at 529.9, 531.5, and 532.8 *eV*, which were assigned to the oxygen in the TiO_2 bulk, oxygen in surface hydroxyl groups, and adsorbed molecular water and/or to the oxygen present due to organic contamination, respectively. We also fitted our O 1s spectra via three peaks. Thus, the bulk oxygen was observed at 530.44 *eV* for TiO_2 film (530.68 *eV* for TiO_2-ZnO film), the surface Ti−OH groups at 532.05 *eV* for TiO_2 film (532.34 *eV* for TiO_2-ZnO film), and adsorbed water and/or organic contaminants at 532.87 *eV* for TiO_2 film (533.29 *eV* for TiO_2-ZnO film). It can be seen that the O 1s

entire spectrum of the TiO_2-ZnO film is shifted to higher energy in comparison to the TiO_2 film. This being so because the O 1s band position is at higher binding energy in ZnO compared with that in TiO_2, as also reported in [60]. Moreover, it should be noted that the full width at half maximum (FWHM) of O 1s peak at 530.68 *eV* for the TiO_2-ZnO film was found to be slightly increased (1.27 to 1.33 *eV*) due to the overlapping of the O–Zn and O–Ti in agreement with [21]. This behavior also implies that the coupled Zn^{2+} ions exist as ZnO on TiO_2 surface.

The relative occurrence of each oxygen species was calculated as proportional to their characteristic peak area and listed in the inset of Figure 0-11(c) and (d). It is clear that the relative abundance of hydroxyl groups is higher in the TiO_2-ZnO film than in the TiO_2 film. In several studies [21, 49, 51], the abundance of hydroxyl group was found to increase significantly with increasing ZnO dosage to TiO_2.

Optical properties: UV–vis spectroscopy has been widely used to investigate the optical properties of semiconductors specifically their band gap (E_g). The absorption curves of the electrophoretically grown TiO_2 and TiO_2-ZnO thin films are shown in Figure 0-12. According to these spectra the TiO_2-ZnO composite film is more transparent compared to the TiO_2 film. Similar blue-shifting effect after modification of TiO_2 with ZnO was observed by Li et al. [61]. They attributed the absorption band edge change to occupation of surface states of TiO_2 by ZnO, as already suggested earlier from our characterization work. To estimate the effect of ZnO on TiO_2 bandgap we plotted (see inset in Figure 0-12) $(\alpha h\nu)^{1/2}$ vs. $(h\nu)$, where α is the absorption coefficient and $h\nu$ the photon energy. By extrapolation of the decreasing slope to zero the E_g value was obtained [62]. The absorption coefficient was calculated using the Kubelka–Munk function [63] from the measured diffusive reflectance by using the equation 0-10:

$$\alpha = (1-R)^2/2R \qquad (0\text{-}10)$$

The band gap energy of the TiO_2-ZnO film (3.26 *eV*) was slightly higher compared to that of the TiO_2 film (3.14 *eV*), which corresponds to the wider direct band gap of ZnO (3.37 *eV*) [64].

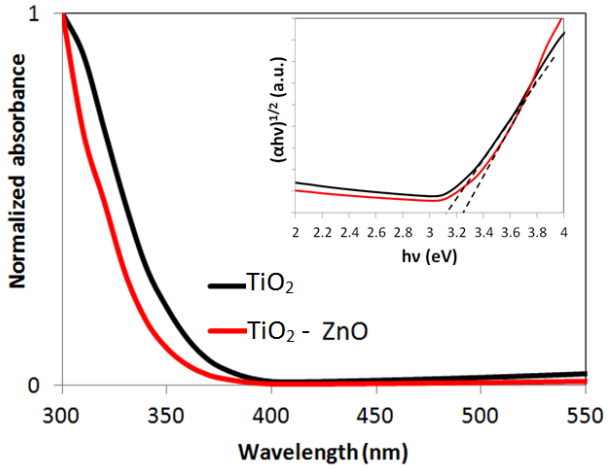

Figure 0-12. Normalized UV–vis absorption coefficient spectra of annealed TiO_2 and TiO_2-ZnO films obtained from diffuse reflectance measurements. The inset shows the plot of $(\alpha h\nu)^{1/2}$ vs. photon energy $h\nu$

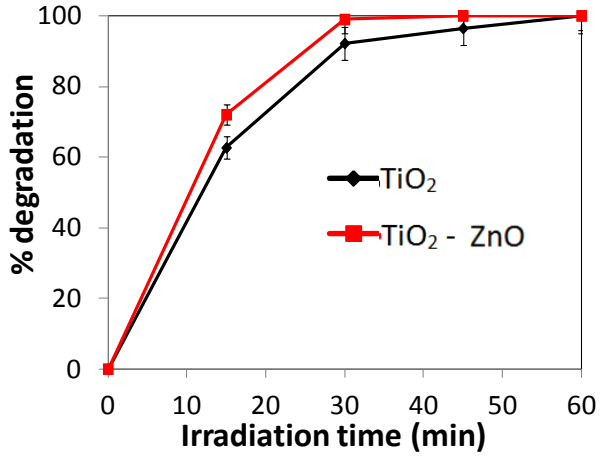

Figure 0-13. Percent of degradation of methyl orange by TiO_2 and TiO_2-ZnO powder, scratched off their annealed films, under UV light irradiation

Photocatalytic activity: The results of methyl orange degradation experiments (shown in Figure 0-13) indicate that the TiO_2-ZnO film is more photoactive than the TiO_2 film. As alluded earlier this can be attributed to the

higher hydroxyl content endowed to the TiO_2 film by the co-deposition of ZnO. As per previous studies [65] TiO_2 surfaces covered with abundant hydroxyl groups (that result from coupling with metal oxides as is ZnO in this study) are more capable to accept the light-induced holes and hence to oxidize adsorbed organic molecules, i.e methyl orange [58].

3.5. Conclusion

Highly adherent and robust mesoporous TiO_2-ZnO films were successfully deposited by EPD by employing a cost-effective and environmentally friendly aqueous suspension system. In this regard, parameters related to the suspension formulation have been systematically studied and optimized. Adding isopropanol to the water as co-solvent decreased the surface tension and conductivity, which are desirable in EPD. On the other hand, it decreased the zeta potential, electrophoretic mobility and the adhesion of the deposited film to the substrate, when added in large excess. Thus, 5 % *v/v* isopropanol-water mixture was chosen as the optimum solvent. A critical component that ultimately allowed the growth of robust films was the use of $Zn(NO_3)_2$ as additive. After varying its concentration, 10^{-3} M was found to be the optimum level for a 5 $g.L^{-1}$ P25 TiO_2 nanoparticle suspension. Finally, selection of low DC voltage at constant 0.1 $mA.cm^{-2}$ current density was found to minimize hydrogen evolution at the cathode hence favoring the growth of an adherent film. The latter appeared to be further assisted by the co-deposition of metallic nanozinc (along $Zn(OH)_2$) that suppresses the hydrogen evolution reaction via the increase of its activation overpotential.

Zinc co-deposition was shown to occur in the early EPD stages via the formation of $Zn(OH)_2$ involving localized cathodic generation of hydroxyl groups by reduction of nitrate to nitrite ions. However, via cathodic potential monitoring and analysis of zinc deposits at different times, it has been for the first time revealed that metallic nanozinc deposits as well with the progress of film growth.

The latter, owing to the open-air aqueous environment appears to oxidize partly *in situ* and be distributed uniformly (~2% Zn) within the whole film. As such this hydrous zinc oxide nanodeposit acts as nanoglue, yielding after annealing very robust and well adhered TiO_2 –ZnO composite films. XPS analysis of the latter suggests ZnO to have deposited on the surface of TiO_2 rendering the latter enriched in hydroxyl groups, which are known to enhance its photocatalytic activity as confirmed via methyl orange degradation experiments under UV irradiation.

3.6. Acknowledgments

This research is supported via a NSERC strategic project grant and sponsored by CIS Solar, Hydro-Quebec, Versatilis Inc and Targray Technology International. Professor N. Tufenkji and Ranjan Roy are thanked for permission to use the Zetasizer and UV lamp in their laboratories.

3.7. References

1. Kwon S, Fan M, Cooper AT, Yang H. Photocatalytic applications of micro- and nano-TiO_2 in environmental engineering. Critical Reviews in Environmental Science and Technology 2008;38(3):197-226.

2. Hashimoto K, Irie H, Fujishima A. TiO_2 photocatalysis: A historical overview and future prospects. Japanese Journal of Applied Physics, Part 1: Regular Papers and Short Notes and Review Papers 2005;44(12):8269-85.

3. Jung H-G, Yoon CS, Prakash J, Sun Y-K. Mesoporous Anatase TiO_2 with High Surface Area and Controllable Pore Size by F^--Ion Doping: Applications for High-Power Li-Ion Battery Anode. The Journal of Physical Chemistry C 2009;113(50):21258-63.

4. Zou Z, Ye J, Sayama K, Arakawa H. Direct splitting of water under visible light irradiation with an oxide semiconductor photocatalyst. Nature 2001;414(6864):625-27.

5. O'Regan B, Grätzel M. A low-cost, high-efficiency solar cell based on dye-sensitized colloidal TiO_2 films. Nature 1991;353:737 - 40.

6. Hagfeldt A, Boschloo G, Sun L, Kloo L, Pettersson H. Dye-Sensitized Solar Cells. Chemical Reviews 2010;110(11):6595-663.

7. Ito S, Chen P, Comte P, Nazeeruddin MK, Liska P, Péchy P, et al. Fabrication of screen-printing pastes from TiO_2 powders for dye-sensitised solar cells. Progress in Photovoltaics: Research and Applications 2007;15(7):603-12.

8. Dor S, Rühle S, Ofir A, Adler M, Grinis L, Zaban A. The influence of suspension composition and deposition mode on the electrophoretic deposition of TiO_2 nanoparticle agglomerates. Colloids and Surfaces A: Physicochemical and Engineering Aspects 2009;342(1-3):70-75.

9. Grinis L, Kotlyar S, Rühle S, Grinblat J, Zaban A. Conformal Nano-Sized Inorganic Coatings on Mesoporous TiO_2 Films for Low-Temperature Dye-Sensitized Solar Cell Fabrication. Advanced Functional Materials 2010;20(2):282-88.

10. Yamaguchi T, Tobe N, Matsumoto D, Nagai T, Arakawa H. Highly efficient plastic-substrate dye-sensitized solar cells with validated conversion efficiency of 7.6%. Solar Energy Materials and Solar Cells 2010;94(5):812-16.

11. Liou Y-J, Hsiao P-T, Chen L-C, Chu Y-Y, Teng H. Structure and Electron-Conducting Ability of TiO_2 Films from Electrophoretic Deposition and

Paste-Coating for Dye-Sensitized Solar Cells. The Journal of Physical Chemistry C 2011;115(51):25580-89.

12. Lebrette S, Pagnoux C, Abélard P. Fabrication of titania dense layers by electrophoretic deposition in aqueous media. Journal of the European Ceramic Society 2006;26(13):2727-34.

13. Hayward RC, Saville DA, Aksay IA. Electrophoretic assembly of colloidal crystals with optically tunable micropatterns. Nature 2000;404(6773):56-59.

14. Besra L, Uchikoshi T, Suzuki TS, Sakka Y. Application of constant current pulse to suppress bubble incorporation and control deposit morphology during aqueous electrophoretic deposition (EPD). Journal of the European Ceramic Society 2009;29(10):1837-45.

15. Besra L, Uchikoshi T, Suzuki TS, Sakka Y. Bubble-Free Aqueous Electrophoretic Deposition (EPD) by Pulse-Potential Application. Journal of the American Ceramic Society 2008;91(10):3154-59.

16. Neirinck B, Fransaer J, Biest OVd, Vleugels J. Aqueous electrophoretic deposition in asymmetric AC electric fields (AC–EPD). Electrochemistry Communications 2009;11(1):57-60.

17. Russ BE, Talbot JB. An Analysis of the Binder Formation in Electrophoretic Deposition. Journal of The Electrochemical Society 1998;145(4):1253-56.

18. Russ BE, Talbot JB. A Study of the Adhesion of Electrophoretically Deposited Phosphors. Journal of The Electrochemical Society 1998;145(4):1245-52.

19. Siracuse JA, Talbot JB, Sluzky E, Hesse KR. The Adhesive Agent in Cataphoretically Coated Phosphor Screens. Journal of The Electrochemical Society 1990;137(1):346-48.

20. Parsi Benehkohal N, Demopoulos GP. Green Preparation of TiO_2-ZnO Nanocomposite Photoanodes by Aqueous Electrophoretic Deposition. Journal of The Electrochemical Society 2012;159(5):B602-B10.

21. Ku Y, Huang Y-H, Chou Y-C. Preparation and characterization of ZnO/ TiO_2 for the photocatalytic reduction of Cr(VI) in aqueous solution. Journal of Molecular Catalysis A: Chemical 2011;342-343:18-22.

22. Kim DW, Lee S, Suk Jung H, Young Kim J, Shin H, Hong KS. Effects of heterojunction on photoelectrocatalytic properties of ZnO- TiO_2 films. International Journal of Hydrogen Energy 2007;32(15):3137-40.

23. Marcì G, Augugliaro V, López-Muñoz MJ, Martín C, Palmisano L, Rives V, et al. Preparation Characterization and Photocatalytic Activity of Polycrystalline ZnO/ TiO_2 Systems. 1. Surface and Bulk Characterization. The Journal of Physical Chemistry B 2001;105(5):1026-32.

24. Lee K, Charbonneau C, Shan G, Demopoulos G, Gauvin R. Nanocrystalline TiO_2 thin film electrodes for dye-sensitized solar cell applications. JOM Journal of the Minerals, Metals and Materials Society 2009;61(4):52-57.

25. Choudhury B, Borah B, Choudhury A. Extending Photocatalytic Activity of TiO_2 Nanoparticles to Visible Region of Illumination by Doping of Cerium. Photochemistry and Photobiology 2012;88(2):257-64.

26. Besra L, Liu M. A review on fundamentals and applications of electrophoretic deposition (EPD). Progress in Materials Science 2007;52(1):1-61.

27. Moldoveanu GA, Demopoulos GP. Producing high-grade nickel sulfate with solvent displacement crystallization. JOM 2002;54(1):49-53.

28. Peng Z, Liu M. Preparation of Dense Platinum-Yttria Stabilized Zirconia and Yttria Stabilized Zirconia Films on Porous $La_{0.9}Sr_{0.1}MnO_3$ (LSM) Substrates. Journal of the American Ceramic Society 2001;84(2):283-88.

29. Lebrette S, Pagnoux C, Abélard P. Stability of aqueous TiO_2 suspensions: influence of ethanol. Journal of Colloid and Interface Science 2004;280(2):400-08.

30. Akerlof G. Dielectric constant of some organic solvent-water mixturs at various temperaturs. Journal of the American Chemical Society: American Chemical Society; 1932. p. 4125-39.

31. Tang F, Uchikoshi T, Ozawa K, Sakka Y. Effect of polyethylenimine on the dispersion and electrophoretic deposition of nano-sized titania aqueous suspensions. Journal of the European Ceramic Society 2006;26(9):1555-60.

32. Radice S, Bradbury CR, Michler J, Mischler S. Critical particle concentration in electrophoretic deposition. Journal of the European Ceramic Society 2010;30(5):1079-88.

33. Dzombak DA, Morel F. Surface Complexation Modeling: Hydrous Ferric Oxide: Wiley; 1990.

34. Van der Biest OO, Vandeperre LJ. Electrophoretic deposition of materials. Annual Review of Materials Science 1999;29(1):327-52.

35. Shane MJ, Talbot JB, Kinney BG, Sluzky E, Hesse KR. Electrophoretic Deposition of Phosphors: II. Deposition Experiments and Analysis. Journal of Colloid and Interface Science 1994;165(2):334-40.

36. Ma J, Cheng W. Deposition and packing study of sub-micron PZT ceramics using electrophoretic deposition. Materials Letters 2002;56(5):721-27.

37. Hamaker HC. Formation of a deposit by electrophoresis. Transactions of the Faraday Society 1940;35:279-87.

38. Karuppuchamy S, Nonomura K, Yoshida T, Sugiura T, Minoura H. Cathodic electrodeposition of oxide semiconductor thin films and their application to dye-sensitized solar cells. Solid State Ionics 2002;151(1-4):19-27.

39. Chang WL, Sathiyanarayanan K, Seung WE, Mun SY. Studies on Suppression of Hydrogen Evolution Reaction for Zinc/Air Fuel Cell; Materials Science Forum, 2007; 539-543:1427-30.

40. Yoshida T, Komatsu D, Shimokawa N, Minoura H. Mechanism of cathodic electrodeposition of zinc oxide thin films from aqueous zinc nitrate baths. Thin Solid Films 2004;451-452:166-69.

41. Zhang L, Chen Z, Tang Y, Jia Z. Low temperature cathodic electrodeposition of nanocrystalline zinc oxide thin films. Thin Solid Films 2005;492(1–2):24-29.

42. Biesinger MC, Lau LWM, Gerson AR, Smart RSC. Resolving surface chemical states in XPS analysis of first row transition metals, oxides and hydroxides: Sc, Ti, V, Cu and Zn. Applied Surface Science 2010;257(3):887-98.

43. Schön G. Auger and direct electron spectra in X-ray photoelectron studies of zinc, zinc oxide, gallium and gallium oxide. Journal of Electron Spectroscopy and Related Phenomena 1973;2(1):75-86.

44. Hashimoto S, Abe M. The characterization of electrodeposited Zn-SiO_2 composites before and after corrosion test. Corrosion Science 1994;36(12):2125-37.

45. Yin L, Tsang T, Adler I, Yellin E. L-S coupling interpretation of high solution LMM Auger spectra of Cu and Zn. Journal of applied physics 1972;43(8):3464-67.

46. Dake LS, Baer DR, Zachara JM. Auger parameter measurements of zinc compounds relevant to zinc transport in the environment. Surface and Interface Analysis 1989;14(1-2):71-75.

47. Kowalczyk SP, Pollak RA, McFeely FR, Ley L, Shirley DA. $L_{2,3}M_{45}M_{45}$ Auger Spectra of Metallic Copper and Zinc: Theory and Experiment. Physical Review B 1973;8(6):2387-91.

48. Deroubaix G, Marcus P. X-ray photoelectron spectroscopy analysis of copper and zinc oxides and sulphides. Surface and Interface Analysis 1992;18(1):39-46.

49. Zou J-J, Zhu B, Wang L, Zhang X, Mi Z. Zn- and La-modified TiO_2 photocatalysts for the isomerization of norbornadiene to quadricyclane. Journal of Molecular Catalysis A: Chemical 2008;286(1-2):63-69.

50. Erdem B, Hunsicker RA, Simmons GW, Sudol ED, Dimonie VL, El-Aasser MS. XPS and FTIR Surface Characterization of TiO_2 Particles Used in Polymer Encapsulation. Langmuir 2001;17(9):2664-69.

51. Wang H, Wu Z, Liu Y, Sheng Z. The characterization of ZnO–anatase–rutile three-component semiconductor and enhanced photocatalytic activity of nitrogen oxides. Journal of Molecular Catalysis A: Chemical 2008;287(1-2):176-81.

52. Wang Z-S, Huang C-H, Huang Y-Y, Hou Y-J, Xie P-H, Zhang B-W, et al. A Highly Efficient Solar Cell Made from a Dye-Modified ZnO-Covered TiO_2 Nanoporous Electrode. Chemistry of Materials 2001;13(2):678-82.

53. Shirkhanzadeh M. XRD and XPS characterization of superplastic TiO_2 coatings prepared on Ti_6Al_4V surgical alloy by an electrochemical method. Journal of Materials Science: Materials in Medicine 1995;6(4):206-10.

54. Lee KE, Gomez MA, Regier T, Hu Y, Demopoulos GP. Further Understanding of the Electronic Interactions between N719 Sensitizer and Anatase TiO_2 Films: A Combined X-ray Absorption and X-ray Photoelectron Spectroscopic Study. The Journal of Physical Chemistry C 2011;115(13):5692-707.

55. Onda K, Li B, Petek H. Two-photon photoemission spectroscopy of TiO_2 (110) surfaces modified by defects and O_2 or H_2O adsorbates. Physical Review B 2004;70(4):045415.

56. Dobler DD, Oswald SO, Wetzig KW. Calibration of XPS - energy scale for determination of the oxidation states of doping elements in SnO_2 powders. Analytical and Bioanalytical Chemistry 2002;374(4):646-49.

57. Kang SH, Kim J-Y, Kim Y, Kim HS, Sung Y-E. Surface Modification of Stretched TiO_2 Nanotubes for Solid-State Dye-Sensitized Solar Cells. The Journal of Physical Chemistry C 2007;111(26):9614-23.

58. Liao S, Donggen H, Yu D, Su Y, Yuan G. Preparation and characterization of ZnO/ TiO_2, SO_4^{2-}/ZnO/ TiO_2 photocatalyst and their photocatalysis. Journal of Photochemistry and Photobiology A: Chemistry 2004;168(1-2):7-13.

59. Simmons GW, Beard BC. Characterization of acid-base properties of the hydrated oxides on iron and titanium metal surfaces. The Journal of Physical Chemistry 1987;91(5):1143-48.

60. Kim S-S, Yum J-H, Sung Y-E. Flexible dye-sensitized solar cells using ZnO coated TiO_2 nanoparticles. Journal of Photochemistry and Photobiology A: Chemistry 2005;171(3):269-73.

61. Li S-j, Lin Y, Tan W-w, Zhang J-b, Zhou X-w, Chen J-m, et al. Preparation and performance of dye-sensitized solar cells based on ZnO-modified TiO_2 electrodes. International Journal of Minerals, Metallurgy, and Materials 2010;17(1):92-97.

62. Charbonneau C, Lee KE, Shan GB, Gomez MA, Gauvin R, Demopoulos GP. Preparation and DSSC Performance of Mesoporous Film Photoanodes Based on Aqueous-Synthesized Anatase Nanocrystallites. Electrochemical and Solid-State Letters 2010;13(8):H257-H60.

63. A.B, Murphy. Band-gap determination from diffuse reflectance measurements of semiconductor films, and application to photoelectrochemical water-splitting. Solar Energy Materials and Solar Cells 2007;91(14):1326-37.

64. Wang ZL. ZnO nanowire and nanobelt platform for nanotechnology. Materials Science and Engineering: R: Reports 2009;64(3-4):33-71.

65. Papp J, Soled S, Dwight K, Wold A. Surface Acidity and Photocatalytic Activity of TiO_2, WO_3/ TiO_2, and MoO_3/ TiO_2 Photocatalysts. Chemistry of Materials 1994;6(4):496-500.

Chapter 4. Green Preparation of TiO_2-ZnO Nanocomposite Photoanodes by Aqueous Electrophoretic Deposition

In continuation of the work described in Chapter 3, here, TiO_2-ZnO nanocomposite films are prepared by aqueous electrophoretic deposition and employed as photoanodes in the fabrication of dye-sensitized solar cells. The rational of co-depositing ZnO with the TiO_2 nanoparticles is explained not only on the basis of film adhesion but also in terms of ZnO's favorable semiconductor properties, namely high electron mobility (155 $cm^2\ V^{-1}\ s^{-1}$) and wide band gap (3.37 *eV*). The deposited composite films are optimized in terms of structure and thickness, assembled into DSSC devices and comprehensively characterized by a variety of photoelectrochemical techniques, including electrochemical impedance spectroscopy. The publication info for this Chapter are: N. Parsi Benehkohal, G.P. Demopoulos, *Journal of the Electrochemical Society 159 (2012) B602.*

4.1. Abstract

Aqueous-based electrophoretic deposition (EPD) of titania nanoparticles (Evonic's P25) was successfully applied to the fabrication of mesoporous electrodes for dye-sensitized solar cells (DSSC). Poor film adhesion and cracking arising from the electrolysis of water and interstitial water evaporation during drying were largely overcome via the selection of low EPD operating current density/DC voltage (0.1 $mA.cm^{-2}$/2.5-3.1 V) but more importantly the addition of zinc nitrate in a 5 vol.% isopropanol-water suspension. As a result, a composite nanostructured TiO_2-ZnO film was fabricated. Photoelectrochemical characterization indicates that in-situ formation of ZnO causes suppression of charge recombination at the electrode/electrolyte interface thus prolonging photoelectron lifetime. A 5.01% conversion efficiency was obtained under 1 sun illumination (100 $mW.cm^{-2}$) of a 13 μm thick single transparent film. The efficiency was further improved to 6.19% upon further optimization via multi-layer construction of the transparent anatase film (18 μm thick) by repeated cycles of EPD.

4.2. Introduction

The dye-sensitized solar cell (DSSC) is attracting tremendous interest as a third-generation renewable energy conversion device [1-4]. The mesoporous nanocrystaline titania thin film is in the heart of the DSSC. Among various fabrication methods, electrophoretic deposition (EPD) may provide process simplification, cost reduction and high throughput manufacturing capability [5]. Thus a number of recent reports have successfully demonstrated the fabrication of DSSC photoanodes by EPD on glass [5], Ti foil [6] or conductive plastic materials [7]. However in all these EPD methods organic solvents and toxic additives were used which are not compatible with the principles of green chemistry. Use of water as solvent is preferred but this has been hampered by the use of high DC voltages that cause its decomposition and gas evolution preventing the growth of good

quality mesoporous films. As a result very few research studies have sought to prepare mesoporous titania electrodes for DSSCs purposes by employing EPD in aqueous media [8-11].

Some of the measures taken in the past to overcome the problem due to water electrolysis in aqueous-based EPD involved lowering the applied current or adding ethanol to the suspension. The former results in general to long deposition time. With the addition of 10 vol.% ethanol, oxygen evolution at the anode appears to be prevented since the oxidation of ethanol occurs at a potential lower than that of water [9]. Thus, Zhao et al. [10] fabricated 2 μm thick films made by EPD (in 30% *v/v* ethanol/water mixture) of ordered titanate nanotubes or commercial P25 TiO_2 powder, and obtained respectively 3.79 and 2.89% efficiencies after annealing at 600° C. Kim et al. [11], on the other hand, prepared 10 μm thick films by EPD (in 30% *v/v* methanol/water mixture) of titanate nanotubes on FTO, which upon annealing at 450 and 500 ◦C showed efficiency of 4.25 and 6.71% respectively. To our knowledge, this is one of the highest conversion efficiency reported so far for photoanodes fabricated by aqueous EPD. However, it is worthy to note that the use of titanate nanotubes greatly increases the complexity and cost of the process making it less attractive from a commercialization perspective.

In this study, the limitations of aqueous-based EPD are successfully overcome by deploying a water-isopropanol (5 vol.%) suspension containing a small amount of $Zn(NO_3)_2$ serving both as charging additive and as binder upon localized hydroxide deposition. Previously salts such as $Mg(NO_3)_2$, $MgCl_2$, or $AlCl_3$ have been used [12]. Thus for example, EPD of phosphor particles in predominantly isopropanol (containing only a minor fraction of water) suspension was reported to benefit from the presence of $Mg(NO_3)_2$ that acts as binder via the formation of $Mg(OH)_2$ [13-15]. Here we have opted to use zinc nitrate instead with the objective of building TiO_2-ZnO composite photoanode. ZnO is an interesting semiconductor material to use in this context because of its favourable properties in comparison to TiO_2 [16-17], such as high electron mobility (155 $cm^2.V^{-1}.s^{-1}$) and wide band gap (3.37 eV) [18]. Several researchers [19-21] have exploited ZnO (as

blocking layer) to reduce the recombination at the interface of TiO_2/electrolyte due to its more negative conduction band edge than TiO_2 (about 100 *mV*) [22] or at the FTO/TiO_2 interface [23]. The latter interface was reported to be associated with more extensive current loss due to recombination, than the current loss taking place across the depth of the film itself [24].

4.3. Experimental

4.3.1. Aqueous EPD suspension and procedure

As a starting point the aqueous suspension-based EPD procedure previously reported by Manríquez and Godínez [25] was studied. Constant current density DC EPD was performed at 0.1 $mA.cm^{-2}$. At this current density a rather low voltage was applied (~2.5-3.1 *V*) thus minimizing water decomposition. The voltage was applied between a stainless steel sheet (anode) and a fluorine-doped tin-oxide conducting glass substrate (FTO-Glass, 10 $\Omega.cm^{-2}$, Nippon Sheet Glass, Japan). The suspension consisted of 1 g P25 TiO_2 powder (AEROXIDE® TiO_2 P25, Evonic) in 200 *mL* 5% *v/v* isopropanol-deionized water mixture. Various amounts of $Zn(NO_3)_2$ were added into the suspension as charging agent as well as binder. The suspension was sonicated for 1.5 h prior to EPD. The distance between the two electrodes was 2 *cm*. The deposition area of the photoelectrode was about 5 cm^2. A Keithley 2400 SourceMeter was used as power supply. Deposition time was in the range of 5-15 min. Fresh layers at different deposition times were taken out from the electrophoretic cell, dried at room temperature and subjected to post-treatment and characterization.

4.3.2. Suspension characterization

The surface tension of the suspension was measured with a Krauss K-12 Tensiometer using the Wilhelmy Plate method. The zeta potential and agglomerate size distribution of the colloidal suspension was measured with a Malvern Zetasizer Nano ZS (Malvern Instruments Ltd., UK). The colloidal

stability of TiO_2 aqueous suspension was evaluated from the change of the suspension optical absorbance using UV/vis spectrophotometry (Lambda20, PerkinElmer)[26-27]. Different suspensions containing a range of 10^{-4}-10^{-2} M $Zn(NO_3)_2$ were prepared and poured into a cuvette. The dependence of absorbance on time was measured at λ = 420 nm and corrected for the blank solution of 5% *v/v* isopropanol-DI water mixture.

4.3.3. Mesoporous film characterization

The freshly deposited films were annealed at 450 °C in air for 30 min followed by $TiCl_4$ post-treatment and annealed again [28]. The resultant porous TiO_2 films with and without the $Zn(NO_3)_2$ as binder were designated as binder-porous film ("BP film") and porous film ("P film"), and the corresponding electrodes were BP and P electrode, respectively. After cooling to room temperature, the TiO_2 films were sensitized by immersing into a 0.5 mM solution of N719 in ethanol at room temperature for 48 *h*. The TiO_2 film was rinsed with ethanol to remove physisorbed dye molecules. The thickness of transparent TiO_2 film (no scattering layer used [29]) was measured using the Dektak 3030 surface profiler system (Veeco Instruments Inc., U.S.A.). The surface area and film porosity data were obtained with Brunauer Emmett–Teller (BET) surface area analysis performed on a Micromeritics TriStar 3000 nitrogen adsorption–desorption apparatus. A multiple point specific surface area type of analysis was carried out. Each sample weighed approximately 100 mg and had been degassed for 4 h at 80°C prior to nitrogen physisorption. The morphology of the TiO_2 films was investigated using a field emission scanning electron microscope FE-SEM (S-4700 Hitachi). Energy-dispersive X-ray spectroscopy (Oxford, S-4700 Hitachi) was employed to determine the chemical species of the composite substrates. AFM (NT-MDT, Solver scanning probe microscope) measurements were performed under an ambient atmosphere using the semi contact mode. Conductive silicon cantilevers (MikroMasch) with a typical resonance frequency of 289 kHz

and force constant of 11.5 $N.m^{-1}$ were used. The average roughness was measured for 80 μm scan size and ca. 205 $\mu m.s^{-1}$ scan velocity.

4.3.4. Solar cell assembly

In order to assemble DSSC, the Pt-counter electrode was prepared by dripping a drop of 5 *mM* $HPtCl_6$-propanol solution onto the pre-cleaned FTO-glass and then heat it at 380 °C for 30 min. The working and counter electrodes were assembled into a sandwich-type cell and sealed with a thermoplastic sealant of 30 μm thickness (Surlyn®-30, Dyesol) by hot-pressing, followed by insertion of commercial electrolyte solution (EL-HPE, Dyesol) through a hole on the Pt electrode.

4.3.5. Photoelectrochemical measurements

J-V curves were recorded using a small area solar simulator (PV measurements Inc., Model SASS) under illumination of uniform light approximating 100 $mW.cm^{-2}$ (AM 1.5 solar emission) provided by a tungsten lamp. Replicate tests of *J-V* measurements were performed for better accuracy. The incident light intensity was calibrated using a Si reference cell. The electrochemical impedance spectra (EIS) were measured by using a VSP-potentiostat system (BioLogic) under 100 $mW.cm^{-2}$ illumination, applying a 10 *mV* AC signal and scanning in a frequency range between 400 *kHz* and 1 *Hz* at different forward applied bias. The EIS data were analyzed with the Z-view software. Open-circuit voltage decay (OCVD) analysis [7, 30-31] was also used to provide detailed curves of electron lifetime (τ) versus open circuit voltage (V_{OC}). In this method, steady-state illumination at open circuit was switched off by a shutter and the V_{OC} recorded as a function of time.

4.4. Results and Discussion

4.4.1. Suspension characterization

The pH of the solvent (prior to particle addition) was 5.6; this decreased to 4 after adding 5 $g.L^{-1}$ P25 TiO_2 to the medium. As reported before [32], the TiO_2 particles upon exposure/immersion to water form surface hydroxyl groups and protons via water splitting. Such surface hydroxyls can be considered as reactive amphoteric sites. At pH below the IEP of TiO_2 (measured to be ca. 6.1), the particles are positively charged due to protonation of the surface hydroxyl groups: $TiOH_2^+$.

Table 0-1: The influence of $Zn(NO_3)_2$ concentration on suspension stability and deposit quality; solvent was 5% *v/v* isopropanol-DI water mixture at natural pH

Additive	***Deposit quality***	***Zeta potential (mV)***	***Aggregate size (nm)***	***Suspension pH***
Without additive	Poor adhesion and not reproducible	28±1	130±8	4
10^{-4}M $Zn(NO_3)_2$	No deposition	30±0	128±4	4.12
$5*10^{-4}$M $Zn(NO_3)_2$	Poor adhesion	31±2	149±4	4.18
10^{-3}M $Zn(NO_3)_2$	Fair quality and adhesion	36±2	66±2	4.22
$5*10^{-3}$M $Zn(NO_3)_2$	Unstable suspension, No deposition	34±1	248±5	4.33
10^{-2}M $Zn(NO_3)_2$	Unstable suspension, No deposition	19±3	569±46	4.37

It is known that the zeta potential is an important indicator of suspension stability against coagulation or settling and also of the rate of particle deposition during EPD [33]. The zeta potential for the suspension without any additive was +28 *mV* (Table 0-1). This value may mean that although the particles are positively charged, they are not necessarily fully dispersed. The zeta potential of the TiO_2 suspension changed as a function of the concentration of $Zn(NO_3)_2$, as shown in Table 0-1. The zeta potential increased with increasing concentration reaching a

maximum of 36 mV at 10^{-3} M. It decreased, however, upon further concentration increase (19mV at 10^{-2} M). High salt concentration or in other words high ionic strength tends to compress the double layer leading to zeta potential decrease and suspension instability. At high ionic concentration, not only the extent of aggregation but also the electrophoretic particle mobility decreases thus ultimately the deposit quality deteriorates at a certain limit, which in our case appeared to be 10^{-3} M $Zn(NO_3)_2$.

Sedimentation tests were also carried out by measuring absorbance versus time for the different $Zn(NO_3)_2$ concentration suspensions. As shown in Figure 0-1, increasing the $Zn(NO_3)_2$ concentration too much leads to instability and quick sedimentation, in correlation with the zeta potential results.

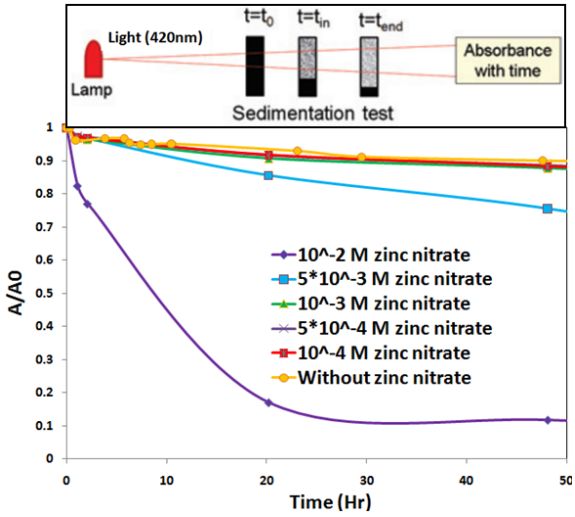

Figure 0-1. The influence of $Zn(NO_3)_2$ concentration on the absorbance of TiO_2 nanoparticle suspensions, natural pH-see Table 0-1.

4.4.2. Film Deposition and Characterization

As indicated in Table 0-1, in the case of EPD in the absence of $Zn(NO_3)_2$, the produced TiO_2 film was not reproducible due to poor adhesion. Moreover, it was not possible to build films above 10.5μm thickness (after annealing). In order to overcome these problems EPD was performed with 10^{-3} M $Zn(NO_3)_2$ present,

which was found to give optimum suspension and deposition conditions in terms of high zeta potential, small aggregate size and film adhesibility-refer to Table 0-1. According to Stoke's law small particles migrate faster within the electric field than large ones such that significant increase in the adhesion is achieved by higher mobility of aggregate leading to stronger attachment to the substrate. But more importantly as different researchers have previously demonstrated the local pH increases at the cathode as consequence of hydrogen ion reduction [13-15] causing in turn metal hydroxide to form that helps bind the particles on the substrate [14, 34]. This mechanism of deposition is proposed to be responsible for the observed improved film adhesion. The pH localization mechanism during EPD has been theoretically [35] and experimentally verified for aqueous suspension recently [36-37]. Thus the pH in the vicinity of the cathode has been shown to increase as consequence of hydrogen ion reduction/OH^- (Equation 0-1).

$$2H_2O + 2e^- \rightarrow H_2 + 2OH^- \qquad (0\text{-}1)$$

Upon interfacial pH increase as result of the cathodic generation of OH^- (Equation 0-1), it is postulated that zinc hydroxide forms (Equation 0-2) acting as "nanoglue" for the physically deposited TiO_2 particles hence promoting the building of an effective film. Apparently during annealing of the film the zinc hydroxide transforms to ZnO.

$$Zn^{2+} + 2\,OH^- \rightarrow Zn(OH)_2 \xrightarrow{\text{Annealing}} ZnO \qquad (0\text{-}2)$$

In order to confirm the presence of Zn within the whole film, an EDS spectrum from the cross section of the film was collected and shown in Figure 0-2(a). In addition to Si, Sn, O of which FTO is composed, Zn and Ti peaks can clearly be identified. According to the line scan (Figure 0-2(b), Zn appears within the whole EPD film of TiO_2. Hence, we can conclude that upon annealing a composite TiO_2-ZnO thin film was built/fabricated.

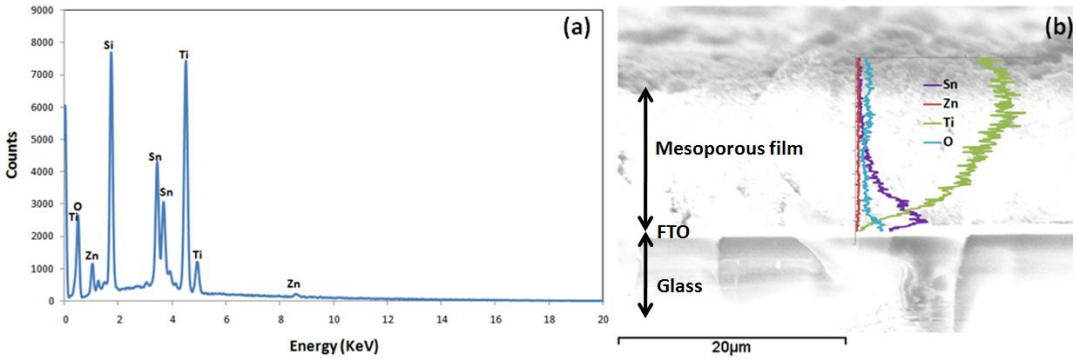

Figure 0-2. (a) EDS spectra for BP film and (b) Line scan of the BP film cross section.

Figure 0-3 and Figure 0-4 show FEG-SEM images of the top surface and cross section of annealed TiO_2-ZnO films prepared at various deposition times. No distinct ZnO particles could be seen apparently reflecting the very small equivalent amount of ZnO in comparison to that of TiO_2 in the suspension, ~1.5%, that makes their detection difficult. It is conceivable that at least in part ZnO deposited on the surface of the TiO_2 particles given that the precursor Zn^{2+} cations are part of the particle surrounding electrical double layers. Figure 0-3(a) and (c) depict the morphology of similar thickness (~8 μm) films without and with addition of $Zn(NO_3)_2$, respectively. AFM analysis indicated the film obtained in the presence of $Zn(NO_3)_2$ to have slightly lower surface roughness; the average roughness decreased from 394 nm to 367 nm with the addition of $Zn(NO_3)_2$, this being attributed to the smaller aggregate size-see Table 0-1. Nevertheless the overall surface area of the film remained essentially the same (refer to Figure 0-5), i.e. equivalent dye loading was obtained with or without the added $Zn(NO_3)_2$. Insets in Figure 0-3 show high magnification FEG-SEM images that provide evidence of good overall mesoporous film microstructure. The mesoporous nature of the produced films was verified via BET surface analysis and determination of the pore size distribution as shown in Figure 0-5. Thus the surface areas of both B (TiO_2 only) and BP (TiO_2-ZnO) films are very close together apparently reflecting the fact that in both films, TiO_2 (P25) is the main component. The small amount of ZnO that co-deposits in the case of BP film did not influence the surface area.

In terms of average pore size this was about 40 nm, i.e. well within the range of mesoporous materials.

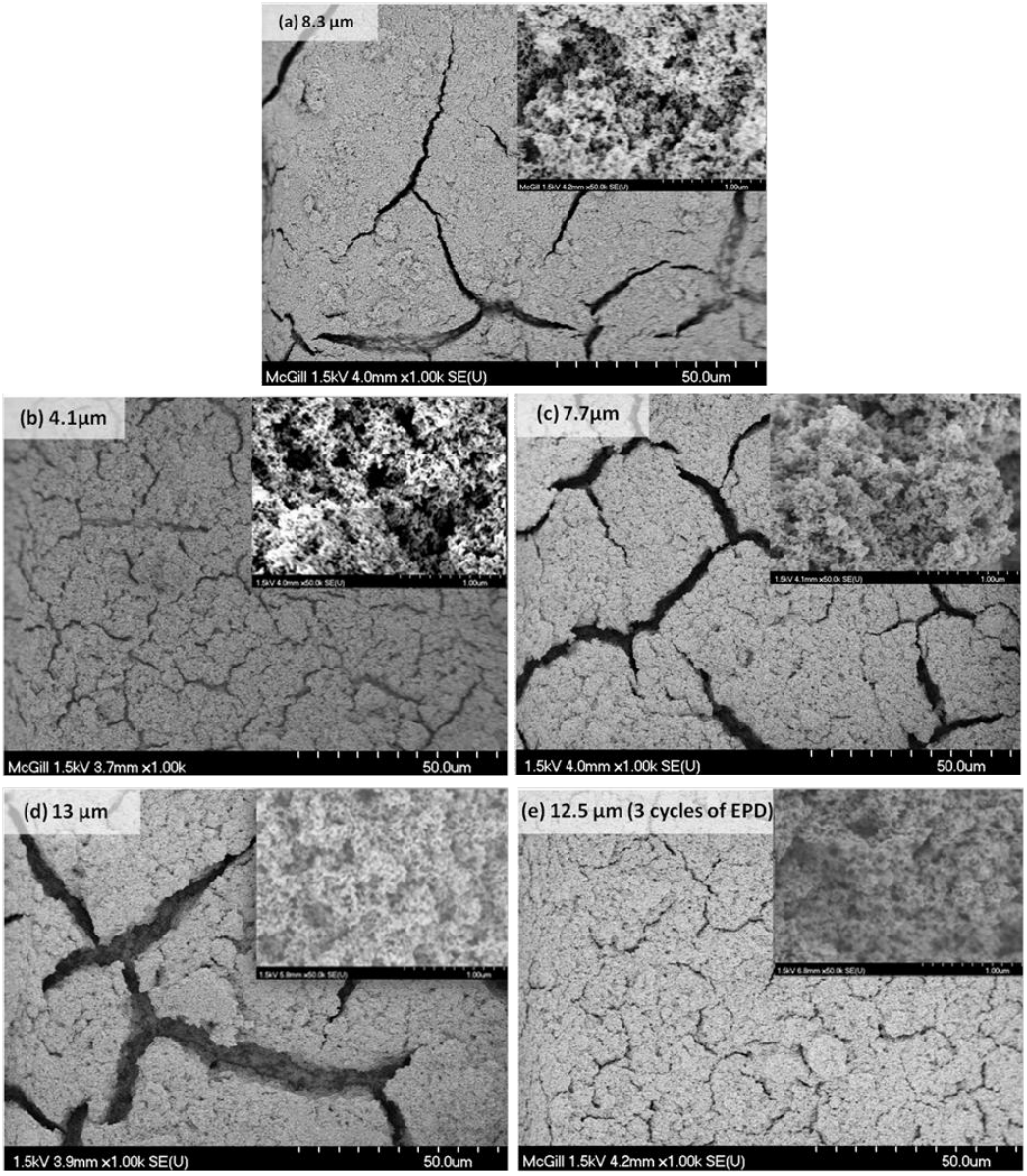

Figure 0-3. Top view SEM images of EPD films of varying thickness obtained at different deposition times from (a) suspension without $Zn(NO_3)_2$ addition and (b, c, d and e) with addition of 10^{-3} M $Zn(NO_3)_2$. (b, c, and d) films are single layer and (e) is 3-layer film. Insets show high magnification images.

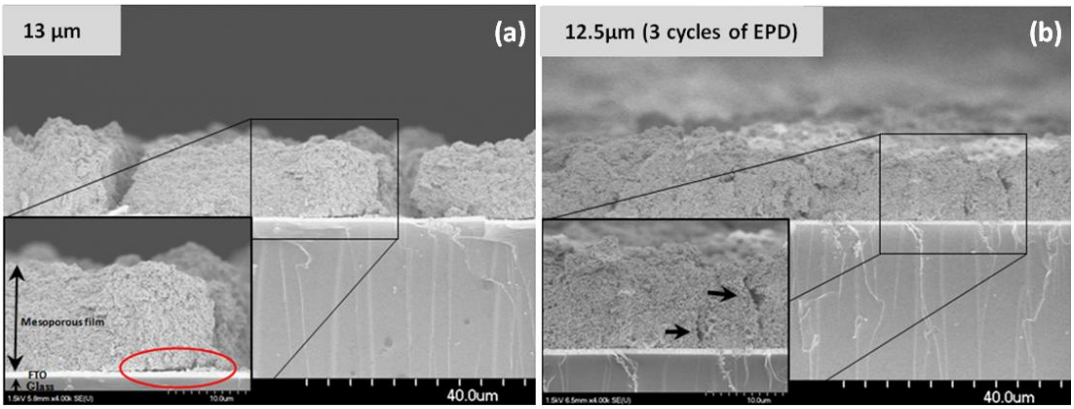

Figure 0-4. Cross section SEM images of thin films deposited from suspension containing 10^{-3} M $Zn(NO_3)_2$ by employing different number of EPD cycles: (a) single-layer film and (b) three-layer film obtained with 3 EPD cycles.

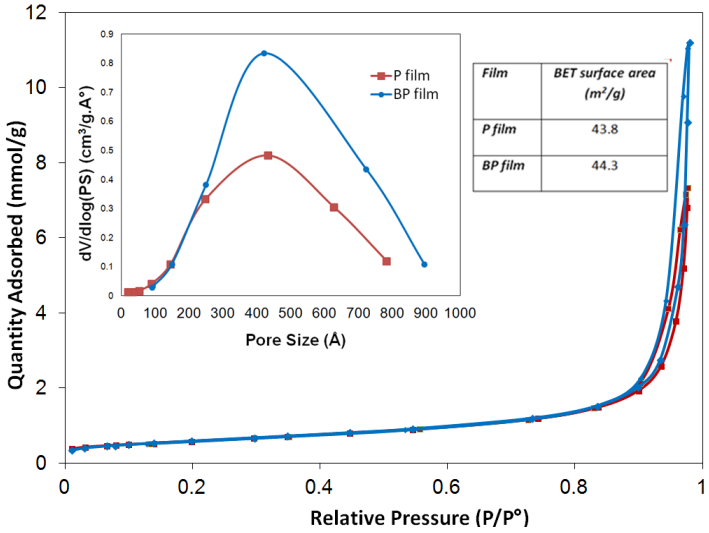

Figure 0-5. Pore size distribution of both P (TiO_2 only) and BP (TiO_2-ZnO composite) film obtained from BET surface analysis

Increasing the film thickness with prolonged deposition resulted in formation of cracks on the film (Figure 0-3 (b), (c), and (d)). Such cracks decrease film adhesion and increase current loss via exposure of the bare FTO glass surface to electrolyte, hence they are undesirable. Crack formation apparently originates from stresses induced within the film as a result of rapid evaporation of water during the drying/annealing process. Cracking can be reduced by minimizing

capillary stresses [38]. Hence 5% *v/v* isopropanol was added as a co-solvent in order to lower the surface tension of de-ionized water from 72.6 $mN.m^{-1}$ down to 49.6. Another way tried to reduce cracking was to apply multiple thin layer deposition cycles via intermittent drying. This proved indeed very effective as it can be evaluated by comparing two films of similar thickness (12-13 μm), namely the single layer BP film of Figure 0-3(d) and the 3-layers BP film of Figure 0-3(e), the latter obtained via 3 EPD cycles of 5 min each (3x~ 4 μm film/cycle). These films (single-layer vs. 3-layer) are also compared in terms of their cross section microstructures in Figure 0-4. As shown in Figure 0-4(a), in the case of a thick film produced in a single EPD cycle, the film/substrate interface exhibits gaps in addition to formation of large cracks. By contrast the 3-layer film of Figure 0-4(b) (prepared by 3 EPD cycles), was associated with much smaller cracks and more importantly not interfacial gaps. Elimination of the latter helps reduce the occurrence of electron loss due to coming in contact of electrolyte with the bare surface of the conducting glass; a postulation that is proven later via electrochemical estimation of the charge recombination resistance and electron lifetime.

4.4.3. DSSC performance

DSSCs were fabricated using EPD-prepared photoanodes from the two different suspensions (with and without $Zn(NO_3)_2$). The photocurrent-voltage properties of the various DSSCs are shown Figure 0-6 and summarized in Table 0-2. As mentioned before, in the absence of $Zn(NO_3)_2$ we could not deposit above 10.5 μm thicknesses due to the poor adhesion of the film to the substrate. The highest conversion efficiency obtained in the absence of $Zn(NO_3)_2$ was 3.34 % for a film with 9.1μm thickness (P film). In the presence of $Zn(NO_3)_2$ the corresponding efficiency (for similar thickness film) improved to 4.48% (composite TiO_2-ZnO BP film). It is worth noting that the V_{OC} was remarkably improved in the case of the composite BP film in comparison to the P film (TiO_2 only). Since V_{OC} is defined as the difference between the Fermi level of the

photoelectrode semiconductor and the redox potential of the electrolyte [39], the observed improvement in V_{OC} may be thought to be the result of a shift of TiO_2's Fermi level and/or the result of a decrease in charge recombination [40-41]. In our case, it is most likely the synergistic contribution of both effects that caused the improvement of the V_{OC}. It is postulated that inter-particle necking via ZnO co-deposition suppressed the recombination of the photoinjected electrons as confirmed by the dark current measurements presented in Figure 0-6; this observation is in agreement with Meng et al. [42]. On the other hand, similarly to Liu et al. [23] formation of ZnO as a potential blocking layer at the FTO/TiO_2 interface may be further thought as leading to a decrease in charge recombination as well. This blocking barrier can also lead to the build up of the electron density within the thin film hence giving rise to a more negative Fermi level and thus a larger V_{OC}.

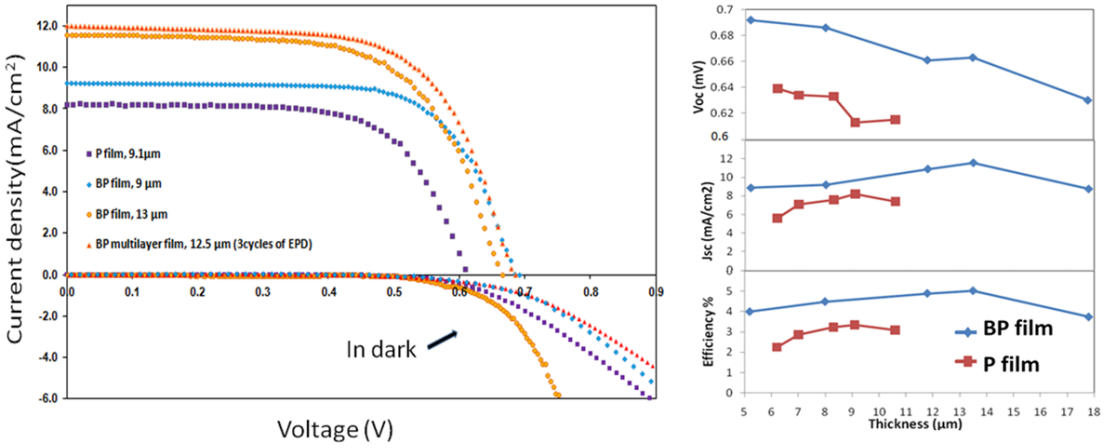

Figure 0-6. (a) *J-V* curves of various DSSCs and (b) the effect of film (single-layer) thickness on photovoltaic parameters.

Table 0-2: Photovoltaic parameters of different solar cells.

Film	Film thickness (μm)	J_{sc} ($mA\ cm^{-2}$)	V_{OC} (V)	Fill factor	η_{max} (%)	η_{ave} (%)
P film [1]	9.1	8.2	0.61	0.70	3.34	3.21±0.11
BP film [2]	9.0	9.2	0.69	0.71	4.48	4.31±0.14
BP film	11.7	10.9	0.66	0.68	4.88	4.80±0.05
BP film	13.0	11.6	0.66	0.65	5.01	4.98±0.04
BP film	15.0	10.9	0.64	0.68	4.81	4.66±0.15
BP film	17.8	8.7	0.63	0.68	3.73	3.73
BP 3 layers film	12.5	12.0	0.68	0.67	5.52	5.44±0.10
BP 4 layers film	15.6	12.3	0.66	0.70	5.7	5.62±0.06
BP 5 layers film	18.3	13.5	0.66	0.69	6.19	6.08±0.10
BP 6 layers film	21.8	13.0	0.62	0.62	5.03	4.91±0.16

[1] "P film" denotes a pure TiO_2 film without the presence of ZnO.
[2] "BP film" denotes a composite TiO_2-ZnO film.

The effect of film thickness on *PV* parameters is presented in Table 0-2. In the case of the BP (TiO_2-ZnO) film, the J_{sc} and conversion efficiency increased to 11.6 $mA.cm^{-2}$ and 5.01% as the thickness of film increased to 13 μm. It is noted that these numbers were obtained with a single transparent film; i.e. no scattering layer was employed as done normally [29]. With further thickness increase (17.8 μm), the conversion efficiency of the single-layer BP film decreased down to 3.73%. Similar behaviour (i.e. existence of an optimum film thickness beyond which performance deteriorates) has been observed with conventional film deposited electrodes prepared by screen-printing [43].

On the other hand, the conversion efficiency was further improved to 5.52% for the same total film thickness (13 μm), when a multilayer film (3 layers) was built reaching 6.19% with a 5 layer-film having total thickness 18.3 μm. To our best knowledge, this efficiency is one of the highest value obtained with an aqueous suspension of low cost commercial P25 powder without any special post treatment such as compression or employment of a scattering layer.

The optimum thickness of single layer BP films was determined to be about 13 μm. It is shown (Table 0-2) that η and J_{SC} tend to decrease above the optimum

thickness. This decrease is most likely due to electron losses within the layer as a result of poor adhesion [44] and large crack formation in the thicker film [45] as already remarked earlier. On the other hand, this optimum thickness for multilayer structure shifted to 18.5 μm. This can be due to the superior film structure achieved by multilayer deposition as evident by the significant reduction of crack size/occurrence and adhesion. The thicker the film becomes, the more electrons are injected into TiO_2 due to the higher dye loading. At the same time, as the film thickness continues to increase, electrons in TiO_2 need to move a longer distance to reach the FTO increasing the chance of loss due to carrier recombination from the encounter of more defects and charge traps [44-46]. This again results in an optimum thickness or optimum number of deposition cycles (number of layers), which varies from one film construction to the other. The multilayer constructed films simply enable us to shift the optimum thickness to higher value due to its superior structure compared to the single layer film.

Although the dark current in DSSCs is not a direct measurement of the charge recombination process, it can be used for first level evaluation [47-48]. The dark current is deemed to originate from bare FTO sites due to poor film adhesion and cracking as well as due to the film's mesoporous structure [49]. These features provide pathways for the redox electrolyte to penetrate through the film and contact the naked FTO surface. The dark current presented in Figure 0-6(a) shows higher rate of recombination from the P (TiO_2 alone) electrode in comparison to the BP (TiO_2-ZnO) electrodes. Reduced current leakage via back electron transfer from the FTO/TiO_2 film interface by introducing the $Zn(NO_3)_2$ to the suspension can imply the formation of a ZnO blocking barrier in the film. The obvious further reduction of the dark current with the multilayer BP film suggests that this strategy is effective in minimizing charge recombination due to less bare FTO sites exposed to the electrolyte as evident and discussed with the cross section SEM images of Figure 0-4. This conclusion is further confirmed by our EIS data discussed in the following section.

4.4.4. Electrochemical analysis

The OCVD (Open Circuit Voltage Decay) technique is a powerful tool to probe the kinetics of recombination. It monitors the transient of V_{OC} during relaxation from the illuminated steady-state to the dark equilibrium. Unlike frequency or steady-state-based methods, it provides a continuous reading of electron lifetime as a function of V_{OC} at high-voltage resolution [50]. The V_{OC} decay reflects the decrease of electron concentration in TiO_2, which is mainly caused by charge recombination [23].

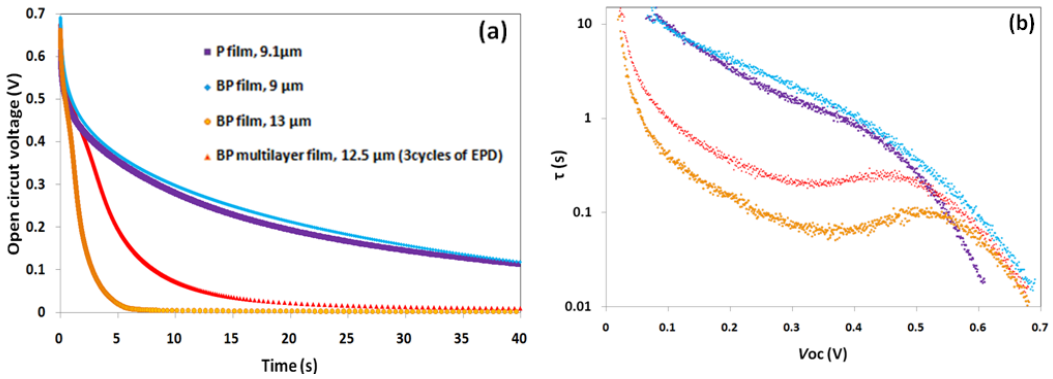

Figure 0-7. (a) V_{OC} decay versus time and (b) Electron lifetime (τ) as a function of V_{OC} for DSSCs based on different EPD photoanodes.

Figure 0-7(a) shows the V_{OC} decay curves of DSSCs prepared with ~ 9 μm thick BP and P films as well as single and multilayer BP films. It is that the decay rate of the cell based on P (TiO_2 alone) electrode is faster than that of BP (TiO_2-ZnO) electrode, which confirms the above conclusion that the formation of composite TiO_2-ZnO film contributes to a longer electron lifetime. The same trend was seen with preparation of multilayer film.

As reported before [50], the electron lifetime (τ) can be derived from the rate of V_{OC} decay according to Equation 0-3:

$$\tau = -\frac{k_B T}{e}\left(\frac{dV_{OC}}{dt}\right)^{-1} \qquad (0\text{-}3)$$

where k_B is the Boltzmann constant, T is the temperature, and e is the electron charge. Figure 0-7(b) shows the results of the dependence of lifetime on the V_{OC} for the different EPD prepared DSSCs. From these results it is once more evident that the co-deposition of $Zn(OH)_2$ along TiO_2 and its subsequent conversion to ZnO, as discussed before, resulted in reduction of photoelectron recombination and hence longer electron lifetime. In addition, the multi layer film clearly demonstrated longer electron lifetime compared to the single layer. This suggests that the injected electrons from the excited dye can survive longer and transport without undergoing losses at the bare FTO surface due to better adhesion and less deep or large sized cracks.

Electrochemical impedance spectroscopy (EIS) has been widely used over the past several years to study the kinetics of electrochemical and photoelectrochemical processes including the explanation of charge transfer processes (both electronic and ionic) occurring in the DSSC [51]. A typical EIS spectrum for a DSSC exhibits three semicircles in the Nyquist plot. The left (high frequency) arc corresponds to the charge transfer process at the Pt counter electrode/electrolyte and FTO/TiO_2 interfaces (R_{CE}); the central arc is related to charge transport resistance in TiO_2 film (R_t), recombination at the TiO_2/dye/electrolyte interfaces (R_{rec}) and the chemical capacitance (C_μ); and the right (low frequency) arc is attributed to Nernst diffusion process of I^-/I_3^- electrolyte [52]. The C_μ, R_{rec} , R_{CE}, and R_t were extracted from EIS measurements under illumination over a range of applied voltages by using the model developed by Fabregat-Santiago et al. [53-55] (see Figure 0-8). By performing EIS analysis at varying applied voltage the shift in conduction band could be determined by the displacement observed in C_μ (chemical capacitance), this allowing for unequivocal interpretation of observed differences in R_{rec} [55].

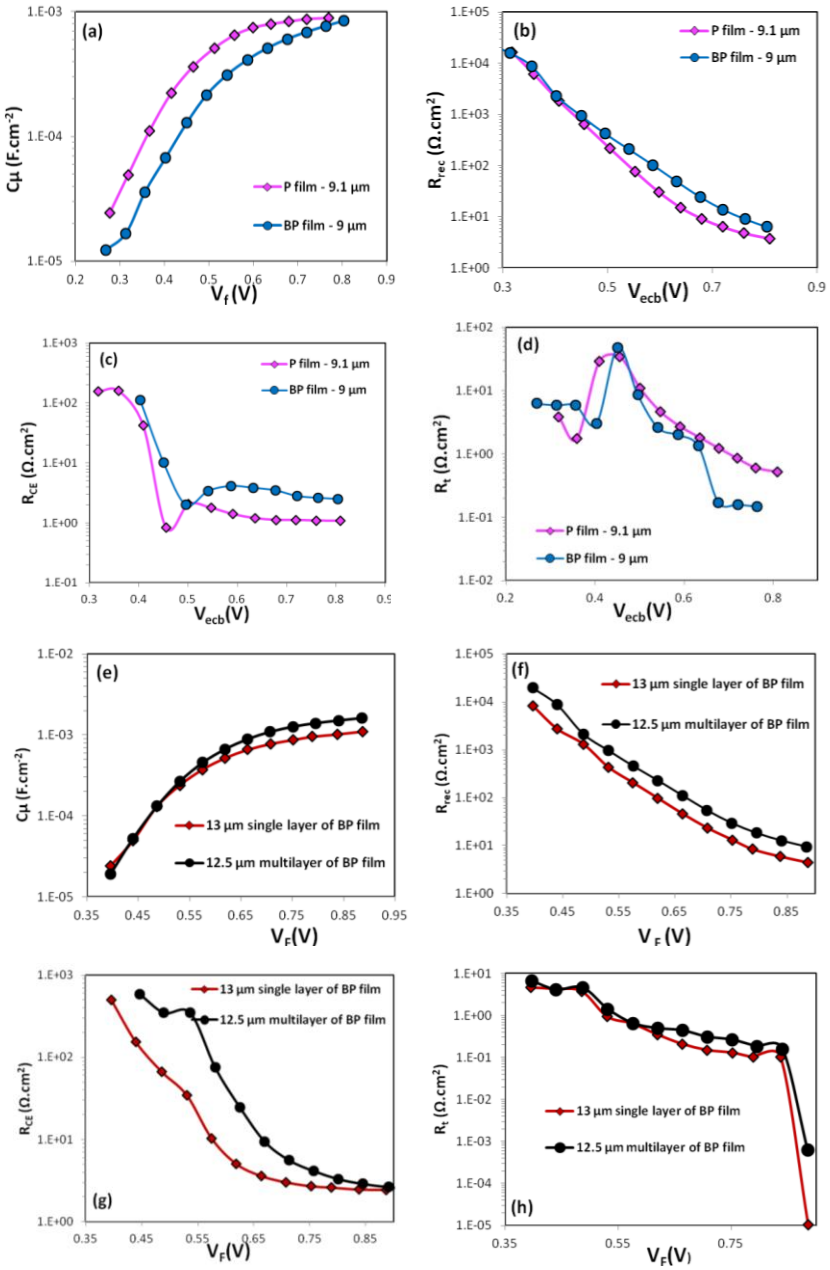

Figure 0-8. Impedance parameters, C_{μ} (chemical capacitance), R_{rec} (recombination resistance at the TiO_2/dye/electrolyte interface), R_{CE} (charge transfer resistance at the Pt counter electrode/electrolyte and FTO/TiO_2 interfaces), and Rt (charge transport resistanc resistance in TiO_2 film), of the various electrodes as function of the voltage drop, V_F or V_{ecb} (where the displacement of the TiO_2 CB has been removed).

C_μ is plotted in Figure 0-8 against the voltage drop at the sensitized electrode, V_F. The latter is obtained by subtracting the voltage drop of series resistance (V_{series}) from the applied potential (V_{app}): $V_F = V_{app} - V_{series}$ [55]. V_F is proportional to the rise of the Fermi level of electrons in TiO_2, $V_F = (E_{Fn}-E_{F0})/q$, where q is the positive elementary charge and E_{Fn} and E_{F0} are the electron Fermi level and the electron Fermi level at equilibrium, respectively. According to Figure 0-8(a) data, the chemical capacitance of the composite (TiO_2-ZnO) BP film has shifted to higher V_F than the simple (TiO_2) P film indicating a displacement of the TiO_2 conduction band (CB) edge. The upward shift of the TiO_2 conduction band arising from the presence of ZnO in the titania film is responsible for the observed (data in Table 0-2) increase in V_{OC} (56). As mentioned before, ZnO owing to its higher conduction band compared to TiO_2, acts as blocking layer, causing accumulation of electron in the film and thus the upward shift of the conduction band and higher V_{OC} [23].

In order to evaluate properly the R_{rec}, we had to plot the R_{rec} of different cells at the same equivalent value of the position of the conduction band (i.e., the same distance between the electron Fermi level, E_{Fn}, and the CB of TiO_2 (E_{CB})), or in other words same electron density in TiO_2, since the recombination rate is proportional to electron density. This was done by removing the displacement of CB and plotting R_{rec} against the voltage drop in a common equivalent conduction band (V_{ecb}) (Figure 0-8 (b)). In order to apply this CB correction on the different TiO_2 films, the chemical capacitance curve of BP film was taken as reference and the curve of P film was shifted until the two overlapped. The same shift applied to the chemical capacitance, was applied to R_{rec} , R_{CE}, and R_t in order to plot them vs V_{ecb}. The methods to plot the C_μ and R_{rec} against V_F and V_{ecb} from EIS measurements have been previously reported [54, 56-58], and extensively reviewed in [55]. As it can be seen in Figure 0-8(b), the resistance of interfacial charge transfer from the TiO_2 to triiodide in the electrolyte (R_{rec}) is higher in the BP film than that in the P film reflecting the formation of ZnO. In other words the presence of ZnO suppresses the rate of recombination loss.

In addition, the R_{CE}, which is given by the sum of resistances of counter electrode/electrolyte and FTO/TiO_2 interfaces, increased to some extent upon using the BP electrode (see Figure 0-8(c). Since the counter electrodes were prepared in the same way for both DSSCs, the observed difference must be attributed to the FTO/TiO_2 interface. In other words ZnO should be held responsible for the increase of R_{CE}. A similar increase in R_{CE} was reported for the formation of a blocking layer such as ZnO at FTO/TiO_2 interface [23] or formation of TiO_2 on a flexible Ti substrate after annealing [59]. These findings provide further supporting evidence for the blocking role of ZnO, which causes higher interfacial resistance due to its more negative conduction band of ZnO compared to that of TiO_2. These results are in a good consistency with the reduced dark current leakage, longer electron lifetimes and higher V_{OC} determined by OCVD and *J-V* curve characterization respectively.

The electron conductivity in the TiO_2 film, $\sigma_n = L/R_t$, can be evaluated where R_t and L are the electron transport resistance and film thickness, respectively [54]. As shown in Figure 0-8(d), the R_t of the BP composite film is lower than that of the P film, which can be translated to improved electron conductivity in the composite BP film. Therefore, it can be deduced that interstitial formation of ZnO within the TiO_2 film provides better particle interconnections and improved electron percolation.

As shown in Figure 0-8(e) and (h), multilayer film construction did not cause a noticeable shift in C_μ or R_t, this being apparently so due to the same composition of the two (single and multilayer) films. However, the multilayer BP films resulted in higher R_{rec} and R_{CE} compared to the single layer films (Figure 0-8(f) and (g)). This indirectly indicates that the multilayer EPD method improves adherence, increases the number of electron pathways to the FTO and reduces electron leakage to bare sites of FTO due to substantial reduction in crack formation and propagation. As a result of these beneficial effects a 24% increase (6.19 vs. 5.01%-see Table 0-2 data) in conversion efficiency was realized.

4.5. Conclusion

In summary, an aqueous-based suspension made of 5 $g.L^{-1}$ P25 nanotitania particles dispersed in 5 % (*v/v*) isopropanol-water mixture spiked with 10^{-3}M $Zn(NO_3)_2$ was developed and successfully employed to fabrication of composite TiO_2-ZnO photoanodes for DSSCs. We demonstrated the influence of adding $Zn(NO_3)_2$ to the suspension in order to prepare stable suspension and overcome the main problem of aqueous-based EPD, which is poor film adhesion and cracking. We took advantage of cathodic deposition of $Zn(OH)_2$ and its conversion to ZnO after annealing. Various supporting data indicates ZnO to behave as a potential blocking layer due to its more negative conduction band compared to TiO_2. It was found to suppress the dark current from substrate to electrolyte by increasing the charge recombination resistance and prolong the lifetime of the photoelectrons. In addition, fabrication of multilayer film by repeated EPD cycles and intermittent drying resulted in 24% conversion efficiency improvement due to superior film properties in terms of enhanced adhesion and reduced crack formation.

4.6. Acknowledgments

This research is supported via a NSERC strategic project grant and sponsored by CIS Solar, Versatilis, Targray Technology International Inc. and Hydro-Quebec's Energy Conversion and Storage Unit. Professor N. Tufenkji is thanked for permission to use the Zetasizer in her laboratory.

4.7. References

1. Hagfeldt A, Boschloo G, Sun L, Kloo L, Pettersson H. Dye-Sensitized Solar Cells. Chemical Reviews 2010;110(11):6595-663.

2. Grätzel M. Dye-sensitized solar cells. Journal of Photochemistry and Photobiology C: Photochemistry Reviews 2003;4(2):145-53.

3. Meyer GJ. The 2010 Millennium Technology Grand Prize: Dye-Sensitized Solar Cells. ACS Nano 2010;4(8):4337-43.

4. Bisquert J. Dilemmas of Dye-Sensitized Solar Cells. ChemPhysChem 2011;12(9):1633-36.

5. Grinis L, Dor S, Ofir A, Zaban A. Electrophoretic deposition and compression of titania nanoparticle films for dye-sensitized solar cells. Journal of Photochemistry and Photobiology A: Chemistry 2008;198(1):52-59.

6. Chen H-W, Huang K-C, Hsu C-Y, Lin C-Y, Chen J-G, Lee C-P, et al. Electrophoretic deposition of TiO_2 film on titanium foil for a flexible dye-sensitized solar cell. Electrochimica Acta 2011;56(23):7991-98.

7. Grinis L, Kotlyar S, Rühle S, Grinblat J, Zaban A. Conformal Nano-Sized Inorganic Coatings on Mesoporous TiO_2 Films for Low-Temperature Dye-Sensitized Solar Cell Fabrication. Advanced Functional Materials 2010;20(2):282-88.

8. Tang F, Uchikoshi T, Ozawa K, Sakka Y. Effect of polyethylenimine on the dispersion and electrophoretic deposition of nano-sized titania aqueous suspensions. Journal of the European Ceramic Society 2006;26(9):1555-60.

9. Lebrette S, Pagnoux C, Abélard P. Fabrication of titania dense layers by electrophoretic deposition in aqueous media. Journal of the European Ceramic Society 2006;26(13):2727-34.

10. Zhao L, Yu J, Fan J, Zhai P, Wang S. Dye-sensitized solar cells based on ordered titanate nanotube films fabricated by electrophoretic deposition method. Electrochemistry Communications 2009;11(10):2052-55.

11. Kim G-S, Seo H-K, Godble VP, Kim Y-S, Yang OB, Shin H-S. Electrophoretic deposition of titanate nanotubes from commercial titania nanoparticles: Application to dye-sensitized solar cells. Electrochemistry Communications 2006;8(6):961-66.

12. Van der Biest O, Vandeperre LJ. Electrophoretic deposition of materials. Annual Review of Materials Science 1999;29(1):327-52.

13. Russ BE, Talbot JB. A Study of the Adhesion of Electrophoretically Deposited Phosphors. Journal of The Electrochemical Society 1998;145(4):1245-52.

14. Russ BE, Talbot JB. An Analysis of the Binder Formation in Electrophoretic Deposition. Journal of The Electrochemical Society 1998;145(4):1253-56.

15. Shane MJ, Talbot JB, Kinney BG, Sluzky E, Hesse KR. Electrophoretic Deposition of Phosphors: II. Deposition Experiments and Analysis. Journal of Colloid and Interface Science 1994;165(2):334-40.

16. Liu X, Luo Y, Li H, Fan Y, Yu Z, Lin Y, et al. Room temperature fabrication of porous ZnO photoelectrodes for flexible dye-sensitized solar cells. Chemical Communications 2007(27):2847-49.

17. Kakiuchi K, Hosono E, Fujihara S. Enhanced photoelectrochemical performance of ZnO electrodes sensitized with N-719. Journal of Photochemistry and Photobiology A: Chemistry 2006;179(1-2):81-86.

18. Wang ZL. ZnO nanowire and nanobelt platform for nanotechnology. Materials Science and Engineering: R: Reports 2009;64(3-4):33-71.

19. Kim S-S, Yum J-H, Sung Y-E. Flexible dye-sensitized solar cells using ZnO coated TiO_2 nanoparticles. Journal of Photochemistry and Photobiology A: Chemistry 2005;171(3):269-73.

20. Wu S, Han H, Tai Q, Zhang J, Chen BL, Xu S, et al. Improvement in dye-sensitized solar cells with a ZnO-coated TiO_2 electrode by rf magnetron sputtering. Applied Physics Letters 2008;92(12).

21. Roh SJ, Mane RS, Min SK, Lee WJ, Lokhande CD, Han SH. Achievement of 4.51% conversion efficiency using ZnO recombination barrier layer in TiO_2 based dye-sensitized solar cells. Applied Physics Letters 2006;89(25).

22. Kim S-S, Yum J-H, Sung Y-E. Improved performance of a dye-sensitized solar cell using a TiO_2/ZnO/Eosin Y electrode. Solar Energy Materials and Solar Cells 2003;79(4):495-505.

23. Liu Y, Sun X, Tai Q, Hu H, Chen B, Huang N, et al. Efficiency enhancement in dye-sensitized solar cells by interfacial modification of conducting glass/mesoporous TiO_2 using a novel ZnO compact blocking film. Journal of Power Sources 2011;196(1):475-81.

24. Zhu K, Schiff EA, Park NG, Van de Lagemaat J, Frank AJ. Determining the locus for photocarrier recombination in dye-sensitized solar cells. Applied Physics Letters 2002;80(4):685.

25. Manríquez J, Godínez LA. Tuning the structural, electrical and optical properties of Ti(III)-doped nanocrystalline TiO_2 films by electrophoretic deposition time. Thin Solid Films 2007;515(7-8):3402-13.

26. Liufu S, Xiao H, Li Y. Adsorption of poly(acrylic acid) onto the surface of titanium dioxide and the colloidal stability of aqueous suspension. Journal of Colloid and Interface Science 2005;281(1):155-63.

27. Eremenko BV, Bezuglaya TN, Savitskaya AN, Malysheva ML, Kozlov IS, Bogodist LG. Stability of Aqueous Dispersions of the Hydrated Titanium Dioxide Prepared by Titanium Tetrachloride Hydrolysis. Colloid Journal 2001;63(2):173-78.

28. Lee K, Charbonneau C, Shan G, Demopoulos G, Gauvin R. Nanocrystalline TiO_2 thin film electrodes for dye-sensitized solar cell applications. JOM Journal of the Minerals, Metals and Materials Society 2009;61(4):52-57.

29. Ito S, Miura H, Uchida S, Takata M, Sumioka K, Liska P, et al. High-conversion-efficiency organic dye-sensitized solar cells with a novel indoline dye. Chemical Communications 2008(41):5194-96.

30. Fabregat-Santiago F, Garcia-Canadas J, Palomares E, Clifford JN, Haque SA, Durrant JR, et al. The origin of slow electron recombination processes in dye-sensitized solar cells with alumina barrier coatings. Journal of applied physics 2004;96(11):6903-07.

31. Bisquert J, Zaban A, Greenshtein M, Mora-Seró I. Determination of Rate Constants for Charge Transfer and the Distribution of Semiconductor and Electrolyte Electronic Energy Levels in Dye-Sensitized Solar Cells by Open-Circuit Photovoltage Decay Method. Journal of the American Chemical Society 2004;126(41):13550-59.

32. Radice S, Bradbury CR, Michler J, Mischler S. Critical particle concentration in electrophoretic deposition. Journal of the European Ceramic Society 2010;30(5):1079-88.

33. Shane MJ, Talbot JB, Sluzky E, Hesse KR. Zeta potential of phosphors. Colloids and Surfaces A: Physicochemical and Engineering Aspects 1995;96(3):301-05.

34. Siracuse JA, Talbot JB, Sluzky E, Hesse KR. The Adhesive Agent in Cataphoretically Coated Phosphor Screens. Journal of The Electrochemical Society 1990;137(1):346-48.

35. De D, Nicholson PS. Role of Ionic Depletion in Deposition during Electrophoretic Deposition. Journal of the American Ceramic Society 1999;82(11):3031-36.

36. Besra L, Uchikoshi T, Suzuki TS, Sakka Y. Experimental verification of pH localization mechanism of particle consolidation at the electrode/solution interface and its application to pulsed DC electrophoretic deposition (EPD). Journal of the European Ceramic Society 2010;30(5):1187-93.

37. Mishra M, Bhattacharjee S, Besra L, Sharma HS, Uchikoshi T, Sakka Y. Effect of pH localization on microstructure evolution of deposits during aqueous electrophoretic deposition (EPD). Journal of the European Ceramic Society 2010;30(12):2467-73.

38. Sarkar P, De D, Rho H. Synthesis and microstructural manipulation of ceramics by electrophoretic deposition. Journal of Materials Science 2004;39(3):819-23.

39. Burnside S, Moser J-E, Brooks K, Grätzel M, Cahen D. Nanocrystalline Mesoporous Strontium Titanate as Photoelectrode Material for Photosensitized Solar Devices: Increasing Photovoltage through Flatband Potential Engineering. The Journal of Physical Chemistry B 1999;103(43):9328-32.

40. Doh J-G, Hong JS, Vittal R, Kang MG, Park N-G, Kim K-J. Enhancement of Photocurrent and Photovoltage of Dye-Sensitized Solar Cells with TiO_2 Film Deposited on Indium Zinc Oxide Substrate. Chemistry of Materials 2003;16(3):493-97.

41. Xia J, Masaki N, Jiang K, Yanagida S. Sputtered Nb_2O_5 as a Novel Blocking Layer at Conducting Glass/ TiO_2 Interfaces in Dye-Sensitized Ionic Liquid Solar Cells. The Journal of Physical Chemistry C 2007;111(22):8092-97.

42. Meng QB, Takahashi K, Zhang XT, Sutanto I, Rao TN, Sato O, et al. Fabrication of an Efficient Solid-State Dye-Sensitized Solar Cell. Langmuir 2003;19(9):3572-74.

43. Ito S, Murakami TN, Comte P, Liska P, Grätzel C, Nazeeruddin MK, et al. Fabrication of thin film dye sensitized solar cells with solar to electric power conversion efficiency over 10%. Thin Solid Films 2008;516(14):4613-19.

44. Miyasaka T, Kijitori Y. Low-Temperature Fabrication of Dye-Sensitized Plastic Electrodes by Electrophoretic Preparation of Mesoporous TiO_2 Layers. Journal of The Electrochemical Society 2004;151(11):A1767-A73.

45. Jarernboon W, Pimanpang S, Maensiri S, Swatsitang E, Amornkitbamrung V. Optimization of titanium dioxide film prepared by electrophoretic deposition for dye-sensitized solar cell application. Thin Solid Films 2009;517(16):4663-67.

46. Yin X, Liu X, Wang L, Liu B. Electrophoretic deposition of ZnO photoanode for plastic dye-sensitized solar cells. Electrochemistry Communications 2010;12(9):1241-44.

47. Chen SG, Chappel S, Diamant Y, Zaban A. Preparation of Nb_2O_5 Coated TiO_2 Nanoporous Electrodes and Their Application in Dye-Sensitized Solar Cells. Chemistry of Materials 2001;13(12):4629-34.

48. Ito S, Liska P, Comte P, Charvet R, Pechy P, Bach U, et al. Control of dark current in photoelectrochemical (TiO_2/I^--I_3^-) and dye-sensitized solar cells. Chemical Communications 2005(34):4351-53.

49. Yu H, Zhang S, Zhao H, Will G, Liu P. An efficient and low-cost TiO_2 compact layer for performance improvement of dye-sensitized solar cells. Electrochimica Acta 2009;54(4):1319-24.

50. Zaban A, Greenshtein M, Bisquert J. Determination of the Electron Lifetime in Nanocrystalline Dye Solar Cells by Open-Circuit Voltage Decay Measurements. ChemPhysChem 2003;4(8):859-64.

51. Wang Q, Moser J-E, Gratzel M. Electrochemical Impedance Spectroscopic Analysis of Dye-Sensitized Solar Cells. The Journal of Physical Chemistry B 2005;109(31):14945-53.

52. Fabregat-Santiago F, Bisquert J, Palomares E, Otero L, Kuang D, Zakeeruddin SM, et al. Correlation between Photovoltaic Performance and Impedance Spectroscopy of Dye-Sensitized Solar Cells Based on Ionic Liquids. The Journal of Physical Chemistry C 2007;111(17):6550-60.

53. Fabregat-Santiago F, Bisquert J, Garcia-Belmonte G, Boschloo G, Hagfeldt A. Influence of electrolyte in transport and recombination in dye-sensitized solar cells studied by impedance spectroscopy. Solar Energy Materials and Solar Cells 2005;87(1-4):117-31.

54. González-Pedro V, Xu X, Mora-Seró In, Bisquert J. Modeling High-Efficiency Quantum Dot Sensitized Solar Cells. ACS Nano 2010;4(10):5783-90.

55. Fabregat-Santiago F, Garcia-Belmonte G, Mora-Sero I, Bisquert J. Characterization of nanostructured hybrid and organic solar cells by

impedance spectroscopy. Physical Chemistry Chemical Physics 2011;13(20):9083-118.

56. Samadpour M, Boix PP, Giménez S, Iraji Zad A, Taghavinia N, Mora-Seró In, et al. Fluorine Treatment of TiO_2 for Enhancing Quantum Dot Sensitized Solar Cell Performance. The Journal of Physical Chemistry C 2011;115(29):14400-07.

57. Braga A, Giménez S, Concina I, Vomiero A, Mora-Seró In. Panchromatic Sensitized Solar Cells Based on Metal Sulfide Quantum Dots Grown Directly on Nanostructured TiO_2 Electrodes. The Journal of Physical Chemistry Letters 2011;2(5):454-60.

58. Barea EM, Shalom M, Giménez S, Hod I, Mora-Seró In, Zaban A, et al. Design of Injection and Recombination in Quantum Dot Sensitized Solar Cells. Journal of the American Chemical Society 2010;132(19):6834-39.

59. Fan K, Peng T, Chai B, Chen J, Dai K. Fabrication and photoelectrochemical properties of TiO_2 films on Ti substrate for flexible dye-sensitized solar cells. Electrochimica Acta 2010;55(18):5239-44.

Chapter 5. Electrophoretically self-assembled mixed metal oxide-TiO_2 nano-composite film structures for photoelectrochemical energy conversion: Probing of charge recombination and electron transport resistances

In chapter 5, we decided to expand our study by preparing three nanoscale-mixed (TiO_2-MO_x, where M=Al, Mg, Zn) composite films by EPD and probe their charge recombination and electron transport properties in order to relate photoanode composite structure to DSSC performance. The island-like metal oxide nanodeposits onto the TiO_2 particle network of the photoanode are characterized both physically and electrochemically in an effort to identify critical performance-controlling factors that allow for effective interfacial charge recombination resistance without compromising photoelectron generation and transport. This Chapter has been published in: N. Parsi Benehkohal, G.P. Demopoulos, *Journal of Power Sources 240 (2013) 667-675.*

5.1. Abstract

Mixed nano scale titania/metal oxide composite films, instead of the common bi-layer configuration, are prepared via the coupling of Electrophoretic Deposition (EPD) with simultaneous electrolytic deposition of hydrous metal oxides, namely ZnO, MgO and Al_2O_3. The nanocomposite films are built into dye-sensitized solar cell (DSSC) photoanodes and their interfacial charge recombination and electronic resistances are investigated. EPD was conducted at low DC voltage using a P25 nanotitania-isopropanol (5 vol.%) aqueous suspension. The nano hydrous oxides were found to co-deposit uniformly within the TiO_2 film (forming island-like nanodeposits) at approximately 1-3wt% content significantly increasing film adhesion. Photoelectrochemical analysis via Electrochemical Impedance Spectroscopy (EIS) and Open Circuit Voltage Decay (OCVD) techniques found, among the three composite films, the TiO_2-Al_2O_3 electrode to exhibit the highest charge recombination resistance at the TiO_2/electrolyte interface (R_{rec}) having as consequence an increase in resulting V_{OC}. However, its conversion efficiency (4.14%) was the lowest because it suffered from very high electron transport resistance (R_t) in the TiO_2 network. By comparison, the TiO_2-MgO film resulted in 5.40 % conversion efficiency and the TiO_2-ZnO film in 5.85% efficiency-both exhibiting significantly lower R_t resistance. The obtained results point to the need for simultaneous optimization of the nanocomposite TiO_2/metal oxide film structure that delivers high interfacial charge recombination resistance while maintaining low the overall electron transport resistance.

5.2. Introduction

The dye-sensitized solar cell (DSSC) is a unique photoelectrochemical energy conversion device, which since its first introduction in 1991 [1] has attracted tremendous R&D attention. The DSSC is typically composed of a mesoporous nanocrystalline TiO_2 film covered by a monolayer of dye molecules, electrolyte,

and counter electrode. The structure of TiO_2 photoanode provides a large surface area that enables abundant dye loading on the surface to maximize the amount of photogenerated charge. In addition to efficient light harvesting, a large electron diffusion length in TiO_2 photoanode is necessary to obtain good collection efficiency. It is noted that unhindered charge transport in the TiO_2 network accompanied by minimized interfacial charge recombination can lead to the large diffusion length.

There have been intensive studies on a range of fabrication procedures to modify the TiO_2 photoelectrode by incorporating different composite films in order to enhance the cell conversion efficiency. Some studies constructed the composite photoanode based on a mixture of nanoparticles with different size, shape such as, nanotube and nanowire, which resulted in enhanced conversion efficiency due to the facile electron transport as well as light scattering [2-4]. Moreover, different metal oxides have been investigated as scattering layer on top of the transparent TiO_2 film such as ZrO_2 [5] and Al_2O_3[6]. Another approach in fabrication of composite photoanodes is the coating of the transparent TiO_2 film with a thin layer of another metal oxide (a type of core-shell configuration applied to the whole film as opposed the individual particles). This approach has been reported to enhance the cell performance of DSSCs by retarding interfacial recombination. As overcoat materials, different metal oxides with higher conduction band (CB) edges, e.g., MgO, ZnO, Nb_2O_5, Al_2O_3, SiO_2, and ZrO_2, are selected in order to minimize the back transfer of photo injected electrons through the TiO_2/dye/electrolyte interface and, hence, improve the V_{OC} and subsequently cell efficiency [7-17]. Furthermore, overcoating with different metal hydroxides such as $Mg(OH)_2$, $Zn(OH)_2$, $Al(OH)_3$, and $La(OH)_3$ prepared by electrodeposition has also been reported [18-19]. It is worth noting that different metal hydroxides with more negative CB compared to that of TiO_2 (-4.21 *eV* vs. vacuum scale [20]) were also applied as a blocking TiO_2 layer at the FTO/TiO_2 interface in order to decrease electron leakage from the substrate to electrolyte [21-23].

In the present work, given that the majority of previous works have focused on the core-shell (overcoat) composite structure, we have decided to fabricate and study the photovoltaic behaviour of an alternative self-assembled co-deposited mixed metal oxide film. We call this film geometry, hybrid or mixed composite structure. There are a few previous studies with which the new mixed composite structure can be related. Thus Chou et al. [24] reported the fabrication of a TiO_2/NiO mixed composite film by mixing the Ni powder with TiO_2 particles, and depositing it on FTO-glass substrate via the spin coating process; the cell employing the composite structure yielded a better conversion efficiency (η ~3.80%) than that of the conventional TiO_2 film-based DSSC (3.27%). This improvement was attributed to the blocking effect of the NiO particles. Moreover, Niu et al.[25] demonstrated that mixed TiO_2-SiO_2 composite electrodes led to pronounced increase in η from ~5.8% (bare TiO_2) to ~8.4%. This increase was explained in terms of the favourable effect SiO_2 particles had on the dispersion of TiO_2, as well as on its role as blocking layer against charge recombination. However, Chappel et al. [26] claimed that the core-shell film structure is preferable as they argued the metal oxide (usually with more negative CB compared to TiO_2; distributed in the entire film of the mixed structure) will act as energy barriers to photo injected electrons diffusing toward the current collector. However, this loss in charge transport depends on how far the CB position of the second metal oxide is located compared to TiO_2. In addition, in the core-shell (overcoat) film structure, dye molecules are adsorbed directly onto the co-deposited shell and not TiO_2. As a result, not only the amount of dye loading can be affected depending on shell's surface properties (IEP-iso electric point) [15], but also owing to the higher CB edge of the shell oxide, electron injection into TiO_2 can be hindered in agreement to [10, 19, 27]. This issue motivated us to investigate the photovoltaic properties of a hybrid/mixed metal oxide nanodeposit configuration that allows for effective interfacial charge recombination resistance without compromising photoelectron generation and injection achieved by direct dye loading on uncoated areas of TiO_2 surface.

Recently, we showed a significant improvement in overall cell efficiency using a nanocomposite TiO_2-ZnO electrode structure as compared to TiO_2 alone [28]. Therefore, we decided to expand our study by considering $Mg(NO_3)_2$ and $AlCl_3$ in addition to $Zn(NO_3)_2$ as charging agents, prepare three mixed (TiO_2-MO_x) composite films, probe their charge recombination and electron transport properties and relate ultimately film structure to device performance. To this end self-assembled composite electrode films are constructed via our recently developed aqueous suspension-based EPD method [29] and after characterization they are analysed by electrochemical impedance spectroscopy (EIS), incident photon current conversion efficiency (IPCE) and open circuit voltage decay (OCVD) techniques.

5.3. Experimental

5.3.1. Aqueous suspension preparation and EPD procedure

An aqueous suspension was prepared as optimized in our pervious work [29]. The suspension consisted of 5% *v/v* de-ionized water-isopropanol and 5 $g.L^{-1}$ of TiO_2 powder (AEROXIDE® TiO_2 P25, Evonic). In addition, 10^{-3} M of 3 different salts namely, $Zn(NO_3)_2$, $Mg(NO_3)_2$, and $AlCl_3$ were added act as charging and binder (upon electrolytic deposition) agents. The suspension was first mixed for 75 minutes with a magnetic stirrer and after for 15 minutes with an ultrasonic stirrer prior to EPD. The zeta potential and suspension conductivity were measured with a Malvern Zetasizer Nano ZS (Malvern Instruments) and an Oakton conductivity meter, respectively. In order to perform EPD, constant current density (0.1-0.3 $mA.cm^{-2}$) was applied between a stainless steel sheet (anode) and a fluorine-doped tin-oxide conducting glass substrate (FTO-Glass, 7 $\Omega.cm^{-2}$, Nippon Sheet Glass, Japan). This current density range was used in order to minimize water decomposition by applying low voltage (~2.2-4.2 *V*) between two electrodes [29]. The deposition area of the electrode was 5 cm^2. The distance between the two electrodes was 2 *cm*. The deposition was performed for different

times over the range of 5-15 min using a Keithley 2400 Source Meter as a power supply. After deposition, the mixed composite films were dried at room temperature and subjected to annealing at 450°C in air for 30 min [30].

5.3.2. Characterization of mixed nano-composite films

The thickness and roughness of the three composite films (no separate scattering layer was applied) were measured using the Dektak 3030 surface profiler system (Veeco Instruments Inc., U.S.A.). The morphology of the TiO_2 films was characterized by a cold-FEG-SEM Hitachi SU-8000. Energy-dispersive X-ray spectroscopy (Oxford, SU-8000 Hitachi) was also employed to determine the chemical species of the composite substrates. High resolutionTransmission Electron Microscopy (HR-TEM) images were obtained using a Philips CM-200 microscope operating at 200 *kV*. X-ray diffraction (XRD) analysis was performed using a Bruker D8 diffractometer equipped with a GADDS 2D detector and Cu *Kα* radiation (λ = 0.15406 *nm*) at a scan rate of 5°/min. X-ray photoelectron spectroscopy (XPS) measurement was performed and collected with a Thermo Scientific KAlpha instrument, using an Al Kα X-ray source at 1486.6 *eV*. Spectra were generated at a perpendicular takeoff angle, using a pass energy of 20 *eV* and steps of 0.1 *eV*. During analysis, the pressure was in the order of ~10^{-10} Torr. Ar^+ ion bombardment with energy of 2 *keV* for 30 *s* was carried out prior to collecting the spectra in order to remove any charging effects from carbon-based contaminants. As an internal reference for the absolute binding energies, the Au ($4f_{7/2}$) peak was used. The experimental spectra were de-convoluted after subtraction of the Shirley background using the *VG* Avantage program. In order to determine the weight percentage of metallic oxide content of the TiO_2 deposited film, the magnesium and zinc were dissolved (24 h) in acidic (2*M* HCl) and aluminum in basic (5*N* NaOH) solution. Then, they were analysed by atomic absorption (AA) using a Varian Atomic Absorption spectrometer.

5.3.3. Cell fabrication and photoelectrochemical measurements

After annealing, the TiO_2-MO_x films were sensitized by immersion into a room temperature 0.5 *mM* ethanol solution of N719 for 48 *h*. The composite films were rinsed with ethanol to remove physisorbed dye molecules. The absorption spectra of dye-loaded films were recorded by UV/vis spectrophotometry (Lambda20, PerkinElmer). As a counter electrode, a Pt layer was prepared by spreading one drop of 5 *mM* H_2PtCl_6 solution (isopropanol), air dry, and then heating at 380 ˚C for 30 min. The working and counter electrodes were assembled into a sandwich-type cell and sealed with a thermoplastic sealant of 30 μm thickness (Surlyn®-30, Dyesol) by hot-pressing, followed by insertion of commercial electrolyte solution (composition: I_3^-/I^-, organic iodide salt, pyridine derivative, acetonitrile and valeronitrile; EL-HPE; Dyesol) through a hole on the Pt electrode.

Current-voltage (*J*-*V*) curves were recorded using a solar simulator of class ABA (*PV* Measurements Inc., Model *IV* 10) under illumination of uniform light approximating 100 $mW.cm^{-2}$ (AM 1.5 solar emission) provided by a Xenon lamp. The light intensity was adjusted with a Si reference cell. Duplicate measurements with each type of DSSC were made to ensure reproducible results. The IPCE measurements were performed with a *PV* Measurements Inc. Quantum Efficiency system, model QEX10, using a 150 *W* Xe lamp coupled with a slit monochromator. The intensity of incident monochromatic light was calibrated with a Si photodiode. The electrochemical impedance spectra (EIS) and open-circuit voltage decay (OCVD) analysis were measured by using a VSP-potentiostat system (BioLogic). EIS were carried out under 100 $mW.cm^{-2}$ illumination, applying a 10 *mV* AC signal and scanning in a frequency range between 400 *kHz* and 1 *Hz* at different forward applied bias. The EIS data were analyzed with the Z-View software. OCVD analysis [31-33] was carried out to provide detailed curves of electron lifetime (τ) versus open circuit voltage (V_{OC}). In this measurement, cells were illuminated and the decay of V_{OC} was studied as a function of time after the switch-off of the light.

5.4. Results and discussion

5.4.1. Characterization of aqueous suspension and the nanocomposite films

As described before, the same 10^{-3} M concentration of three different salts, namely $AlCl_3$, $Zn(NO_3)_2$, and $Mg(NO_3)_2$, was added to the 5% *v/v* water-isopropanol mixture. As indicated in Table 0-1, $AlCl_3$ provided the most stable suspension verified by the highest zeta potential at 35 *mV*. Despite, however the higher zeta potential that is considered advantageous for EPD, the higher suspension conductivity is not desirable since the free ions tend to carry the bulk of the charge and not the charged particles. On the other hand, $Mg(NO_3)_2$ resulted in the lowest zeta potential and consequently least stable suspension probably due to its lower tendency to be specifically adsorbed on the surface of TiO_2 particles, however the suspension was still stable enough against sedimentation for EPD to take place.

Table 0-1: Properties of different suspensions and deposited mixed composite films

Charging agent	*Zeta Potential (mV)*	*Suspension pH*	*Suspension Conductivity ($10^{-6}S.cm^{-1}$)*	*Applied current density for EPD ($mA.cm^{-2}$) – Applied Voltage (V)*	*Film roughness after annealing (µm)*	*Film composition after annealing*	*Metal oxide film content (% Wt.)*
$AlCl_3$	*35±1.0*	*3.3*	395	0.3 (2.6-3.7 V)	0.64 ± 0.10	TiO_2-Al_2O_3	1.66 ± 0.03
$Zn(NO_3)_2$	*31±3.0*	*4.2*	213	0.1 (2.2-3.2 V)	0.45± 0.16	TiO_2-ZnO	2.39 ± 0.09
$Mg(NO_3)_2$	*20±1.5*	*4.2*	216	0.3 (3.5-4.2 V)	1.34± 0.30	TiO_2-MgO	1.07 ± 0.01

Constant current density EPD was performed at 0.1 $mA.cm^{-2}$ for the suspension containing $Zn(NO_3)_2$ and at 0.3 $mA.cm^{-2}$ for the other two suspensions. These values were determined experimentally to be the highest possible current density that will allow deposition of continuous and uniform films at a potential below the threshold of water decomposition. The present system does not rely on very high applied voltage that is commonly used in organic media to ensure film adhesion but rather on co-deposition of hydrous metal oxide [29].

As can be deduced from the SEM images shown in Figure 0-1, EPD has led to the formation of robust films. It is evident that the TiO_2-ZnO and TiO_2-Al_2O_3 films exhibit superior quality and uniformity compared to the TiO_2-MgO film. This observation is in agreement with the roughness values measured by surface profilometry (Table 0-1). Apparently the lower zeta potential of the $Mg(NO_3)_2$ suspension caused formation of large size aggregates and consequently rougher surface. Moreover, the high magnification SEM images of these films shown in Figure 0-1(d), (e), and (f) provide clear evidence of a well developed mesoporous structure, which is required for efficient dye loading and electrolyte diffusion in DSSC application.

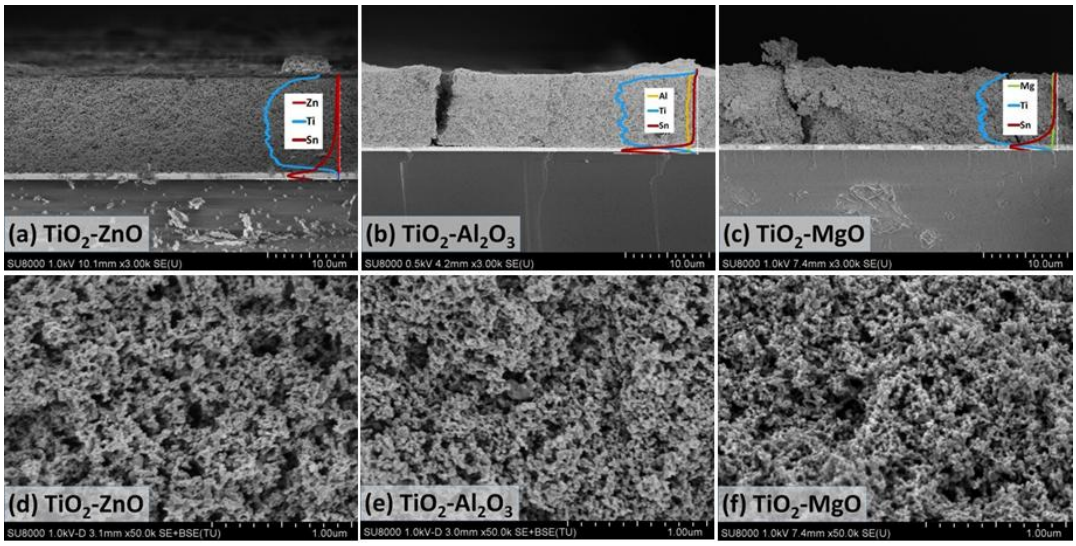

Figure 0-1. (a), (b), and (c) Cross section SEM images of annealed composite films. (c), (d), and (e) high magnification top-view film images. Insets in (a), (b), and (c) show the EDS line scan of the film cross section.

The deposition mechanism of a mixed TiO_2-ZnO composite film was described in detail in our pervious study [29]. In short, during EPD due to cathodic reduction of H^+ and nitrate ions, the local pH increases leading to electrolytic deposition of hydrous metal oxide that acts as binder for the physically deposited TiO_2 particles, hence promoting the building of an adhesive film. Chemical

analysis of the deposited films (shown in Table 0-1), as well as EDS analysis performed on the film cross sections (shown in Figure 0-1), confirmed the uniform co-deposition of zinc, magnesium and aluminum oxide at an amount less than 3 %, independent of the deposition time.

In order to further investigate the mode of metal oxide co-deposition during EPD of TiO_2, elemental maps of some particles removed from the TiO_2-ZnO film were examined at very high magnification (Figure 0-2). As it can be seen, zinc was deposited on the surface of TiO_2 particles uniformly as nanodots rather than as a continuous shell, apparently due to its small quantity. Furthermore, EDS spot analysis on some particles from the same film (Figure 0-2 (e)) confirmed that zinc oxide was present in various spots of the particle surface (e.g. points 1 and 3) but not on other spots (e.g. point 2). According to the XRD results (refer to Figure 0-9 in supporting information), all three annealed composite films showed only the mixed phase TiO_2 (anatase and rutile, since the commercial TiO_2 powder (P25) used in our work is composed of anatase and rutile [34]) and FTO glass. ZnO, Al_2O_3, and MgO were not detected by XRD most likely due to their small quantity (<3%) as also noted elsewhere [35-36]. It is notable that there was no sign of Zn^{2+}, Mg^{2+}, and Al^{3+} ions substitution into the TiO_2 lattice as deduced from the lack of any XRD peak shift [37-38]. The absence of substitution was also deduced from High-resolution TEM analysis as per image presented in Figure 0-3, where the characteristic lattice spacing of undoped anatase (0.352 nm) for (101) plane [39] is present. The same HR-TEM image of Figure 0-3 further provides evidence of partial coating of the TiO_2 surface by a nanodeposit (~1 nm thick rim). Therefore, ZnO, Al_2O_3, and MgO crystallites are considered to have deposited on the surface of TiO_2 nanoparticles.

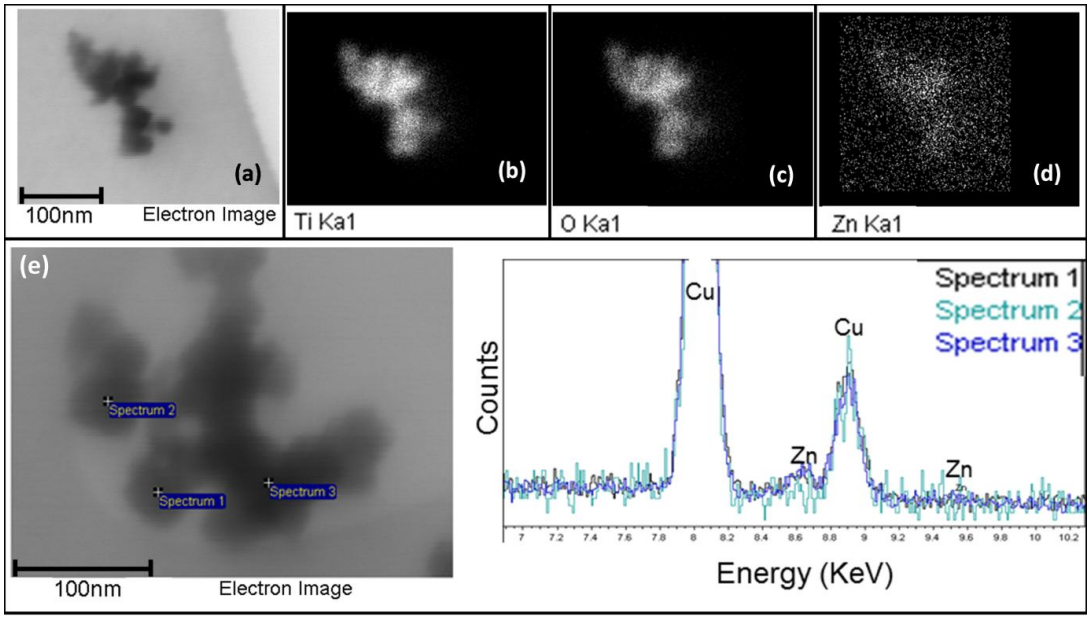

Figure 0-2. Elemental maps of part of TiO_2–ZnO film in high magnification. (a) STEM image of nanoparticles of TiO_2–ZnO composite film. (b), (c), (d) Elemental maps displaying Ti, O and Zn distribution, and (e) EDS spot analysis on some particles removed from the TiO_2–ZnO film

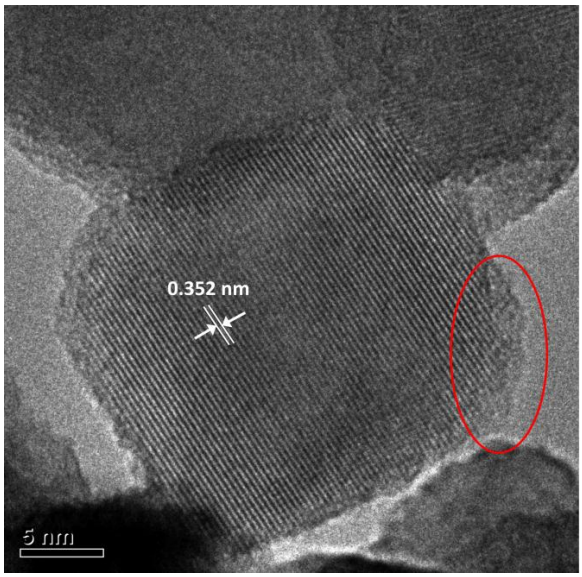

Figure 0-3. HR-TEM image of TiO_2–ZnO composite film showing a single TiO_2 nanoparticle (characteristic lattice spacing of 0.35 nm corresponding to (101) planes in anatase) that appears partially coated with ZnO (~1 nm surface deposit).

Finally, in order to positively substantiate the presence of co-deposited metal oxides XPS analysis was performed and presented in Figure 0-4. The XPS high-resolution spectra exhibited peaks at 1021.93, 74.96, and 50.6 *eV* attributed to Zn $2p_{3/2}$, Al 2p, and Mg 2p states, which are characteristic of ZnO [40], Al_2O_3 [41-42], and MgO [43-45], respectively.

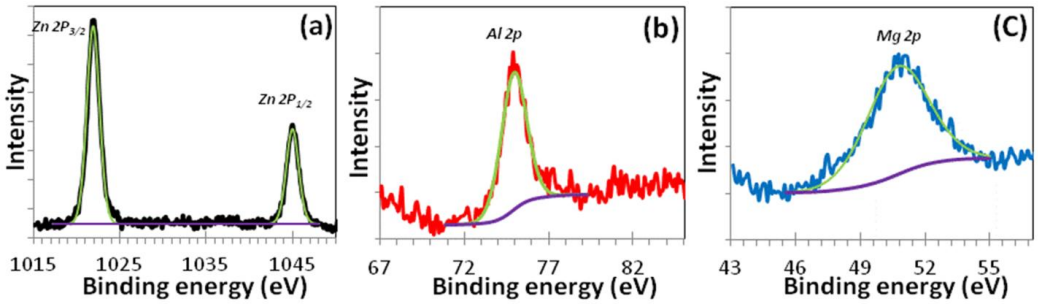

Figure 0-4. High resolution XPS spectra of (a) Zn 2p region, (b) Al 2p region, and (c) Mg 2p region for annealed TiO_2–ZnO, TiO_2–Al_2O_3, and TiO_2–MgO films, respectively.

5.4.2. Photoelectrochemical characterization

Before assembling the DSSC, UV-vis absorption spectra for dye-loaded films were measured and presented in Figure 0-5 (a). The differences in absorption spectra of these films are negligible indicating that the co-deposited oxides did not alter the dye-adsorption properties of TiO_2 (P25)- the main component of the sensitized film. Eventually, DSSCs were assembled using these three mixed composite films as photoanodes with similar thickness of ca.11.5 μm *J-V* measurements made on the cells, shown in Figure 0-5 (b) and Table 0-2, indicated that the TiO_2-ZnO photoanode produced the highest short circuit current density (J_{sc}) and conversion efficiency (η) almost 40% higher than that of the TiO_2-Al_2O_3 film that showed the lowest performance.

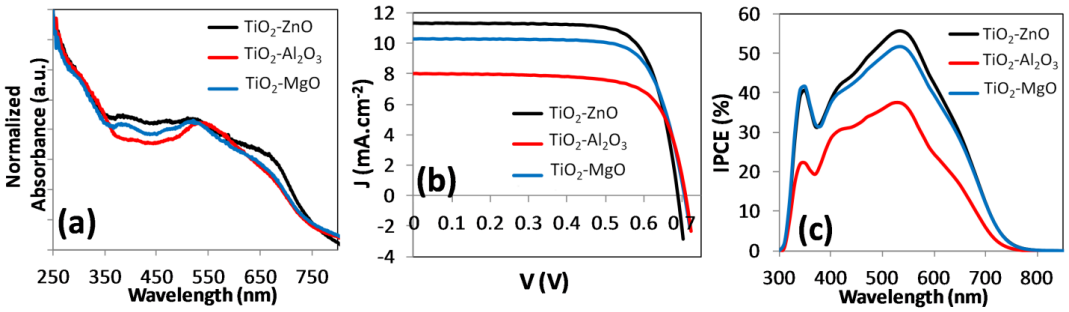

Figure 0-5. (a) Absorption spectra of dye-covered nanocomposite film, (b) I–V curves and (c) IPCE of various DSSCs prepared by different nanocomposite photoanodes.

Measurements of IPCE, which is defined as the number of electrons generated by light in the external circuit divided by the number of incident photons, of the three composite photoanodes are shown in Figure 0-5 (c). The maximum IPCE value for the three composite films at ~530 nm decreases from 55.7, to 51.6, to 37.6% in direct correspondence with the observed drop of J_{sc} from 11.3, to 10.3, to 8.03 $mA.cm^{-2}$ for TiO_2-ZnO, TiO_2-MgO, and TiO_2- Al_2O_3, respectively.

Table 0-2. Photovoltaic parameters of different DCCSs.

Film	J_{sc} *(mA.cm^{-2})*	V_{OC} *(V)*	*Fill factor*	η_{max} *(%)*	$\eta_{average}$ *(%)*
TiO_2 - ZnO	11.3	689	0.75	5.86	5.57±0.45
TiO_2 - MgO	10.3	706	0.74	5.40	5.36±0.05
TiO_2 - Al_2O_3	8.03	710	0.72	4.14	3.42±0.63

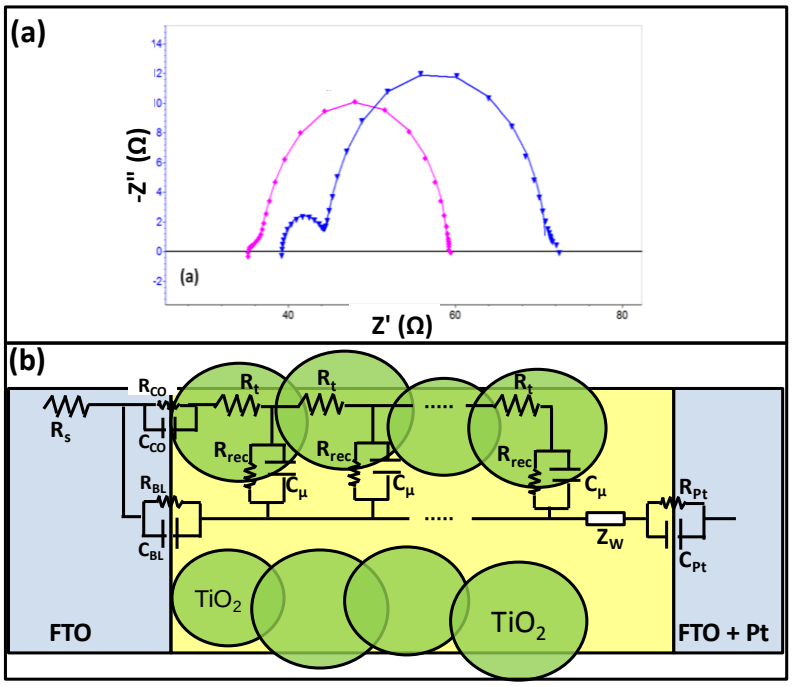

Figure 0-6. (a) Typical Nyquist plots of DSSC based on TiO_2–ZnO film and measured under 1 sun illumination and the *Voc* condition. Lines represent corresponding fit results. (b) General transmission line model of DSSCs [47]. The (R_{rec}) is the charge recombination resistance at the TiO_2/dye/electrolyte interface; (C_μ) is the chemical capacitance of the TiO_2 film; (R_t) is the transport resistance of electrons in TiO_2 film; Z_W is the Warburg element showing the Nernst diffusion of I_3^- in electrolyte; (R_{Pt}) and (C_{Pt}) are the charge-transfer resistance and double-layer capacitance at the platinized counter electrode; (R_{BL}) and (C_{BL}) are the charge-transfer resistance and the corresponding double-layer capacitance at exposed FTO/electrolyte interface; (R_{CO}) and (C_{CO}) are the resistance and the capacitance at FTO/TiO_2 contact; R_s is the series resistance, including the sheet resistance of FTO glass and contact resistance of the cell.

Electrochemical impedance spectroscopy (EIS) is regarded as a powerful tool for investigating the electron transport and kinetics of interfacial charge transfer processes in DSSCs [46]. A typical EIS spectrum for a DSSC exhibits three semicircles in the Nyquist plot (see Figure 0-6 (a)). The left (high frequency) arc represents *(R_{CE})*, which consists of the charge transfer process at the Pt counter electrode/electrolyte *(R_{Pt})* and FTO/ TiO_2 interfaces (R_{CO}); the central arc is related to charge transport resistance in TiO_2 film (R_t), recombination at the

TiO_2/dye/electrolyte interfaces (R_{rec}) and the chemical capacitance (C_μ); and the third arc is associated with electrolyte diffusion impedance (Z_w)[47]. The third arc is not discernible here (Figure 0-6 (a)) because of overlap with the middle-frequency [48] probably due to the use of high performance commercial electrolyte with a small diffusion resistance. In this study we carried out EIS analysis at varying applied voltage in order to verify whether there is a shift in the CB of TiO_2 (as a result of the metal oxide co-deposition) thus allowing for interpretation of R_{rec} differences. This CB displacement is observable from the C_μ shift as reported elsewhere [49]. All mentioned parameters were extracted from EIS measurements by employing the transmission model proposed by Fabregat-Santiago et al. [49-51] (see Figure 0-6 (b)) and plotted against the voltage drop at the sensitized electrode, V_F. The latter was obtained by subtracting the voltage drop of the series resistance (V_{series}) from the applied potential (V_{app}): $V_F = V_{app} - V_{series}$ [49]. V_F is proportional to the rise of the Fermi level of electrons in TiO_2, $V_F = (E_{Fn}-E_{F0})/q$, where q is the positive elementary charge and E_{Fn} and E_{F0} are the electron Fermi level and the electron Fermi level at equilibrium, respectively. As shown in Figure 0-7 (b), the C_μ of the three composite films did not shift indicating similar CB position.

Moreover, knowing the value of L (film thickness), R_{rec} and R_t, makes it possible to calculate important electron parameter called effective diffusion length (L_n), using the equation (0-1):

$$L_n = L\sqrt{R_{rec} / R_t} \quad (0\text{-}1) \quad [52]$$

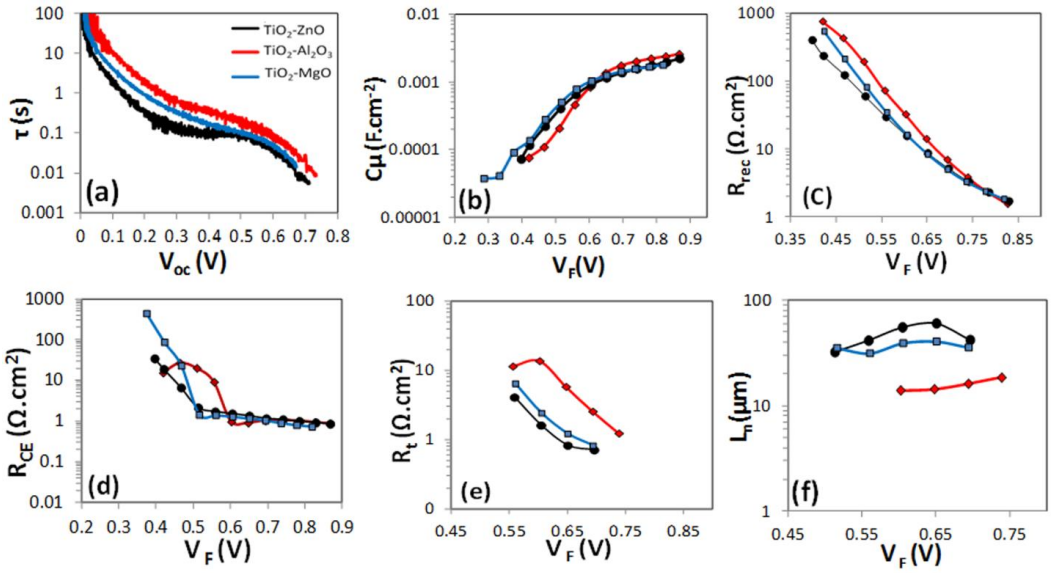

Figure 0-7. (a) Electron lifetime (τ) as a function of *Voc* for DSSCs based on different nano-composite photoanodes obtained from OCVD measurement. (b), (c), (d), (e), and (f) Impedance parameters of the various electrodes as function of the voltage drop, V_F (after series resistance correction).

We further probed our cells via the use of OCVD, a complementary to EIS technique that provides very detailed curves of electron lifetime (τ_n) in DSSC devices as a measure of recombination kinetics [53]. It monitors the decay of photovoltage (V_{OC}) after turning off the illumination [33]. The photovoltage decay reflects the decrease of electron concentration at the TiO_2, which is mainly caused by charge recombination. As reported before [54], the electron lifetime (τ) can be derived from the rate of V_{OC} decay according to equation (0-2):

$$\tau = -\frac{k_B T}{e}\left(\frac{dV_{OC}}{dt}\right)^{-1} \qquad (0\text{-}2)$$

where k_B is the Boltzmann constant, T is the temperature, and e is the electron charge. The calculated response times τ as a function of V_{OC} for the three different

DSSCs are displayed in Figure 0-7 (a) indicating highest and lowest electron lifetime for TiO_2-Al_2O_3 and TiO_2-ZnO photoanodes, respectively.

5.4.3. Discussion

Now, the origin of performance differences in the three composite photoanodes will be discussed. As shown in Table 0-2, the V_{OC} was slightly improved from TiO_2-ZnO to TiO_2-MgO and TiO_2-Al_2O_3. As we discussed in our pervious study [28] and in agreement with Doh et al. [55] V_{OC} improvement can result from retardation of interfacial charge recombination (originating from ZnO, Al_2O_3, and MgO [22]) and/or from possible upward shift of the CB edge position of TiO_2 due to development of a dipole at the interface of TiO_2/metal oxide [56-58]. However, since similar C_μ values were determined (Figure 0-7 (b)) the CB edge for all 3 composite photoanodes, by extension is the same leaving retardation of charge recombination as the origin of the observed V_{OC} increase. According to Figure 0-7 (c), Al_2O_3 presented the highest blocking ability for interfacial charge recombination because of its highest R_{rec}, which also resulted in the highest electron lifetime as determined from the OCVD measurements (Figure 0-7 (a)). The blocking ability of Al_2O_3 is most likely due to its higher CB edge position (-1.31 *eV* vs. vacuum level) compared to MgO (-1.41 *eV* vs. vacuum level) and ZnO (-4.19 *eV* vs. vacuum level [15, 20]). It is notable that the mechanism of charge transfer determining R_{rec} is via direct transfer from the TiO_2 CB [31]. However, electrons may recombine not only from the CB but also from localized intraband states as well as surface states in the band gap [50, 59]. Therefore, it is also interesting to probe the region of lower Fermi levels [54].Thus, the OCVD technique was employed as it allows us to monitor the kinetics of recombination in the domain of low photovoltages [33, 54]. It is apparent from the data of Figure 0-7(a) that the composite films containing Al_2O_3 and MgO exhibited more linear electron lifetime curves at lower voltage (below ~0.5 *V*) than the film containing ZnO. This means that Al_2O_3 and MgO offered better passivation of surface trap states in

comparison to ZnO, a finding in good agreement with [31] where Al_2O_3 was employed as an overcoat.

However, as shown in Table 0-2, TiO_2-Al_2O_3 photoanode yielded rather poor performance in terms of J_{sc} and η despite its higher charge recombination resistance. The observed lower J_{sc} and the corresponding lower IPCE of the TiO_2-Al_2O_3 photoanode may be linked to a decrease in injection yield and/or charge collection efficiency. Since all three photoanodes had the same CB position of TiO_2 as verified by EIS (Figure 0-7 (b)), and not a significant difference in the amount of dye loading as verified by the UV-vis absorption spectra (Figure 0-5 (a)) charge injection efficiency from the excited dye to TiO_2 must have been the same for all of them. Hence, it can be concluded that the collection/extraction efficiency of the injected electrons must be held responsible for the observed poor performance of the TiO_2-Al_2O_3 electrode. The effective diffusion length (L_n) of the photoinjected electron in a TiO_2 film is very well known to be a good indicator for charge extraction [60]. According to Figure 0-7 (f), the L_n in TiO_2-Al_2O_3 is much shorter than in the other photoanodes resulting in the lowest charge extraction, and consequently lowest J_{sc} and IPCE. This can be explained on the basis of Al_2O_3's high CB position as schematically described in Figure 0-8. It is postulated that photo injected electrons cannot transport through the co-deposited metal oxide (Al_2O_3) as its high CB acts as energy barrier in the contact point of two adjacent TiO_2 particles. As a result R_t increases with the consequence of a shorter L_n. By comparison to MgO that has almost the same CB, it is possible that the blocking effect of Al_2O_3 was more drastic due to its ~55% higher amount (1.66 Wt% vs. 1.07 Wt% for MgO) that apparently resulted in a more insulating nanocoating in the TiO_2-Al_2O_3 electrode.

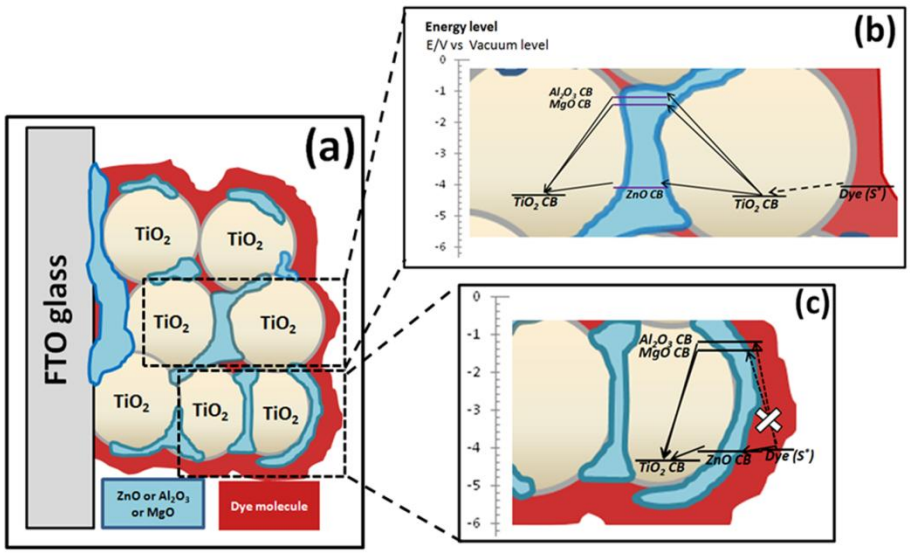

Figure 0-8. (a) Schematic view of the mixed composite structure; (b) electron transfer inside the composite film in the case of the dye molecules been attached directly onto TiO_2 particles; and (c) electron transfer inside the composite film in the case of the dye molecules been attached to the co-deposited metal oxide having higher CB band edge compared to that of TiO_2.

As mentioned above, in the mixed metal oxide composite structure, the co-deposited oxides do not form complete shell around the TiO_2 particles but give an island-like deposit on the TiO_2 surface similar to the schematic presented in Figure 0-8. This structure can be considered advantageous in comparison to the core-shell structure in terms of sensitization and charge injection efficiency. In the latter structure, dye molecules are adsorbed directly onto the co-deposited shell and not TiO_2. As a result, owing to the higher CB edge of the co-deposited oxide, electron injection into TiO_2 (Figure 0-8 (c)) is hindered in agreement to [10, 19, 27]. In contrast the island-like metal oxide co-deposition pattern makes some part of TiO_2 surface available for the direct dye adsorption and consequently direct charge injection into TiO_2 CB. Proper selection of the right co-deposited metal oxide that can match the electronic properties of TiO_2, therefore, becomes critical in electrophoretically forming electrode structures with superior performance properties. In this regard ZnO is the co-deposited metal oxide of choice. Thus, a

high conversion efficiency of 6.44 % was obtained via multi-layer (by repeated cycles of EPD) construction of the transparent TiO_2-ZnO film (8 layers) with optimum total thickness of 19 μm.

5.5. Conclusion

Three different mixed oxide nanocomposite photoeletrodes, namely TiO_2-ZnO, TiO_2-Al_2O_3 and TiO_2-MgO were fabricated by low DC voltage EPD using a P25 nanotitania-isopropanol (5 vol.%) aqueous suspension. Co-deposition of secondary oxides was accomplished via in-situ cathodic electrolytic deposition of Zn, Mg, and Al hydroxides that acted as binders and finally converted to the oxide form upon annealing at 450 ˚C. Co-deposits of all three nano oxides were uniformly distributed (~1-3 wt%) within the film in island-like pattern on TiO_2 particle surfaces. As a result dye loading on the TiO_2 surface was not adversely affected. However, photovoltaic behaviour was impacted in different ways by the electronic properties of the co-deposited metal oxide. Thus among the three composite photoelectrodes, TiO_2-Al_2O_3 showed the highest charge recombination resistance at the TiO_2/electrolyte interface (R_{rec}) resulting in the highest electron lifetime and, consequently slightly higher V_{OC}. However, it showed the lowest conversion efficiency of 4.14% mainly due to the highest charge transport resistance (R_t) of photo injected electrons in the TiO_2 network arising from Al_2O_3's high CB that acts as energy barrier compounded with a more insulating nanocoating. The TiO_2-MgO film showed 5.40 % conversion efficiency due to the lower R_t and longer L_n compared to TiO_2-Al_2O_3. On the other hand, the TiO_2-ZnO device showed the highest conversion efficiency (5.85%) and current density (11.3 $mA.cm^{-2}$) corresponding to the lowest R_t. The obtained results point to the need for simultaneous optimization of the nanocomposite TiO_2/metal oxide film structure that delivers high interfacial charge recombination resistance while maintaining low the overall electron transport resistance.

5.6. Acknowledgments

This research is supported via a NSERC strategic project grant and sponsored by CIS Solar, Hydro-Quebec, Versatilis Inc and Targray Technology International. The authors are thankful to Professor Raynald Gauvin and Nicolas Brodusch for using the SEM Hitachi SU-8000. Furthermore, Professor N. Tufenkji is thanked for permission to use the Zetasizer in her laboratory.

5.7. Supporting Information

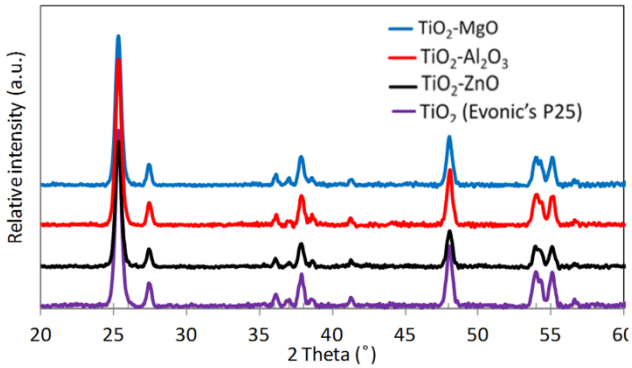

Figure 0-9. XRD patterns of different nano-composite films after annealing compared to Evonic's P25's pattern

5.8. References

1. O'Regan B, Grätzel M. A low-cost, high-efficiency solar cell based on dye-sensitized colloidal TiO_2 films. Nature 1991;353:737 - 40.

2. Yu J, Li Q, Shu Z. Dye-sensitized solar cells based on double-layered TiO_2 composite films and enhanced photovoltaic performance. Electrochimica Acta 2011;56(18):6293-98.

3. Kim YJ, Lee YH, Lee MH, Kim HJ, Pan JH, Lim GI, et al. Formation of Efficient Dye-Sensitized Solar Cells by Introducing an Interfacial Layer of Long-Range Ordered Mesoporous TiO_2 Thin Film. Langmuir 2008;24(22):13225-30.

4. Chan Y-F, Wang C-C, Chen B-H, Chen C-Y. Dye-sensitized TiO_2 solar cells based on nanocomposite photoanode containing plasma-modified multi-walled carbon nanotubes. Progress in Photovoltaics: Research and Applications 2013;21(1):47-57.

5. Hore S, Vetter C, Kern R, Smit H, Hinsch A. Influence of scattering layers on efficiency of dye-sensitized solar cells. Solar Energy Materials and Solar Cells 2006;90(9):1176-88.

6. Shin K, Jun Y, Moon JH, Park JH. Observation of Positive Effects of Freestanding Scattering Film in Dye-Sensitized Solar Cells. ACS Applied Materials & Interfaces 2009;2(1):288-91.

7. Tennakone K, Bandara J, Bandaranayake PKM, Kumara GRA, Konno A. Enhanced efficiency of a dye-sensitized solar cell made from MgO-coated nanocrystalline SnO_2. Japanese Journal of Applied Physics, Part 2: Letters 2001;40(7 B):L732-L34.

8. Palomares E, Clifford JN, Haque SA, Lutz T, Durrant JR. Slow charge recombination in dye-sensitised solar cells (DSSC) using Al_2O_3 coated nanoporous TiO_2 films. Chemical Communications 2002(14):1464-65.

9. Palomares E, Clifford JN, Haque SA, Lutz T, Durrant JR. Control of Charge Recombination Dynamics in Dye Sensitized Solar Cells by the Use of Conformally Deposited Metal Oxide Blocking Layers. Journal of the American Chemical Society 2002;125(2):475-82.

10. Kay A, Grätzel M. Dye-Sensitized Core−Shell Nanocrystals: Improved Efficiency of Mesoporous Tin Oxide Electrodes Coated with a Thin Layer of an Insulating Oxide. Chemistry of Materials 2002;14(7):2930-35.

11. Kim S-S, Yum J-H, Sung Y-E. Improved performance of a dye-sensitized solar cell using a TiO_2/ZnO/Eosin Y electrode. Solar Energy Materials and Solar Cells 2003;79(4):495-505.

12. Taguchi T, Zhang X-t, Sutanto I, Tokuhiro K-i, Rao TN, Watanabe H, et al. Improving the performance of solid-state dye-sensitized solar cell using MgO-coated TiO_2 nanoporous film. Chemical Communications 2003(19):2480-81.

13. Kumara GRA, Okuya M, Murakami K, Kaneko S, Jayaweera VV, Tennakone K. Dye-sensitized solid-state solar cells made from magnesiumoxide-coated nanocrystalline titanium dioxide films: enhancement of the efficiency. Journal of Photochemistry and Photobiology A: Chemistry 2004;164(1–3):183-85.

14. Jung HS, Lee J-K, Nastasi M, Lee S-W, Kim J-Y, Park J-S, et al. Preparation of Nanoporous MgO-Coated TiO_2 Nanoparticles and Their Application to the Electrode of Dye-Sensitized Solar Cells. Langmuir 2005;21(23):10332-35.

15. Kim J, Lee S, Noh J, Jung H, Hong K. Enhanced photovoltaic properties of overlayer-coated nanocrystalline TiO_2 dye-sensitized solar cells (DSSCs). Journal of Electroceramics 2009;23(2):422-25.

16. Chou C-S, Chou F-C, Kang J-Y. Preparation of ZnO-coated TiO_2 electrodes using dip coating and their applications in dye-sensitized solar cells. Powder Technology 2012;215-216(0):38-45.

17. Chen SG, Chappel S, Diamant Y, Zaban A. Preparation of Nb_2O_5 Coated TiO_2 Nanoporous Electrodes and Their Application in Dye-Sensitized Solar Cells. Chemistry of Materials 2001;13(12):4629-34.

18. Yum J-H, Nakade S, Kim D-Y, Yanagida S. Improved Performance in Dye-Sensitized Solar Cells Employing TiO_2 Photoelectrodes Coated with Metal Hydroxides. The Journal of Physical Chemistry B 2006;110(7):3215-19.

19. Peiris TAN, Senthilarasu S, Wijayantha KGU. Enhanced Performance of Flexible Dye-Sensitized Solar Cells: Electrodeposition of $Mg(OH)_2$ on a Nanocrystalline TiO_2 Electrode. The Journal of Physical Chemistry C 2011;116(1):1211-18.

20. Yong X, Schoonen MAA. The absolute energy positions of conduction and valence bands of selected semiconducting minerals. American Mineralogist 2000;85(3-4):543-56.

21. Xia J, Masaki N, Jiang K, Yanagida S. Sputtered Nb_2O_5 as a Novel Blocking Layer at Conducting Glass/ TiO_2 Interfaces in Dye-Sensitized Ionic Liquid Solar Cells. The Journal of Physical Chemistry C 2007;111(22):8092-97.

22. Liu Y, Sun X, Tai Q, Hu H, Chen B, Huang N, et al. Efficiency enhancement in dye-sensitized solar cells by interfacial modification of conducting glass/mesoporous TiO_2 using a novel ZnO compact blocking film. Journal of Power Sources 2011;196(1):475-81.

23. Noh JH, Lee S, Kim JY, Lee J-K, Han HS, Cho CM, et al. Functional Multilayered Transparent Conducting Oxide Thin Films for Photovoltaic Devices. The Journal of Physical Chemistry C 2008;113(3):1083-87.

24. Chou C-S, Lin Y-J, Yang R-Y, Liu K-H. Preparation of TiO_2/NiO composite particles and their applications in dye-sensitized solar cells. Advanced Powder Technology 2011;22(1):31-42.

25. Niu H, Liu L, Wang H, Zhang S, Ma Q, Mao X, et al. Significant influence of nano-SiO_2 on the performance of dye-sensitized solar cells based on P25. Electrochimica Acta 2012;81(0):246-53.

26. Chappel S, Chen S-G, Zaban A. TiO_2-Coated Nanoporous SnO_2 Electrodes for Dye-Sensitized Solar Cells. Langmuir 2002;18(8):3336-42.

27. Alarcón H, Hedlund M, Johansson EMJ, Rensmo H, Hagfeldt A, Boschloo G. Modification of Nanostructured TiO_2 Electrodes by Electrochemical Al^{3+} Insertion: Effects on Dye-Sensitized Solar Cell Performance. The Journal of Physical Chemistry C 2007;111(35):13267-74.

28. Parsi Benehkohal N, Demopoulos GP. Green Preparation of TiO_2-ZnO Nanocomposite Photoanodes by Aqueous Electrophoretic Deposition. Journal of The Electrochemical Society 2012;159(5):B602-B10.

29. Parsi Benehkohal N, Gomez MA, Gauvin R, Demopoulos GP. Enabling aqueous electrophoretic growth of adherent nanotitania mesoporous films via intrafilm cathodic deposition of hydrous zinc oxide. Electrochimica Acta 2013;87(0):169-79.

30. Lee K, Charbonneau C, Shan G, Demopoulos G, Gauvin R. Nanocrystalline TiO_2 thin film electrodes for dye-sensitized solar cell applications. JOM Journal of the Minerals, Metals and Materials Society 2009;61(4):52-57.

31. Fabregat-Santiago F, Garcia-Canadas J, Palomares E, Clifford JN, Haque SA, Durrant JR, et al. The origin of slow electron recombination processes in dye-sensitized solar cells with alumina barrier coatings. Journal of applied physics 2004;96(11):6903-07.

32. Grinis L, Kotlyar S, Rühle S, Grinblat J, Zaban A. Conformal Nano-Sized Inorganic Coatings on Mesoporous TiO_2 Films for Low-Temperature Dye-

Sensitized Solar Cell Fabrication. Advanced Functional Materials 2010;20(2):282-88.

33. Bisquert J, Zaban A, Greenshtein M, Mora-Seró I. Determination of Rate Constants for Charge Transfer and the Distribution of Semiconductor and Electrolyte Electronic Energy Levels in Dye-Sensitized Solar Cells by Open-Circuit Photovoltage Decay Method. Journal of the American Chemical Society 2004;126(41):13550-59.

34. Erdem B, Hunsicker RA, Simmons GW, Sudol ED, Dimonie VL, El-Aasser MS. XPS and FTIR Surface Characterization of TiO_2 Particles Used in Polymer Encapsulation. Langmuir 2001;17(9):2664-69.

35. Ku Y, Huang Y-H, Chou Y-C. Preparation and characterization of ZnO/ TiO_2 for the photocatalytic reduction of Cr(VI) in aqueous solution. Journal of Molecular Catalysis A: Chemical 2011;342-343:18-22.

36. Zou J-J, Zhu B, Wang L, Zhang X, Mi Z. Zn- and La-modified TiO_2 photocatalysts for the isomerization of norbornadiene to quadricyclane. Journal of Molecular Catalysis A: Chemical 2008;286(1-2):63-69.

37. Wang H, Wu Z, Liu Y, Sheng Z. The characterization of ZnO–anatase–rutile three-component semiconductor and enhanced photocatalytic activity of nitrogen oxides. Journal of Molecular Catalysis A: Chemical 2008;287(1-2):176-81.

38. Wang Z-S, Huang C-H, Huang Y-Y, Hou Y-J, Xie P-H, Zhang B-W, et al. A Highly Efficient Solar Cell Made from a Dye-Modified ZnO-Covered TiO_2 Nanoporous Electrode. Chemistry of Materials 2001;13(2):678-82.

39. Zhang H, Liu P, Li F, Liu H, Wang Y, Zhang S, et al. Facile Fabrication of Anatase TiO_2 Microspheres on Solid Substrates and Surface Crystal Facet

Transformation from {001} to {101}. Chemistry – A European Journal 2011;17(21):5949-57.

40. Dake LS, Baer DR, Zachara JM. Auger parameter measurements of zinc compounds relevant to zinc transport in the environment. Surface and Interface Analysis 1989;14(1-2):71-75.

41. Mullins WM, Averbach BL. Bias-reference X-Ray photoelectron spectroscopy of sapphire and yttrium aluminum garnet crystals. Surface Science 1988;206(1–2):29-40.

42. Di Castro V, Polzonetti G, Contini G, Cozza C, Paponetti B. XPS study of MnO_2 minerals treated by bioleaching. Surface and Interface Analysis 1990;16(1-12):571-74.

43. Altieri S, Tjeng LH, Voogt FC, Hibma T, Sawatzky GA. Reduction of Coulomb and charge-transfer energies in oxide films on metals. Physical Review B 1999;59(4):R2517-R20.

44. Peng XD, Barteau MA. Characterization of oxide layers on Mg(0001) and comparison of H_2O adsorption on surface and bulk oxides. Surface Science 1990;233(3):283-92.

45. Huang HH, Jiang X, Zou Z, Chin WS, Xu GQ, Dai WL, et al. Potassium adsorption and reaction with water on MgO(100). Surface Science 1998;412–413(0):555-61.

46. Wang Q, Moser J-E, Gratzel M. Electrochemical Impedance Spectroscopic Analysis of Dye-Sensitized Solar Cells. The Journal of Physical Chemistry B 2005;109(31):14945-53.

47. Fabregat-Santiago F, Bisquert J, Palomares E, Otero L, Kuang D, Zakeeruddin SM, et al. Correlation between Photovoltaic Performance and

Impedance Spectroscopy of Dye-Sensitized Solar Cells Based on Ionic Liquids. The Journal of Physical Chemistry C 2007;111(17):6550-60.

48. Wang Z-S, Cui Y, Dan-oh Y, Kasada C, Shinpo A, Hara K. Thiophene-Functionalized Coumarin Dye for Efficient Dye-Sensitized Solar Cells: Electron Lifetime Improved by Coadsorption of Deoxycholic Acid. The Journal of Physical Chemistry C 2007;111(19):7224-30.

49. Fabregat-Santiago F, Garcia-Belmonte G, Mora-Sero I, Bisquert J. Characterization of nanostructured hybrid and organic solar cells by impedance spectroscopy. Physical Chemistry Chemical Physics 2011;13(20):9083-118.

50. Fabregat-Santiago F, Bisquert J, Garcia-Belmonte G, Boschloo G, Hagfeldt A. Influence of electrolyte in transport and recombination in dye-sensitized solar cells studied by impedance spectroscopy. Solar Energy Materials and Solar Cells 2005;87(1-4):117-31.

51. González-Pedro V, Xu X, Mora-Seró In, Bisquert J. Modeling High-Efficiency Quantum Dot Sensitized Solar Cells. ACS Nano 2010;4(10):5783-90.

52. Bisquert J, Mora-Seró In. Simulation of Steady-State Characteristics of Dye-Sensitized Solar Cells and the Interpretation of the Diffusion Length. The Journal of Physical Chemistry Letters 2009;1(1):450-56.

53. Bisquert J, Fabregat-Santiago F, Mora-Seró In, Garcia-Belmonte G, Giménez S. Electron Lifetime in Dye-Sensitized Solar Cells: Theory and Interpretation of Measurements. The Journal of Physical Chemistry C 2009;113(40):17278-90.

54. Zaban A, Greenshtein M, Bisquert J. Determination of the Electron Lifetime in Nanocrystalline Dye Solar Cells by Open-Circuit Voltage Decay Measurements. ChemPhysChem 2003;4(8):859-64.

55. Doh J-G, Hong JS, Vittal R, Kang MG, Park N-G, Kim K-J. Enhancement of Photocurrent and Photovoltage of Dye-Sensitized Solar Cells with TiO_2 Film Deposited on Indium Zinc Oxide Substrate. Chemistry of Materials 2003;16(3):493-97.

56. Law M, Greene LE, Radenovic A, Kuykendall T, Liphardt J, Yang P. ZnO−Al_2O_3 and ZnO− TiO_2 Core−Shell Nanowire Dye-Sensitized Solar Cells. The Journal of Physical Chemistry B 2006;110(45):22652-63.

57. Butler MA, Ginley DS. Prediction of Flatband Potentials at Semiconductor-Electrolyte Interfaces from Atomic Electronegativities. Journal of The Electrochemical Society 1978;125(2):228-32.

58. Diamant Y, Chappel S, Chen SG, Melamed O, Zaban A. Core–shell nanoporous electrode for dye sensitized solar cells: the effect of shell characteristics on the electronic properties of the electrode. Coordination Chemistry Reviews 2004;248(13–14):1271-76.

59. Bisquert J. Chemical Diffusion Coefficient of Electrons in Nanostructured Semiconductor Electrodes and Dye-Sensitized Solar Cells. The Journal of Physical Chemistry B 2004;108(7):2323-32.

60. Wang Q, Ito S, Gratzel M, Fabregat-Santiago F, Mora-Sero I, Bisquert J, et al. Characteristics of High Efficiency Dye-Sensitized Solar Cells. The Journal of Physical Chemistry B 2006;110(50):25210-21.

Chapter 6. Green-engineered all-substrate mesoporous TiO_2 thin film photoanodes with superior light harvesting structure and performance

In all previous studies reported in Chapters 3-5, EPD was employed to prepare photoanodes for DSSC application and photoelectrochemical analysis using a commercial available nanotitania powder, P25 (Evonic) with narrow size distribution. This material however is known from other reports in literature to be inferior in DSSC applications in comparison to benchmark nanotitania materials (Dyesol) produced by a combination of sol-gel and hydrothermal processing and formulated into screen-printing pastes. In an effort to (1) fabricate photoanodes by EPD that exhibit record efficiency at par with the benchmark screen printable photoanodes; and (2) to build bi-functional photoanodes via co-deposition of multi-sized TiO_2 particles of different functionality the present work was undertaken. In this regard, environmentally friendly aqueous-synthesized anatase (5–10 nm) nanocrystallites and sub-micrometer-sized "sea urchin"-like rutile (200–500 nm) aggregates are used in a binder-free isopropanol suspension. Upon study and optimization assisted by photoelectrochemical characterization, record-breaking DSSC devices for EPD-built photoanodes are designed. The new EPD procedure is shown to be equally effective for metallic and plastic substrates. A manuscript based on this Chapter was submitted for publication as per following info: N. Parsi Benehkohal and G. P. Demopoulos, Submitted to *Journal of Materials Chemistry A: Materials for energy and sustainability on 13-Aug-2013*.

6.1. Abstract

Electrophoretic deposition (EPD) is employed successfully in a suspension of multi-component and different size and morphology (anatase + rutile) TiO_2 nanoparticulates to engineer a very robust bi-functional electrode structure for dye sensitized solar (DSSC) application with excellent light harvesting and photo electrochemical performance. Aqueous-synthesized anatase (5–10 nm) nanocrystallites and sub-micrometer-sized "sea urchin"-like rutile (200–500 nm) aggregates are formulated in a stable isopropanol suspension without resorting to organic or inorganic binders or charging agents. Interestingly, extremely high quality and robust films are obtained thanks to the high surface reactivity, electrophoretic mobility and unique morphology of the sea urchin-like rutile aggregates. As result of the excellent film adhesion rendered by rutile, contact resistance between the TiO_2 film and the FTO-glass substrate is minimized resulting in higher V_{OC} and fill factor, in addition to their scattering functionality. It is shown that by increasing the dye-coated anatase component, light absorption and photocurrent (J_{sc}) generation increases up to certain degree only due to increasing incidence of charge recombination. Use of an intermediate in size and mixed phase TiO_2 material (P25) helped optimize the composite photoanode built on FTO-glass that upon annealing at 450°C yielded a record conversion efficiency (8.59% vs. 8.32% for double-layer benchmark photoanode) for an EPD-fabricated DSSC without resorting to mechanical compression. Such green-engineered mesoporous electrode structures can be successfully built on metallic and plastic substrates and find application in various energy and environmental fields where nanostructured TiO_2 materials are employed.

6.2. Introduction

Nanotechnology-based photovoltaic energy conversion devices, like dye-sensitized solar cells (DSSCs) [1], are currently in the center of an unprecedented global R&D activity driven by the realization that only the harvesting of solar energy can provide abundant sustainable solutions to our climate change and

human economic development challenges. Commercialization of such nanomaterial-based *PV* devices despite the promise of "low-cost" [1] that is repeated in almost all publications (at least 1000/year on DSSCs alone) remains elusive. As we intensify our research efforts for higher efficiency DSSCs [2-3] there is a pressing need equal attention been given to issues like cost, scalability and green chemistry/manufacturing compliance. It is only in this way that the new generation *PV* nanotechnologies can offer a truly sustainable solution for the world something that the current silicon and thin-film CdTe/CIGS PV options do not offer. At the same time production of robust solar cell products built on different substrates (glass, metal [4], plastic [5]) for versatility and easy installation such as in building integration can dramatically facilitate the proliferation of solar energy utilization. By far innovative high-throughput solution processing making use of benign solvents with minimum energy consumption and chemical waste generation can enable the green engineering of superior DSSC electrode structures. In this context, the present work describes the construction of extremely robust and highly performing light harvesting mesoporous electrodes on different substrates via the design of a novel self-assembled and free of binders or additives electrophoretic deposition system for aqueous-synthesized nanotitania particle blends. Such green-engineered electrode structures can find application in other energy and environmental fields than DSSCs alone where different phase nanostructured TiO_2 materials are used as is the case of water splitting [6], photocatalysis [7-10], or lithium-ion energy storage [11].

Typically, a DSSC comprises a photoanode, a counter electrode and an electrolyte [3]. The photoanode, the focus of the present work, in its standard configuration has a mesoporous film of titanium dioxide (TiO_2) nanoparticles (~20-30 nm in size) built on transparent conducting glass substrate via screen printing and annealing/sintering [4, 12]. The nano-TiO_2 film serves as scaffold for the adsorption of the sensitizing dye molecules as well as electron transport network hence the importance of optimizing the dye-TiO_2 interface [13-15]. In addition for enhancing the DSSC's photoconversion efficiency it is imperative that the

electrode structure incorporates proper light scattering components [16]. As such large (sub-micron sized corresponding to visible light wavelength range) TiO_2 particles are employed. The most common strategy adopted for the incorporation of scattering light functionality to the photoanode is a double-layer film structure made of a thin transparent layer (~12 μm thick of anatase nanoparticles) covered with a separate layer (~5 μm thick) of scattering TiO_2 particles [17]. Although effective, this approach results in adding complexity and cost as the film needs to be annealed/sintered twice after each layer deposition. Alternatively the large scattering particles may conveniently be introduced as part of the transparent anatase paste and deposited as single layer. This approach however is associated with significant photocurrent loss due to lower dye loading on the large scattering particles. In recognition of this limitation it has been proposed to replace the large scattering particles with various nanocrystalline aggregates or hierarchical nanostructures that can equally serve as the dye-anchoring transparent anatase network and as scattering structures [16, 18]. Despite their elegant appeal, questions are raised as to the practicality of several of these dual-function nanostructures because of the complex synthesis and fabrication protocols involved.

Recently we reported on the aqueous solution synthesis of a new nanostructured rutile aggregate (200-500 nm) variety that has "sea urchin"-like external features and very large surface area (>80 $m^2.g^{-1}$) [19]. Blending this material with aqueous synthesized anatase nanocolloids (5–10 nm) [20] in a hybrid paste formulation proved to have excellent potential for the construction of screen-printable single layer dual-function DSSC photoanodes [12]. However, preparation of screen-printing pastes is time consuming and makes heavy use of organic chemicals like ethanol (solvent), terpineol (rheological agent) and ethyl cellulose (binder) [21] that need to be evaporated (ethanol) and decomposed/removed (terpineol and ethyl cellulose) in a subsequent high-temperature sintering (at ~450°C) treatment. The latter is incompatible with electrode preparation on plastic substrates, nor to mention the risk of residual carbon deposit that can act as recombination sites [5]. Moreover the use of a binder

does not allow in the case of multicomponent paste formulation as is the case of blends of anatase nanocrystallites and different scattering entities like "sea-urchin"-shaped rutile used in this work [12], or other crystal shapes like TiO_2 nanotubes [22-25] to achieve satisfactory packing and hetero-phase particle networking. With the view of providing an optimized light harvesting single layer photoanode structure via a fully green engineering approach we have developed an organic binder-free electrophoretic deposition (EPD) process that features aqueous-synthesized anatase nanocrystallites and "sea-urchin"-shaped rutile aggregates. Via proper formulation of the particle blend suspension in isopropanol we show that extremely robust composite (anatase/rutile) TiO_2 films can be produced on different substrates from FTO-glass to metallic titanium foil and ITO-PEN plastic materials without having to resort to post-deposition compression [26]. Detailed structural and photoelectrochemical characterization reveals that the sub-micron sized "sea urchin"-like rutile aggregates act as assembling anchors for the anatase nanocrystallites leading to superior substrate-film adhesion and intra-film light harvesting structure. Upon optimization and annealing at ~450°C of the FTO-glass based dual-function electrode film a record conversion efficiency (8.59%) for an EPD-fabricated DSSC was obtained that surpasses all previously published studies [27-34].

6.3. Experimental

6.3.1. Synthesis of TiO_2 components

Anatase and rutile were synthesized via forced hydrolysis of aqueous $TiCl_4$ solution as described elsewhere [19-20]. In general, a 200 *mL* solution was prepared and subjected to forced hydrolysis in a well-agitated batch reactor employing mechanical stirring (~1000 rpm) at 80°C. For anatase, a 0.2 *M* $TiCl_4$ solution was hydrolyzed over a period of 30 min. Higher $TiCl_4$ concentration or longer retention time favored the formation of rutile. The rutile used in this work was prepared via hydrolysis of a 0.5 *M* $TiCl_4$ solution over 2 hours. The obtained

colloidal suspension was quenched, and kept in a cold water bath (at 3°C). To facilitate recovery of the suspended nano particles, the final solution was neutralized to pH ~3-4 with NH_4OH in order to promote coagulation. This was followed by separation in a centrifuge (6000 rpm) and multiple washings of the collected wet particulates with deionized water.

6.3.2. Suspension preparation and EPD procedure

The freshly separated anatase and rutile particulates were washed up to 7 times to ensure complete removal of residual chloride ions before directly dispersed in isopropanol to prepare the EPD suspension. The total particle concentration was 5 $g.L^{-1}$. Different ratios of anatase, rutile and P25 (AEROXIDE® TiO_2 P25, Evonic) were investigated. First, each freshly prepared and washed component was dispersed separately in isopropanol with an ultrasound horn for 5 minutes followed by 10 minutes of magnetic stirring. Then, the individual component suspensions were mixed together by magnetic stirring for 60 minutes and 10 minutes of ultrasonication prior to transferring into the electrophoretic cell. It is notable that contrary to previous EPD practices [27, 35-36], where binders and charging agents are added, none was used here.

EPD was performed at constant 80 V DC voltage applied between a stainless steel sheet (anode) and a fluorine-doped tin-oxide conducting glass substrate (FTO-Glass, 7 $\Omega.cm^{-2}$, Sigma-Aldrich) or ITO-PEN (plastic substrate, 15 $\Omega.cm^{-2}$, Kintec) or Ti foil (metal substrate, 42 $\mu\Omega.cm$, Sigma-Aldrich). The surface area of the substrate was 5 cm^2. The two EPD electrodes were separated by 2 cm corresponding to an electric field of 40 $V.cm^{-1}$. This electric field is much lower than other recently reported isopropanol/TiO_2 systems (200 $V.cm^{-1}$) [28] ensuring the electrochemical stability of the solvent hence its re-use – an important green manufacturing consideration. A Keithley 2400 Source Meter was used as a power supply unit. EPD was run for different deposition times enabling the production of variable thickness films. In order to minimize the problem of crack formation (caused during post-deposition annealing) [37-38] with increasing film thickness,

each film was built with multi deposition cycles of EPD involving drying at room temperature between cycles.

6.3.3. Solar cell assembly

The freshly deposited films were annealed at 450 °C in air for 30 min followed by $TiCl_4$ post-treatment and annealed again [39]. After cooling to room temperature, the TiO_2 films were sensitized by immersing into a 0.5 *mM* solution of N719 in ethanol at room temperature for 24 *h*. The TiO_2 film was rinsed with ethanol to remove physisorbed dye molecules. In order to assemble DSSC, the Pt-counter electrode was prepared by dripping a drop of 5 *mM* $HPtCl_6$-propanol solution onto the pre-cleaned FTO-glass and then heated at 400 °C for 30 min. A two-electrode sandwich cell separated by 30 μm spacer (Surlyn®-30, Dyesol) was sealed with a cell assembly machine (E002-1233, Dyesol) and filled with a standard iodide/triodide electrolyte (EL-HPE, Dyesol) through a hole pre-drilled on the counter electrode. Finally for comparison purposes, double-layer electrode films were also produced by screen-printing (Electric flat screen printer/Model AT25PA-Dyesol) using the benchmark transparent (18NR-T, Dyesol) and scattering (WER2-O, Dyesol) pastes supplied by Dyesol.

6.3.4. Characterization

The electrophoretic mobility of the colloidal suspension was measured with a Malvern Zetasizer Nano ZS (Malvern Instruments Ltd., UK). The film thickness was measured using the Dektak 3030 surface profiler system (Veeco Instruments Inc., U.S.A.). X-ray diffraction (XRD) analysis was performed using a Bruker D8 diffractometer equipped with a GADDS 2D detector and Cu $K\alpha$ radiation (λ = 0.15406 nm) at a scan rate of 5°/min. The ratio of deposited anatase to rutile was quantified using PANalytical-High score software on the basis of the relative peak intensity of (101) of anatase (2θ = 25.2º) and (110) of rutile (2θ = 27.5º). The morphology of the TiO_2 films was characterized using the cold-FEG-SEM Hitachi

SU-8000. The diffusive reflectance spectra of deposited films as well as the absorption spectra of dye-loaded films were recorded with a *PV* Measurements Inc. Quantum Efficiency system, model QEX10.

For current–voltage (*J-V*) characterization, an ABA solar simulator (PV measurements Inc., Model SASS) was employed to provide uniform and constant light illumination of 100$mW.cm^{-2}$ (AM 1.5 solar emission) via a Xenon lamp. The light intensity was adjusted with a Si reference cell. Cells were properly masked in order to eliminate extra scattered light and edge effects [40-41]. The active area of all cells measured was 0.175 cm^2.

Electrochemical impedance spectra (EIS) analysis was carried out by using a VSP-potentiostat system (BioLogic). EIS was performed under 100 $mW.cm^{-2}$ illumination, applying a 10 *mV* AC signal and scanning in a frequency range between 400 *kHz* and 1 *Hz* at different forward applied bias. The EIS data was analyzed with the Z-view software. The IPCE measurements were performed with a *PV* Measurements Inc. Quantum Efficiency system, model QEX10, using a 150*W* Xe lamp coupled with a slit monochromator. The intensity of incident monochromatic light was calibrated with a Si photodiode.

6.4. Results and Discussion

6.4.1. Aqueous-synthesized anatase nanocrystallites and “sea urchin”-shaped rutile aggregates

The typical benchmark grade anatase TiO_2 materials used in transparent or scattering paste formulations featured in DSSC record-breaking devices [2] are prepared by a combination of sol-gel and hydrothermal processes [42-43] that are chemical and energy-intensive hence relatively costly. By comparison here we make use of easily synthesized but highly performing transparent and scattering TiO_2 via a green aqueous process based on forced hydrolysis of abundant and low cost $TiCl_4$. By adjusting the $TiCl_4$ concentration the process can be used to

produce either transparent anatase nanocrystallites [20] or large sub-micron sized rutile particulates [19].

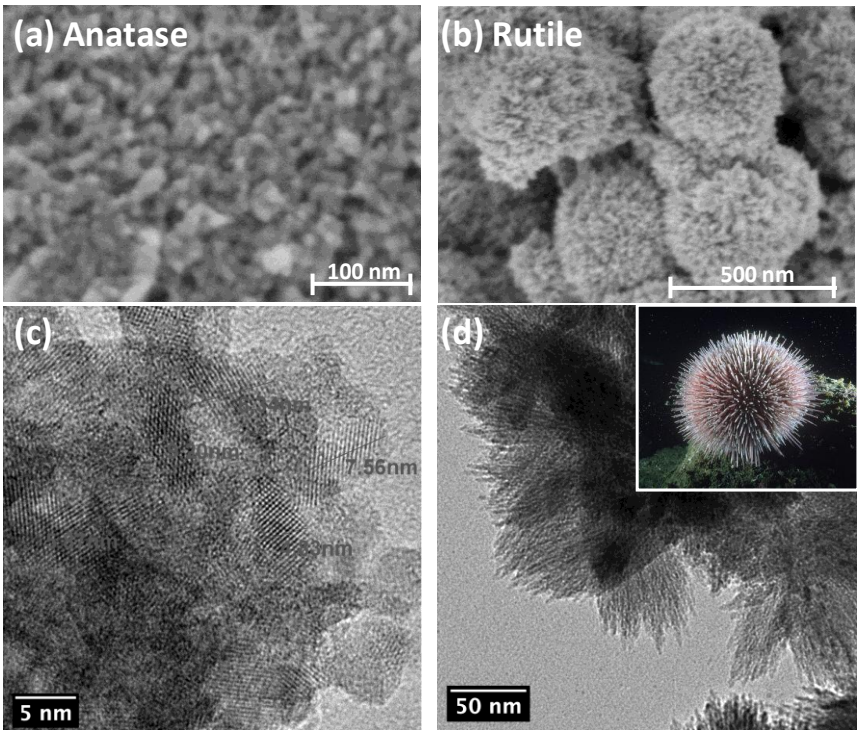

Figure 0-1. SEM and TEM images of aqueous-synthesized TiO_2 materials: (a, c) anatase nanocrystallites, and (b, d) "sea urchin"-like rutile aggregates, Inset in (d) shows a real sea urchin

Figure 0-1 presents the SEM and TEM images of our aqueous-synthesized anatase (5-10 nm) and unique "sea urchin"-like rutile (200-500 nm) particles. The anatase nanocrystallites were found to possess huge surface area (131.4 $m^2.g^{-1}$) desirable for dye loading, the latter further facilitated by the presence of surface hydroxyl groups [14]. Similarly, the large rutile aggregated particles despite their size, they posses high surface area (81.5 $m^2.g^{-1}$) equivalent to that of the benchmark Dyesol anatase material [44] and double of that of P25 product (45.3 $m^2.g^{-1}$). This high surface area of the rutile aggregates reflects their unique internal self-assembled nanofibre structure (Figure 0-1(d)). The same rutile material was found to have relatively large BET average pore volume 0.372 $cm^3.g^{-1}$ in comparison to that of anatase (0.176), and P25 (0.237) further

facilitating the construction of an optimized mesoporous film for superior photovoltaic response.

6.4.2. EPD composite film construction

As mentioned earlier the standard method of photoanode fabrication involves paste preparation and screen-printing of a double-layer (transparent-scattering) film (Figure 0-2(a)). By employing electrophoretic deposition considerable simplification is introduced by removing the entire steps of prior drying and grinding the TiO_2 materials as well as the chemicals during the time consuming paste making process. Thus the aqueous-synthesized anatase and rutile components are directly transferred into the isopropanol solvent immediately after their washing and deposition is done over a few minutes at room temperature. Isopropanol that was used here as the suspension medium is better suited for larger scale application rather than other lower molecular weight (MW) alcohols employed previously [27, 30] due to its higher boiling point (better plant hygiene), its easier recovery-recycling, and electrochemical stability [45-46].

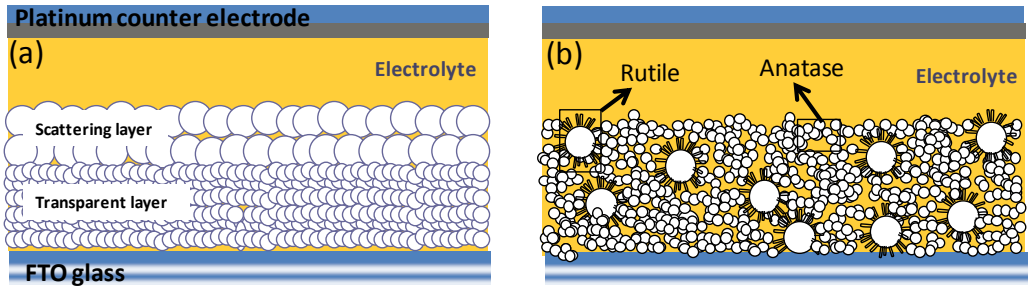

Figure 0-2. Schematic diagram of the (a) conventional double layer and (b) single-layer composite bi-functional photoanode structure.

However, a pre-requisite for successful EPD is the preparation of a stable colloidal suspension. Typically stabilization of EPD suspensions is accomplished via the use of charging agents [35, 47]. While this approach is very effective when one type of single sized particles is used [48] this is not the case necessarily with

multi-sized particles of different type, i.e anatase and rutile in the present system due to potential differences in terms of surface charge properties of the different particle classes [49]. We have discovered that in the case of the present anatase-rutile system a stable suspension can be obtained without the use of additives like binders or charging agents enabling the green engineering of a single-layer bi-functional film structure (Figure 0-2(b)). This became possible by thorough washing of the two aqueous-synthesized TiO_2 materials. A similar behaviour was reported previously for ZrO_2 powders [50]. It was determined that washing helps to remove chloride ions (originating from the $TiCl_4$ – containing synthesis solution [20]) adsorbed on particle surfaces. It took 7 washing cycles to remove completely the interfering Cl^- ions. It is worth noting that EPD of partially washed (e.g. 3 cycles) TiO_2 particulates was not feasible. We postulate that the adsorbed chloride ions neutralize the inherent positive surface charge that develops on the TiO_2 particles as a result of the residual water (0.3-0.5%) [46, 51-52] carried with them from the washing stage.

The positive surface charge of the thoroughly washed anatase and rutile components (while in individual suspension in isopropanol) was confirmed with electrophoretic mobility measurements. The corresponding values were +0.2672 10^{-8} $m^2.V^{-1}.s^{-1}$ for rutile-TiO_2 and +0.1296 10^{-8} $m^2.V^{-1}.s^{-1}$ for anatase-TiO_2. Since electrophoretic mobility is directly proportional to zeta potential [53] we can conclude that the sea urchin-like rutile aggregates possess an unusually high surface reactivity hence their higher positive charge. Preliminary EPD trials with single component suspensions yielded good rutile film but in contrast anatase did not deposit well producing very weak and soft film that peeled off during drying - such contrasting behavior is attributed to their electrophoretic mobility differences. It was after preparing a mixed suspension by blending the anatase nanocrystallites with the sea urchin-like rutile aggregates that extremely adherent films were deposited. The extremely robust nature of the as-deposited composite anatase-rutile films can be appreciated by watching the short video provided as part of the SI material of the paper. It appears in other words that the unique sea-

urchin-like rutile aggregates act as “anchors” for the deposition of the anatase nanocrystallites. Such anchoring of the electrophoretically driven nanoparticles onto the cathodic substrate is likely further facilitated via fragmentation of some of the rutile needle-like thorns and creation of secondary nucleation sites. In this way, dual phase (anatase-rutile) films of exceptional strength, adhesion, and quality are obtained that can be advantageously used as photoanodes.

EPD was performed in three different suspension ratios of anatase (A) to rutile (R) components, namely 80% A-20% R, 50% A-50% R, and 20% A-80% R and the produced films were characterized in terms of composition and structure. The % anatase and rutile composition of the deposited films was quantified by XRD (Figure 0-3(a) and Table 0-1). The co-deposition of rutile with anatase was also indirectly verified by the higher reflectance of the films obtained from suspensions containing higher amount of large size rutile particles (Figure 0-3 (b)). However, the film composition, with the exception of the 20% A-80% R case, was found to differ from that of the suspension. Thus, the 80% A-20% R and 50% A-50% R suspensions yielded 54% A-46% R and 36% A-64% R film composition, respectively. Apparently, owing to its higher electrophoretic mobility ($0.2672\ 10^{-8}\ m^2.V^{-1}.s^{-1}$ vs. $0.1296\ 10^{-8}\ m^2.V^{-1}.s^{-1}$) rutile deposited at faster rate than anatase. This was confirmed by making use of the Hamaker equation (6-1) [48, 53]:

$$\frac{dY}{dt} = k\mu cES \qquad (0\text{-}1)$$

in which the yield is Y (g), the time t (s), the electrophoretic mobility μ ($m^2.V^{-1}.s^{-1}$), the electric field E ($V.m^{-1}$), the concentration of particles in suspension c ($g.L^{-1}$), the electrode surface area S (m^2) and k, a dimensionless factor ($k \leq 1$) that takes into account that not all particles reaching the electrode will actually become part of the film (deposit). In the case of the 50% A-50% R suspension the estimated film composition matches the one measured with XRD (Table 0-1). However, for the other two wider range suspension compositions there were significant deviations between actual and estimated values. This

discrepancy may arise from the inevitable simplifying assumptions inherent in the Hamaker equation. One such assumption is that there is non-interference in the deposition behavior of particles to each other in the mixed suspension. The other assumption is that the *k* value is the same for both types of particles, which cannot be true given the contrasting EPD film quality obtained from the individual suspensions (poor anatase film vs. good rutile film).

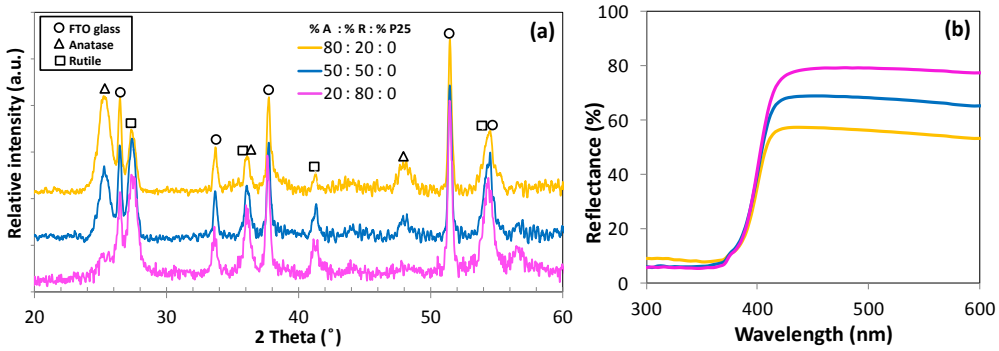

Figure 0-3. XRD patterns (a) and reflectance spectra (b) of three composite (anatase-A/rutile-R) films deposited from suspensions of different % anatase:% rutile ratio

Table 0-1. Percent composition of composite films obtained from different suspension anatase:rutile ratios; XRD measured values compared to Hamaker equation estimates

Suspension Composition	*Film Composition*	
	Anatase (%) Deposited(Estimated)	*Rutile (%) Deposited(Estimated)*
80% A-20% R	54±3 (66)	46±3 (34)
50% A-50% R	36±1 (33)	64±1 (67)
20% A-80% R	21±2 (11)	79±2 (89)

SEM images of film cross sections obtained from the three suspensions are shown in Figure 0-4. The quality, uniformity and more importantly the film adhesion improved significantly, by increasing the amount of sea urchin-like rutile particles. The film with the highest percentage of anatase nanocrystallites (Figure 0-4(a)) was very compact and lacked uniformity as also was observed previously when the same material was deposited via paste screen printing [12, 20].

This lack of film uniformity with the high content anatase suspension is thought to arise from aggregation due to the, lower electrophoretic mobility of the anatase nanoparticles that translates to lower zeta potential. The mesoporous film structure (decreased packing density and increased pore size distribution) is seen to improve, when the amount of deposited rutile is increased (Figure 0-4 (b) and (c)), in correspondence to the higher pore size volume of the sea urchin-like rutile particles. When a DSSC is assembled with this improved film structure electrode, the stronger film adhesion onto the substrate leads to improved electron percolation path to the substrate and better electron collection at the FTO/TiO_2 interface. In addition, the higher pore size distribution facilitates electrolyte diffusion in the mesoporous film structure finally boosting the DSSC efficiency.

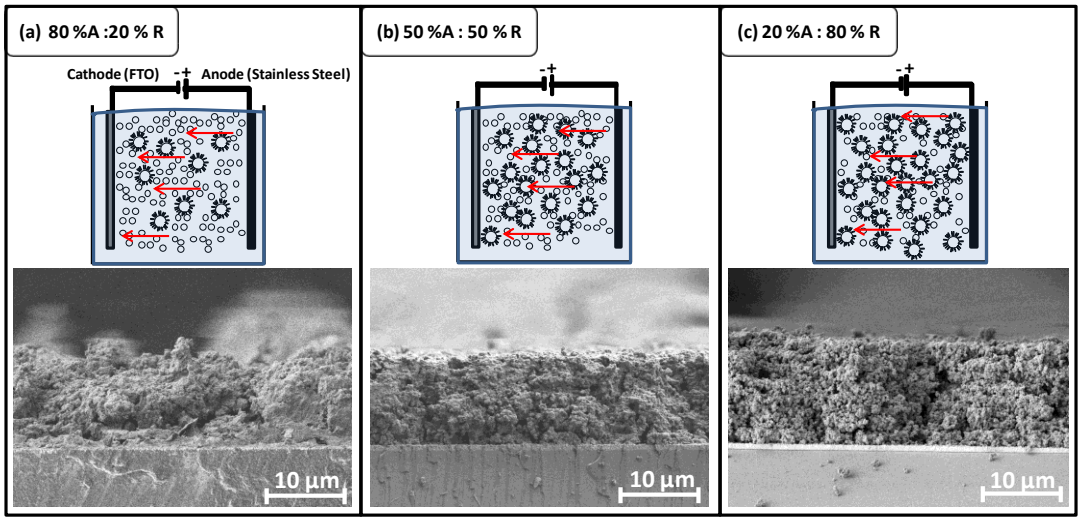

Figure 0-4. SEM cross sections of composite films deposited from variable anatase:rutile composition suspensions

6.4.3. DSSC photoelectrochemical performance

DSSCs based on these three composite films as well as additional ones incorporating P25 as third component (to be discussed in the next section) were assembled and their photovoltaic (*J-V*) and electrochemical characteristics (EIS) were measured and analysed as summarised in Table 0-2 and Figure 0-5.

Focusing first on the three P25-free devices we can make the following observations with reference to the relative effects anatase and rutile components have on various performance indicators. By far among these three cells the 50%A-50%R prepared photoanode gave the best photoconversion efficiency (7.43% PCE) and open circuit voltage (0.67 V V_{OC}). The 80%A-20%R had a slightly lower PCE (7.07%) but higher photocurrent output (14.7 vs.14.5$mA.cm^{-2}$), while the 20%A-80%R photoanode had the worst PCE and J_{sc} but high FF and V_{OC}. This implies that the two components (anatase and rutile) impact differently the light harvesting and *PV* performance of the photoanode hence the need for optimization via creative balancing of the opposite effects. Before this is done individual performance parameters need to be analysed so to maximize their positive outcome. To this end both optical (Figure 0-5 (a) and (c)) and photoelectrochemical (dark current analysis (Figure 0-5 (d)) and EIS (Figure 0-5 (e)) measurements were made.

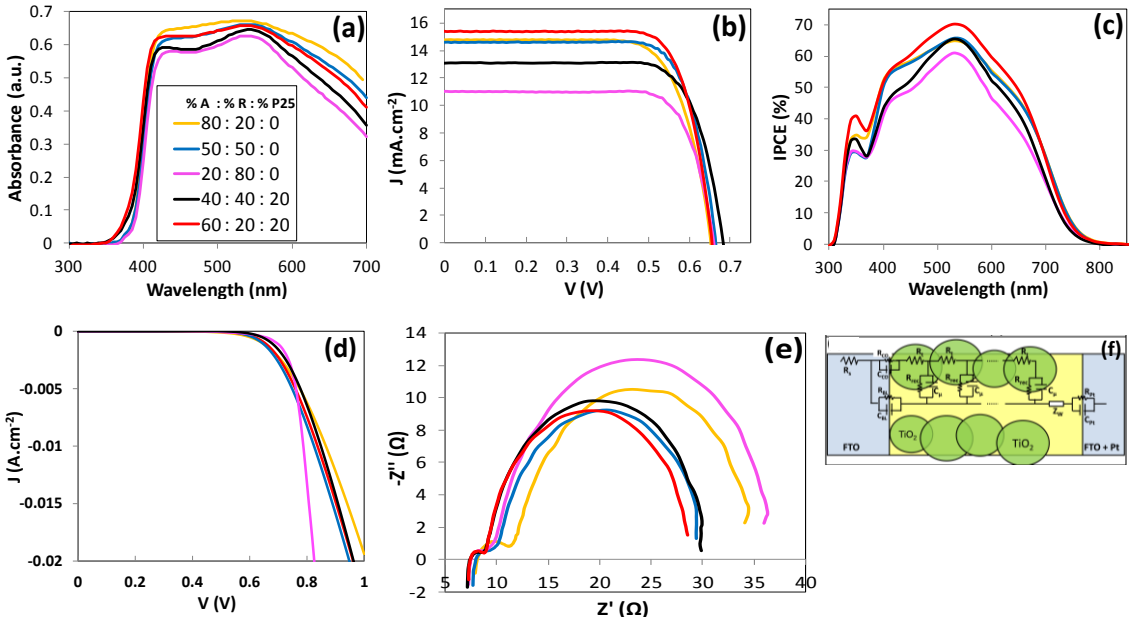

Figure 0-5. (a) Corrected (for the absorption of bare TiO_2) absorption spectra of the dye-covered nano-composite films, (b) *J-V* curves, (c) IPCE spectra, (d) dark current-*V* curves, (e) EIS Nyquist plots, and (f) general transmission line model of DSSCs used to simulate the Nyquist plots [54]

Table 0-2. Photovoltaic and photoelectrochemical parameters of DSSCs made with different composition composite electrodes (*J-V* measurements and fitting results of EIS analysis). The film thickness of all electrodes is ca.11.5μm.

Suspension Composition			PV Performance					EIS Parameters				
Anatase (%)	Rutile (%)	P25 (%)	V_{oc} (V)	J_{sc} (mA cm^{-2})	FF (%)	η_{max} (%)	$\eta_{average}$ (%)	R_s (Ω)	R_{CE} (Ω)	R_t (Ω)	R_{rec} (Ω)	τ_n (ms)
80	20	0	0.65±0.00	14.7±0.1	74±1.0	7.07	6.63±0.44	7.1±0.2	4.3±0.5	1.47±1.00	24.0±0.6	36.6
50	50	0	0.67±0.00	14.5±0.3	76±0.2	7.43	7.22±0.18	7.7±0.5	1.4±0.4	3.79±0.39	20.4±0.4	41.4
20	80	0	0.66±0.00	11.0±0.1	77±0.4	5.62	5.61±0.01	7.1±0.5	1.4±0.1	4.47±0.13	27.8±0.9	62.1
40	40	20	0.68±0.01	13.7±0.7	76±1.7	7.51	7.23±0.39	7.0±0.2	1.4±0.1	2.56±0.07	21.2±0.3	35.0
60	20	20	0.66±0.01	14.9±0.5	75±1.9	7.72	7.47±0.27	7.0±0.1	1.4±0.1	2.15±0.65	18.9±1.3	27.8
75	5	20	0.64±0.00	15.0±0.4	74±1.4	7.29	6.99±0.30	7.5±0.1	4.5±0.1	0.14±0.01	17.9±1.1	22.2
0	0	100	0.72±0.00	10.5±0.3	75±1.9	5.91	5.71±0.17	7.3±0.3	3.4±0.2	0.29±0.1	25.5±0.6	15.9

As shown in Figure 0-5 (a), the photoanode with the highest amount of anatase nanocrystallites had the highest light absorption efficiency reflecting its higher surface area and dye loading capacity as characterized previously [55]. The variation in amount of dye-loading is also evident from differences in photoanode coloration shown in Figure 0-9 (refer to supporting information), which illustrates digital photographs of DSSCs based on the different composite films. Consequently, it resulted in the highest J_{sc} (Table 0-2) in agreement with its higher IPCE as shown in Figure 0-5 (c). However, the higher photocurrent generation with the high anatase content was not translated to higher PCE. This may be explained on the basis of the EIS results (for detailed introduction to EIS refer to the Supporting information section (6.7.2)). Thus, we observed with increasing the anatase content the charge recombination resistance of the photoanode (R_{rec}) to decrease (refer to Table 0-2). We postulate this to stem from the inevitable increase in grain boundaries and surface traps associated with the ultra nanosized (< 10 nm) anatase crystallites as well as the larger interfacial photoanode/electrolyte area [56]. Hence the lower R_{rec} resulted in lower electron life time (τ) and V_{OC} [30].

Returning now to the role of rutile we can identify two effects, in addition to its action in scattering light as evident with the reflectance spectra of Figure 0-3 (b). Firstly with increasing the rutile content as described earlier a mechanically stronger and more adherent film formed on the substrate. This as evident by the

observed correlation between R_{CE} and rutile content (refer to Table 0-2) leads to a decrease in charge transfer resistance from the TiO_2 film to the FTO glass substrate (R_{CE}). As a result the strong contact between the film and the substrate, the fill factor improves, something that was also recently noted by Chen et al.[28]. On the other hand, the charge transport resistance (R_t) of the film (Table 0-2) and the dark current (Figure 0-5 (d)) increased by increasing the amount of rutile particles (refer to Table 0-2) in the photoamode. This undesirable effect may be due to poor heteroparticle connecting after certain rutile threshold is exceeded both in terms of physical and electronic terms.

6.4.4. Optimization of film structure

Having elucidated the role of anatase and rutile in the performance of the photoanode we proceeded to optimization of the film structure by incorporating a fraction (20%) of the commercial P25 TiO_2 product. We thought that the intermediate size (~30 nm) of P25 (in comparison to the home-made anatase and rutile components) would improve inter-particle contacting (i.e. lower the R_t) especially given its mixed phase composition (~80% anatase:~20% rutile) [11] as well improve film porosity for less charge recombination at the photoanode/electrolyte interface. As it can be seen in Figure 0-6, the addition of P25 particles improved significantly the film mesoporous structure, which has as result better electrolyte diffusion. On the other hand, the incorporation of P25 reduced considerably the problem of film cracking during annealing that is known to be a problem with EPD-built films (refer to Figure 0-10 in supporting information) [28, 38].

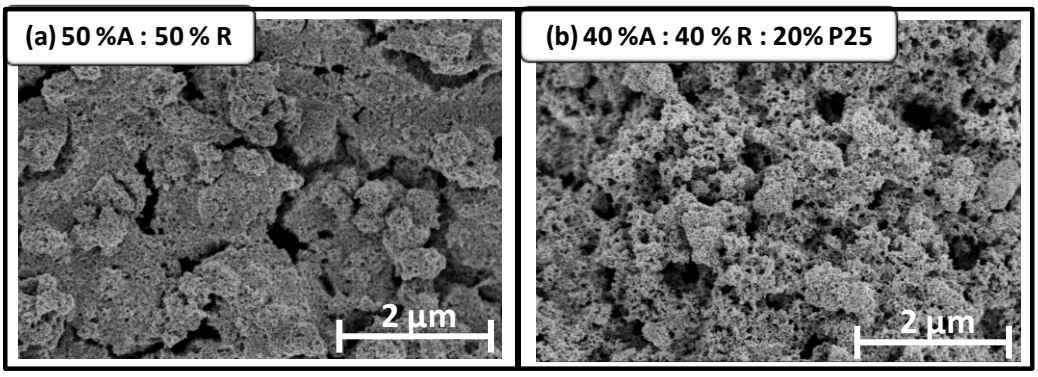

Figure 0-6. Top view SEM images of composite films with (b) and without (a) P25 present

As can be verified with the data presented in Table 0-2, the co-deposition of P25 did result in improved photoanode structure. Thus the film transport resistance (R_t) decreased from 3.79 (50%A-50%R) to 2.56 Ω (40%A-40%R-20%P25), by partial P25 substitution. The PCE of the corresponding cell at the same time slightly improved from 7.43% to 7.51%. Further improvement was attained by reducing the rutile fraction and increasing the photogenerating anatase fraction arriving to the following optimum suspension composition: 60%A-20%R-20%P25. The cumulative film deposit composition from this optimum suspension quantified by XRD measurement was 64% A-36% R (refer to Table 0-4 included with Supporting Information section). (Note that since P25 is a mixed phase TiO_2 product -80% anatase and 20% rutile- the film deposit composition is the cumulative one). As per data of Table 0-2 the PCE and J_{sc} with the latter electrode climbed to: 7.72% and 14.9 $mA.cm^{-2}$. Further reduction of the suspension rutile fraction down to 5% (and increase of anatase to 75%) did not translate however to further improvement revealing the critical role of rutile. As it can be seen in Table 0-2 the drop of the rutile content from 20% down to 5% was associated with substantial increase in TiO_2-substrate resistance (R_{CE}) (from 1.4 to 4.5 Ω), in other words in deterioration of film-substrate adhesion. Hence by engineering the required amount of "sea urchin"-shaped rutile aggregates within the electrode structure we have achieved to maximize photocurrent generation via the dye-coated anatase, increase light trapping via the scattering effect of rutile

and produce low resistance and high strength film-substrate bonding. For comparison purposes a DSSC based on 100% P25 suspension was also fabricated. This device's PCE was only 5.9%, as a result of a lower J_{sc} (10.5 $mA.cm^{-2}$) most likely arising from low dye loading considering the lower surface area of P25 powder (45.3 m^2 g^{-1}) compared to the aqueous-synthesized anatase and rutile.

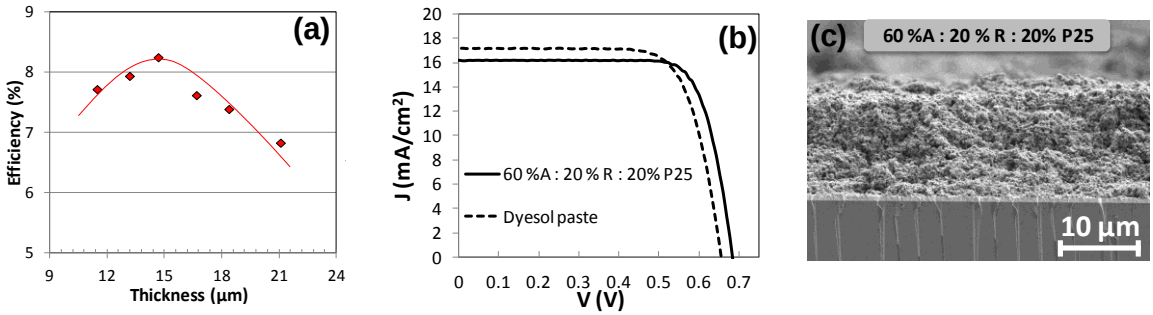

Figure 0-7. Photo-conversion efficiency of DSSCs made from optimized composite films (60%A-20%R-20%P25 suspension) of variable thickness (b) J-V curves of DSSCs based on the best composite electrode and benchmark double-layer electrode made with commercial Dyesol pastes (transparent + scattering) and (c) SEM cross section of optimized composite electrode

Having determined the optimum composite film composition the optimization of the film thickness was pursued next. The film thickness was adjusted by increasing the number of EPD cycles. The results are presented in Figure 0-7 (a). An excellent power conversion efficiency of 8.59 % was obtained for the optimum thickness of 15 µm, which outperforms the cell based on double-layer electrode built via screen-printing using benchmark commercial transparent and scattering pastes (8.32 % PCE) – comparative results shown in Figure 0-7 (b) and Table 0-3. Highly reproducible results were obtained. Five devices fabricated using the same composite film rendered an average PCE of 8.22 % vs. 8.09% for the control devices (Table 0-3). To our knowledge, this is the highest peak PCE reported so far for a DSSC based on a photoanode fabricated by EPD. This is truly remarkable as in the present work no mechanical compression as done in other EPD benchmark studies was applied [27]. It is interesting to further note the higher V_{OC} and fill factor exhibited by the new green-engineered photoanode (see

SEM cross section image in Figure 0-7 (c)) owing to its excellent film-substrate adhesion that supersedes that of the benchmark photoanode as well.

Table 0-3. Comparison of DSSC photovoltaic performance of composite photoanode (60%A-20%R-20%P25) to double-layer benchmark photoanode (Dyesol)

Photoanode	*Thickness (μm)*	*Fabrication method*	*V_{OC} (V)*	*J_{sc} ($mA.cm^{-2}$)*	*FF (%)*	*η_{max} (%)*	*$\eta_{average}$ (%)*
Double Layer Dyesol Pastes	***16***	**Screen Printing**	0.65	17.3	74	8.32	8.09±0.24
Composite Bi-functional	***15***	**EPD**	0.68	16.1	77	8.59	8.22±0.26

6.4.5. Non-glass flexible substrates

Having demonstrated that extremely robust films with excellent film-substrate adhesion strength can be produced on FTO-conducting glass even before any annealing of the film is done (refer to video in the SI section 6.7.1) we decided to evaluate the effectiveness of the new binder-free EPD process on flexible metallic [4, 6, 28] and plastic substrates [5, 31] as well. To this end EPD tests were run using the optimum 60%A-20%R-20%P25 isopropanol suspension with flexible titanium metal sheet and ITO-PEN plastic substrates. No annealing was performed nor compression applied. Once more excellent quality films were produced as can be seen in Figure 0-8, not prone to de-lamination or breakage. Hence further work is warranted for the development of flexible photoanodes featuring the aqueous-synthesized anatase and "sea urchin" rutile aggregates on one hand and their evaluation in different applications beyond DSSCs.

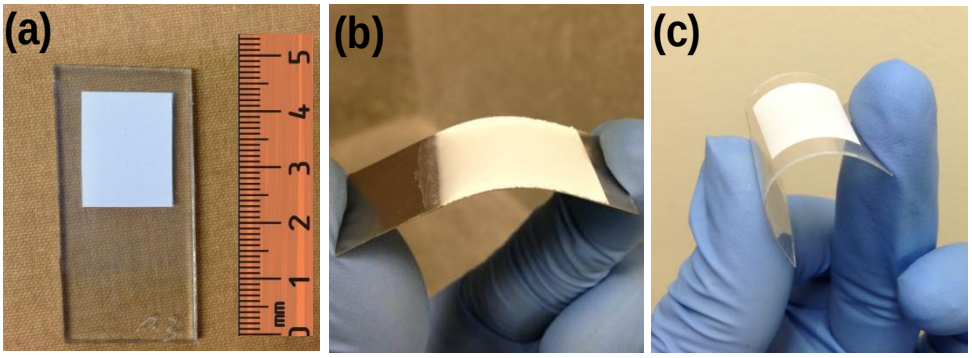

Figure 0-8. Robust composite films deposited on (a) FTO glass, (b) flexible metallic (Titanium) sheet, and (c) plastic (ITO-PEN) material

6.5. Conclusion

The green engineering of highly performing DSSC electrodes was developed via innovative high-throughput solution processing making use of benign solvents (water for synthesis and isopropanol for deposition). We have found that aqueous-synthesized anatase nanocrystallites can be effectively deposited by electrophoretic deposition upon blending with aqueous synthesized "sea urchin"-like rutile aggregates to form superior light harvesting composite film structures upon annealing. Successful deposition of extremely robust films was enabled via the stabilization of the multi-component suspension by prior thorough washing to remove interfering chloride ions and the unique surface reactivity and morphology of the sea urchin-like rutile aggregates. The latter were found to possess twice as much electrophoretic mobility than the anatase nanocrystallites – a property that led in combination with apparent secondary nucleation site formation on the substrate by fragmentation of some of the needle-like thorns to a high strength adherent film. As result of the excellent film adhesion rendered by rutile, contact resistance between the TiO_2 film and the substrate was minimized resulting in higher V_{OC} and fill factor, in addition to their scattering functionality. There is an optimum rutile fraction that can be incorporated above which film transport resistance increases. It was shown that by increasing the dye-coated anatase component light absorption and photocurrent (J_{sc}) generation to increase up to certain degree, thereafter introduction of surface traps leading to deterioration because of higher incidence of charge recombination. Use of an intermediate in size and mixed phase TiO_2 material (P25) helped optimize the composite photoanode structure that upon annealing at 450°C yielded a record conversion efficiency (8.59% vs. 8.32% for double-layer benchmark photoanode) for an EPD-fabricated DSSC without resorting to mechanical compression. Such green-engineered electrode structures finally can be successfully built on metallic and plastic substrates and find application in various energy and environmental fields, where different phase nanostructured TiO_2 materials are employed.

6.6. Acknowledgments

This research is supported via a NSERC strategic project grant and sponsored by CIS Solar, Hydro-Quebec, Versatilis Inc and Targray Technology International. Authors are thankful to Professor Raynald Gauvin and Nicolas Brodusch for using the SEM Hitachi SU-8000. Furthermore, Professor N. Tufenkji is thanked for permission to use the Zetasizer in her laboratory.

6.7. Supporting Information

6.7.1. Video on the adhesive properties of as-deposited composite films

A short video which can be seen at:

http://www.youtube.com/watch?v=AdV8LK9jViE, presents the extremely robust nature of the as-deposited composite anatase-rutile films (the deposited film shown in the video did not go through any kind of post treatment such as annealing at high temperature or compression).

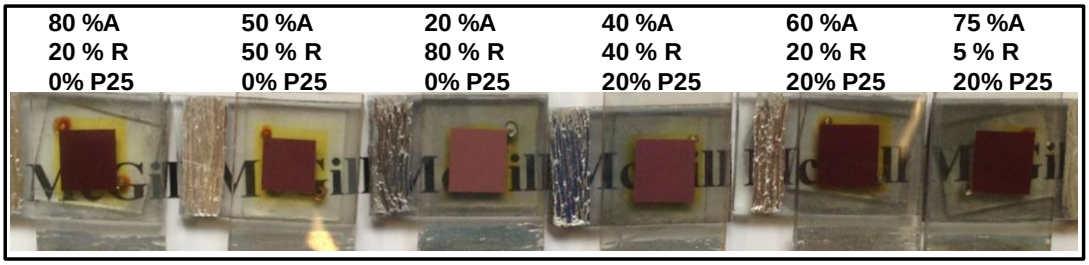

Figure 0-9. Digital photographs of DSSCs based on different composite films with variation in color as a result of different amount of dye-loading on photoanode

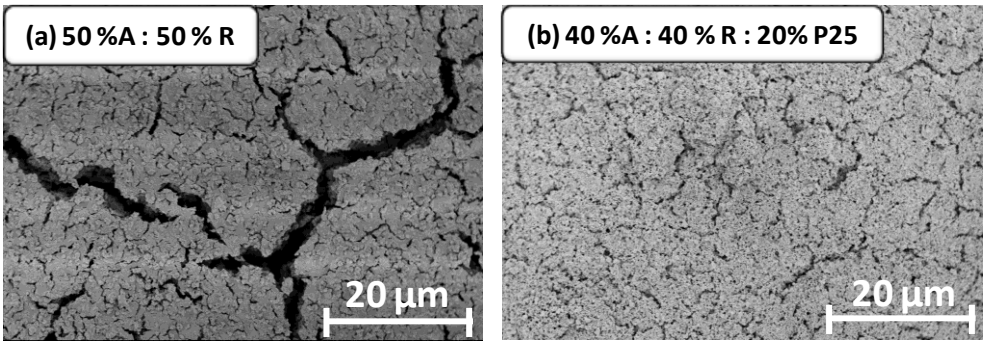

Figure 0-10. Top view SEM images of composite films with (b) and without (a) P25 present showing the positive influence P25 has on crack formation suppression

Table 0-4. Percent composition of composite films obtained from different suspension anatase:rutile:P25 ratios

Suspension Composition	*Film Composition*	
	Deposited Anatase[1] (%)	Deposited Rutile[2] (%)
40% A-40% R-20%P25	59	41
60% A-20% R-20%P25	64	36
75% A-5% R-20%P25	79	21

[1] This amount comprises the fraction of deposited aqueous-synthesized anatase as well as the anatase component typically 80%) of co-deposited P25.
[2] This amount comprises the fraction of deposited aqueous-synthesized rutile as well as the rutile component typically 20%) of co-deposited P25.

6.7.2. Electrochemical impedance spectroscopy (EIS) Analysis

Electrochemical impedance spectroscopy (EIS) is considered as a powerful technique to investigate the electron transport and kinetics of interfacial charge transfer processes in DSSCs [57]. A typical EIS spectrum for a DSSC exhibits three semicircles in the Nyquist plot (see Figure 5 (e)). The left (high frequency) semicircles represents (R_{CE}),which consists of the charge transfer process at the Pt counter electrode/electrolyte (R_{Pt}) and FTO/ TiO_2 interfaces (R_{CO}), since the Pt counters electrode were prepared similarly for all devices, the difference observed in R_{CE} can be corresponded to R_{CO}. This semicircle starts from R_s, which

corresponds to series resistance originating from the glass substrates and contacts; the central arc is related to charge transport resistance in TiO_2 film (R_t), recombination at the TiO_2/dye/electrolyte interfaces (R_{rec}) and the chemical capacitance (C_μ); and the third arc is associated with electrolyte diffusion impedance (Z_w) [54]. The third arc is not discernible here because of overlap with the middle-frequency [58] probably due to the use of high performance commercial electrolyte with a small diffusion resistance. Moreover, the electron lifetime (τ) in the TiO_2 film can be extracted from Equation (0-2):

$$\tau = \frac{1}{2\pi f} \quad (0\text{-}2)$$

where f is the characteristic frequency, corresponding to the peak in the intermediate-frequency regime [59]. Electron lifetime was proposed to quantify the extent of electron recombination with the redox electrolyte [60].

6.8. References

1. Kalyanasundaram K, Gratzel M. Themed issue: nanomaterials for energy conversion and storage. Journal of Materials Chemistry 2012;22(46):24190-94.

2. Burschka J, Pellet N, Moon SJ, Humphry-Baker R, Gao P, Nazeeruddin MK, et al. Sequential deposition as a route to high-performance perovskite-sensitized solar cells. Nature 2013;499(7458):316-19.

3. Zhang S, Yang X, Numata Y, Han L. Highly efficient dye-sensitized solar cells: progress and future challenges. Energy & Environmental Science 2013;6(5):1443-64.

4. Carnie MJ, Charbonneau C, Barnes PRF, Davies ML, Mabbett I, Watson TM, et al. Ultra-fast sintered TiO_2 films in dye-sensitized solar cells: phase

variation, electron transport and recombination. Journal of Materials Chemistry A 2013;1(6):2225-30.

5. Miyasaka T. Toward Printable Sensitized Mesoscopic Solar Cells: Light-Harvesting Management with Thin TiO_2 Films. The Journal of Physical Chemistry Letters 2011;2(3):262-69.

6. Swierk JR, Mallouk TE. Design and development of photoanodes for water-splitting dye-sensitized photoelectrochemical cells. Chemical Society Reviews 2013;42(6):2357-87.

7. Kwon S, Fan M, Cooper AT, Yang H. Photocatalytic applications of micro- and nano- TiO_2 in environmental engineering. Critical Reviews in Environmental Science and Technology 2008;38(3):197-226.

8. Kontos AG, Katsanaki A, Maggos T, Likodimos V, Ghicov A, Kim D, et al. Photocatalytic degradation of gas pollutants on self-assembled titania nanotubes. Chemical Physics Letters 2010;490(1–3):58-62.

9. Kontos AI, Kontos AG, Tsoukleris DS, Vlachos GD, Falaras P. Superhydrophilicity and photocatalytic property of nanocrystalline titania sol-gel films. Thin Solid Films 2007;515(18):7370-75.

10. Kontos AI, Kontos AG, Raptis YS, Falaras P. Nitrogen modified nanostructured titania: Electronic, structural and visible-light photocatalytic properties. Physica Status Solidi - Rapid Research Letters 2008;2(2):83-85.

11. Sussman MJ, Brodusch N, Gauvin R, Demopoulos GP. Binder-free fabrication of nanotitania/carbon lithium-ion intercalation electrodes. Journal of The Electrochemical Society 2013;160(5):A3100-A07.

12. Lee KE, Charbonneau C, Demopoulos GP. Thin single screen-printed bifunctional titania layer photoanodes for high performing DSSCs via a

novel hybrid paste formulation and process. Journal of Materials Research 2013;28(03):480-87.

13. Ronca E, Pastore M, Belpassi L, Tarantelli F, De Angelis F. Influence of the dye molecular structure on the TiO_2 conduction band in dye-sensitized solar cells: disentangling charge transfer and electrostatic effects. Energy & Environmental Science 2013;6(1):183-93.

14. Lee KE, Gomez MA, Elouatik S, Demopoulos GP. Further Understanding of the Adsorption Mechanism of N719 Sensitizer on Anatase TiO_2 Films for DSSC Applications Using Vibrational Spectroscopy and Confocal Raman Imaging. Langmuir 2010;26(12):9575-83.

15. Lee KE, Gomez MA, Regier T, Hu Y, Demopoulos GP. Further Understanding of the Electronic Interactions between N719 Sensitizer and Anatase TiO_2 Films: A Combined X-ray Absorption and X-ray Photoelectron Spectroscopic Study. The Journal of Physical Chemistry C 2011;115(13):5692-707.

16. Zhang Q, Myers D, Lan J, Jenekhe SA, Cao G. Applications of light scattering in dye-sensitized solar cells. Physical Chemistry Chemical Physics 2012;14(43):14982-98.

17. Lee J-K, Jeong B-H, Jang S-i, Kim Y-G, Jang Y-W, Lee S-B, et al. Preparations of TiO_2 pastes and its application to light-scattering layer for dye-sensitized solar cells. Journal of Industrial and Engineering Chemistry 2009;15(5):724-29.

18. Sauvage F, Chen D, Comte P, Huang F, Heiniger L-P, Cheng Y-B, et al. Dye-Sensitized Solar Cells Employing a Single Film of Mesoporous TiO_2 Beads Achieve Power Conversion Efficiencies Over 10%. ACS Nano 2010;4(8):4420-25.

19. Charbonneau C, Gauvin R, Demopoulos GP. Nucleation and growth of self-assembled nanofibre-structured rutile (TiO_2) particles via controlled forced hydrolysis of titanium tetrachloride solution. Journal of Crystal Growth 2009;312(1):86-94.

20. Charbonneau C, Gauvin R, Demopoulos GP. Aqueous solution synthesis of crystalline anatase nanocolloids for the fabrication of DSC photoanodes. Journal of The Electrochemical Society 2011;158(3):H224-H31.

21. Ito S, Chen P, Comte P, Nazeeruddin MK, Liska P, Péchy P, et al. Fabrication of screen-printing pastes from TiO_2 powders for dye-sensitised solar cells. Progress in Photovoltaics: Research and Applications 2007;15(7):603-12.

22. Zheng D, Lv M, Wang S, Guo W, Sun L, Lin C. A combined TiO_2 structure with nanotubes and nanoparticles for improving photoconversion efficiency in dye-sensitized solar cells. Electrochimica Acta 2012;83(0):155-59.

23. Kim AY, Kang M. High efficiency dye-sensitized solar cells based on multilayer stacked TiO_2 nanoparticle/nanotube photoelectrodes. Journal of Photochemistry and Photobiology A: Chemistry 2012;233(0):20-23.

24. Zhong P, Que W, Zhang J, Jia Q, Wang W, Liao Y, et al. Charge transport and recombination in dye-sensitized solar cells based on hybrid films of TiO_2 particles/ TiO_2 nanotubes. Journal of Alloys and Compounds 2011;509(29):7808-13.

25. Khamwannah J, Zhang Y, Young Noh S, Kim H, Frandsen C, Kong SD, et al. Enhancement of dye sensitized solar cell efficiency by composite TiO_2 nanoparticle/8nm TiO_2 nanotube paper-like photoelectrode. Nano Energy 2012;1(3):411-17.

26. Lindstrom H, Holmberg A, Magnusson E, Lindquist S-E, Malmqvist L, Hagfeldt A. A New Method for Manufacturing Nanostructured Electrodes on Plastic Substrates. Nano Letters 2001;1(2):97-100.

27. Grinis L, Dor S, Ofir A, Zaban A. Electrophoretic deposition and compression of titania nanoparticle films for dye-sensitized solar cells. Journal of Photochemistry and Photobiology A: Chemistry 2008;198(1):52-59.

28. Chen H-W, Huang K-C, Hsu C-Y, Lin C-Y, Chen J-G, Lee C-P, et al. Electrophoretic deposition of TiO_2 film on titanium foil for a flexible dye-sensitized solar cell. Electrochimica Acta 2011;56(23):7991-98.

29. Wang S, Zhang J, Chen S, Yang H, Lin Y, Xiao X, et al. Conversion enhancement of flexible dye-sensitized solar cells based on TiO_2 nanotube arrays with TiO_2 nanoparticles by electrophoretic deposition. Electrochimica Acta 2011;56(17):6184-88.

30. Xue Z, Zhang W, Yin X, Cheng Y, Wang L, Liu B. Enhanced conversion efficiency of flexible dye-sensitized solar cells by optimization of the nanoparticle size with an electrophoretic deposition technique. RSC Advances 2012;2(18):7074-80.

31. Chen H-W, Liang C-P, Huang H-S, Chen J-G, Vittal R, Lin C-Y, et al. Electrophoretic deposition of mesoporous TiO_2 nanoparticles consisting of primary anatase nanocrystallites on a plastic substrate for flexible dye-sensitized solar cells. Chemical Communications 2011;47(29):8346-48.

32. Liou Y-J, Hsiao P-T, Chen L-C, Chu Y-Y, Teng H. Structure and Electron-Conducting Ability of TiO_2 Films from Electrophoretic Deposition and Paste-Coating for Dye-Sensitized Solar Cells. The Journal of Physical Chemistry C 2011;115(51):25580-89.

33. Chiu W-H, Lee K-M, Hsieh W-F. High efficiency flexible dye-sensitized solar cells by multiple electrophoretic depositions. Journal of Power Sources 2011;196(7):3683-87.

34. Chang H, Su H-T, Chen W-A, David Huang K, Chien S-H, Chen S-L, et al. Fabrication of multilayer TiO_2 thin films for dye-sensitized solar cells with high conversion efficiency by electrophoresis deposition. Solar Energy 2010;84(1):130-36.

35. Besra L, Liu M. A review on fundamentals and applications of electrophoretic deposition (EPD). Progress in Materials Science 2007;52(1):1-61.

36. Tang F, Uchikoshi T, Ozawa K, Sakka Y. Effect of polyethylenimine on the dispersion and electrophoretic deposition of nano-sized titania aqueous suspensions. Journal of the European Ceramic Society 2006;26(9):1555-60.

37. Parsi Benehkohal N, Demopoulos GP. Green Preparation of TiO_2-ZnO Nanocomposite Photoanodes by Aqueous Electrophoretic Deposition. Journal of The Electrochemical Society 2012;159(5):B602-B10.

38. Parsi Benehkohal N, Demopoulos GP. Electrophoretically self-assembled mixed metal oxide- TiO_2 nano-composite film structures for photoelectrochemical energy conversion: Probing of charge recombination and electron transport resistances. Journal of Power Sources 2013;240(0):667-75.

39. Lee K, Charbonneau C, Shan G, Demopoulos G, Gauvin R. Nanocrystalline TiO_2 thin film electrodes for dye-sensitized solar cell applications. JOM Journal of the Minerals, Metals and Materials Society 2009;61(4):52-57.

40. Yang X, Yanagida M, Han L. Reliable evaluation of dye-sensitized solar cells. Energy & Environmental Science 2013;6(1):54-66.

41. Snaith HJ. The perils of solar cell efficiency measurements. Nature Photonics 2012;6(6):337-40.

42. Grätzel M. Sol-gel processed TiO_2 films for photovoltaic applications. Journal of Sol-Gel Science and Technology 2001;22(1-2):7-13.

43. Barbé CJ, Arendse F, Comte P, Jirousek M, Lenzmann F, Shklover V, et al. Nanocrystalline Titanium Oxide Electrodes for Photovoltaic Applications. Journal of the American Ceramic Society 1997;80(12):3157-71.

44. Charbonneau C, Lee KE, Shan GB, Gomez MA, Gauvin R, Demopoulos GP. Preparation and DSSC Performance of Mesoporous Film Photoanodes Based on Aqueous-Synthesized Anatase Nanocrystallites. Electrochemical and Solid-State Letters 2010;13(8):H257-H60.

45. Moldoveanu GA, Demopoulos GP. Producing high-grade nickel sulfate with solvent displacement crystallization. JOM 2002;54(1):49-53.

46. Parsi Benehkohal N, Gomez MA, Gauvin R, Demopoulos GP. Enabling aqueous electrophoretic growth of adherent nanotitania mesoporous films via intrafilm cathodic deposition of hydrous zinc oxide. Electrochimica Acta 2013;87(0):169-79.

47. Lyklema J, van Leeuwen HP, Minor M. DLVO-theory, a dynamic re-interpretation. Advances in Colloid and Interface Science 1999;83(1–3):33-69.

48. Ma J, Cheng W. Deposition and packing study of sub-micron PZT ceramics using electrophoretic deposition. Materials Letters 2002;56(5):721-27.

49. Wang G, Nicholson PS. Heterocoagulation in Ionically Stabilized Mixed-Oxide Colloidal Dispersions in Ethanol. Journal of the American Ceramic Society 2001;84(6):1250-56.

50. Hatton BD, Sakka Y. Influence of Washing on Zirconia Powder for Electrophoretic Deposition. Journal of the American Ceramic Society 2001;84(3):666-68.

51. Negishi H, Yamaji K, Imura T, Kitamoto D, Ikegami T, Yanagishita H. Electrophoretic deposition mechanism of YSZ/n-propanol suspension. Journal of the Electrochemical Society 2005;152(2):J16-J22.

52. Dzombak DA, Morel F. Surface Complexation Modeling: Hydrous Ferric Oxide: Wiley; 1990.

53. Dor S, Rühle S, Ofir A, Adler M, Grinis L, Zaban A. The influence of suspension composition and deposition mode on the electrophoretic deposition of TiO_2 nanoparticle agglomerates. Colloids and Surfaces A: Physicochemical and Engineering Aspects 2009;342(1-3):70-75.

54. Fabregat-Santiago F, Bisquert J, Palomares E, Otero L, Kuang D, Zakeeruddin SM, et al. Correlation between Photovoltaic Performance and Impedance Spectroscopy of Dye-Sensitized Solar Cells Based on Ionic Liquids. The Journal of Physical Chemistry C 2007;111(17):6550-60.

55. Lee KE, Gomez MA, Charbonneau C, Demopoulos GP. Enhanced surface hydroxylation of nanocrystalline anatase films improves photocurrent output and electron lifetime in dye sensitized solar cell photoanodes. Electrochimica Acta 2012;67(0):208-15.

56. Park K, Zhang Q, Myers D, Cao G. Charge Transport Properties in TiO_2 Network with Different Particle Sizes for Dye Sensitized Solar Cells. ACS Applied Materials & Interfaces 2013;5(3):1044-52.

57. Wang Q, Moser J-E, Gratzel M. Electrochemical Impedance Spectroscopic Analysis of Dye-Sensitized Solar Cells. The Journal of Physical Chemistry B 2005;109(31):14945-53.

58. Wang Z-S, Cui Y, Dan-oh Y, Kasada C, Shinpo A, Hara K. Thiophene-Functionalized Coumarin Dye for Efficient Dye-Sensitized Solar Cells: Electron Lifetime Improved by Coadsorption of Deoxycholic Acid. The Journal of Physical Chemistry C 2007;111(19):7224-30.

59. Fan K, Peng T, Chai B, Chen J, Dai K. Fabrication and photoelectrochemical properties of TiO_2 films on Ti substrate for flexible dye-sensitized solar cells. Electrochimica Acta 2010;55(18):5239-44.

60. Yu H, Zhang S, Zhao H, Will G, Liu P. An efficient and low-cost TiO_2 compact layer for performance improvement of dye-sensitized solar cells. Electrochimica Acta 2009;54(4):1319-24.

Chapter 7. Global conclusions and claims to originality

7.1. Conclusions

Via a series of advanced studies it was shown that electrophoretic deposition can be advantageously deployed as fabrication method for mesoporous nanotitania electrode structures suitable for dye-sensitized solar cell (DSSC) applications using commercially available P25 TiO_2 nanoparticles. This work in particular has achieved to grow mesoporous films on conductive glass using aqueous suspensions opening the road for green fabrication of DSSC photoanodes. This was achieved via the in-situ co-deposition of hydrous metal oxides in particular ZnO that acts as nanoglue. Detailed monitoring of cathodic interfacial potential and XPS analysis of the deposited films shed new light into the intricate mechanism by which the TiO_2-ZnO films are electrophoretically grown. At the same time via application of a suite of photoelectrochemical techniques new insight was advanced to understand interfacial charge recombination phenomena and electron transport properties controlling the photovoltaic performance of these composite DSSC photoanodes. Last but not least in this work EPD was successfully employed in the case of deposition of multi-component TiO_2 nanoparticulates with different size and morphology in order to engineer exceptionally robust TiO_2 films with excellent light harvesting and photoelectrochemical performance. In particular it was found aqueous-synthesized "sea urchin"-like rutile aggregates (200-500nm), when blended with aqueous-synthesized anatase nanocrystallites (5-10 nm), to provide excellent adhesion strength at the film-substrate interface and scattering functionality to the photoanode. As a result record efficiency-breaking DSSC devices were built and robust films on different type of substrates (plastic and metal) were grown. A number of more specific technical conclusions is provided below:

1. A stable aqueous suspension of P25 TiO_2 nanoparticles, which makes deposition of adherent film feasible, was developed by adjusting the surface

tension, conductivity, and zeta potential via the addition of isopropanol and zinc nitrate as co-solvent and charging agent, respectively. In addition, via judicious selection of low DC voltage hydrogen bubble evolution at the cathode was minimized, which along the co-deposition of $Zn(OH)_2$ and metallic nanozinc led to well adherent film (TiO_2-ZnO) growth.

2. The kinetics and mechanism of EPD of TiO_2-ZnO film growth were studied and found zinc in the early EPD stages to deposit as $Zn(OH)_2$ via localized cathodic generation of hydroxyl groups. But in addition, via cathodic potential monitoring and analysis of zinc deposits at different times, it has been for the first time revealed that metallic nanozinc also deposits with the progress of film growth. Both $Zn(OH)_2$ and metallic nanozinc convert to crystalline ZnO upon annealing.

3. DSSC devices based on TiO_2-ZnO composite films resulted in superior photoelectrochemical performances compared to that of bare TiO_2 film. Film growth via multi-EPD cycles yielded electrodes with less cracking during annealing and in combination with post-annealing $TiCl_4$ treatment significantly elevated efficiency (6.44%). By employing various photoelectrochemical measurements it was shown ZnO to behave as a potential blocking layer due to its more negative conduction band compared to TiO_2 thus suppressing the dark current from substrate to electrolyte and increasing the charge recombination resistance having as result to prolong the lifetime of the photoelectrons.

4. After expansion of our work by EPD fabrication of three composite photoanodes, namely, TiO_2-ZnO, TiO_2-Al_2O_3 and TiO_2-MgO, TiO_2-ZnO exhibited the highest film uniformity and quality, most likely reflecting its highest suspension stability. It also resulted in a lowest charge transport resistance and finally highest effective electron diffusion length and PV

performance (η =5.85% and J_{sc}=11.3 $mA.cm^{-2}$). This was explained by the closer CB band of ZnO to TiO_2.

5. The secondary oxides (ZnO, Al_2O_3 and MgO) were found to co-deposit uniformly within the TiO_2 film (forming island-like nanodeposits) at approximately 1-3wt% content and differ from the continuous "core–shell" film structure investigated by others. It has been confirmed that proper selection of the right co-deposited metal oxide that can match the electronic properties of TiO_2 and deliver high interfacial charge recombination resistance while maintaining low the overall electron transport resistance, is critical in electrophoretically forming electrode structures.

6. EPD of multi sized TiO_2 particulates (aqueous-synthesized anatase (5–10 nm) nanocrystalites and sub-micrometer-sized "sea urchin"-like rutile (200–500 nm) aggregates) in isopropanol without resorting to organic or inorganic binders or charging agents was successfully advanced. This was accomplished via the stabilization of the multi-component suspension by prior thorough powder washing to remove interfering chloride ions.

7. Extremely adhesive and robust films were deposited from this suspension of mixed TiO_2 particles thanks to the unique surface reactivity, high mobility, and morphology of the "sea urchin"-like rutile aggregates in combination with apparent secondary nucleation on the substrate by fragmentation of some of the needle-like thorns.

8. An optimum ratio of anatase/rutile particle mixture was determined for the suspension, which upon incorporation of a fraction of P25 intermediate size particles to improve mesoporosity, enabled the fabrication of highly performing bi-functional electrodes. DSSC devices built with the newly configured bi-functional electrodes rendered an excellent power conversion efficiency (*PCE*) of 8.59%, which sets a new record for EPD built DSSCs

while outperforming the cell prepared by double-layer electrode from commercial benchmark pastes via screen printing (8.32%).

9. Finally, such green-engineered mesoporous electrode structures can be successfully built on flexible metallic and plastic substrates without resorting to any organic or inorganic binders followed by high temperature post treatment and/or compression. Therefore, these properties can extend the application of this bi-functional electrode from PV industry to various energy and environmental fields.

7.2. Claims to originality

Several parts of this thesis can be considered as contributions to original knowledge, as can be testified from the quality of journals where these materials were published. Here are the most important ones:

1. Developed an environmentally friendly aqueous EPD system featuring electrolytic co-deposition of ZnO as nanoglue for growth of highly adherent TiO_2 films without using any organic and toxic solvent and/or binder.

2. Elucidated the EPD mechanism of TiO_2-ZnO composite film formation; zinc co-deposition was shown to occur in the early EPD stages via the formation of $Zn(OH)_2$ involving localized cathodic generation of hydroxyl groups by reduction of nitrate to nitrite ions. However, via cathodic potential monitoring and XPS analysis of zinc deposits at different deposition times, it has been for the first time revealed that metallic nanozinc deposits as well with the progress of film growth. The latter, owing to the open-air aqueous environment appears to oxidize partly in situ and be distributed uniformly (~2% Zn) within the entire film. As such this hydrous zinc oxide nanodeposit acts as nanoglue, yielding after annealing very robust and well adhered TiO_2–ZnO composite films.

3. Provided comprehensive photoelectrochemical analysis of nanoscale mixed metal oxide - TiO_2 films produced by EPD and correlated their DSSC performance to the electronic properties of the metal oxides (ZnO, MgO, Al_2O_3) that influence interfacial charge recombination resistance and electron transport.

4. Succeeded to prepare stable suspension of multi-sized and different morphology and phase TiO_2 particulates without using any organic binder/charging agents enabling film deposition on various substrates.

5. Engineered highly robust bi-functional electrodes with record-breaking photovoltaic performance for EPD-built DSSC devices: 8.59% vs. 8.32% for double-layer benchmark photoanode, without mechanical compression applied.

7.3. Suggestions for future work

Future works can be focused on the employment of pulse and AC voltage EPD [1, 2] to further improve the morphology and photoelectrochemical properties of the aqueous-deposited composite films. In addition, since an optimized aqueous-based procedure for deposition of robust composite films has been developed (described in Chapter 3,4 and 5), we can go further and employ gold and/or silver salts as charging agents in the suspension in order to deposit Au/Ag-TiO_2 composites and benefit from their plasmonic effects [3-5]. Along the same lines the EPD technique can be applied to the development of quantum dot sensitized solar cells in continuation of the work accomplished and jointly published by the author of this thesis [6], which was not included here. We showed that EPD of various colloidal quantum dots such as PbS and PbSeS allows a rapid, uniform, and effective sensitization of TiO_2 film with QDs, but further work is needed to improve the conversion efficiency. Finally, assembling DSSCs on flexible

substrates by employing our adhesive bi-functional (anatase-rutile) films (Chapter 6) should be investigated in terms of lower temperature post treatment protocols.

7.4. References

1. Besra L, Uchikoshi T, Suzuki TS, Sakka Y. Bubble-Free Aqueous Electrophoretic Deposition (EPD) by Pulse-Potential Application. Journal of the American Ceramic Society 2008;91(10):3154-59.

2. Besra L, Uchikoshi T, Suzuki TS, Sakka Y. Application of constant current pulse to suppress bubble incorporation and control deposit morphology during aqueous electrophoretic deposition (EPD). Journal of the European Ceramic Society 2009;29(10):1837-45.

3. Brown MD, Suteewong T, Kumar RSS, et al. Plasmonic Dye-Sensitized Solar Cells Using Core−Shell Metal−Insulator Nanoparticles. Nano Letters 2010;11(2):438-45.

4. Ding B, Yang M, Lee BJ, Lee J-K. Tunable surface plasmons of dielectric core-metal shell particles for dye sensitized solar cells. RSC Advances 2013;3(25):9690-97.

5. Ding IK, Zhu J, Cai W, et al. Plasmonic Back Reflectors: Plasmonic Dye-Sensitized Solar Cells. Advanced Energy Materials 2011;1(1):51-51.

6. Parsi Benehkohal N, González-Pedro V, Boix PP, et al. Colloidal PbS and PbSeS Quantum Dot Sensitized Solar Cells Prepared by Electrophoretic Deposition. The Journal of Physical Chemistry C 2012;116(31):16391-97.